# Development, Optimization and Testing of an Innovative Wedge Anchorage for CFRP Plates

by

Mustafa A. Alhusain

A thesis
presented to the University of Waterloo
in the fulfilment of the
thesis requirement for the degree of
Master of Applied Science
in
Mechanical Engineering

Waterloo, Ontario, Canada, 2018

# Author's Declaration

I hereby declare that I am the sole author of this thesis. This is a true copy of the thesis, including any required final revisions, as accepted by my examiners.

I understand that my thesis may be made electronically available to the public.

# Abstract

Replacing degraded concrete structures can be quite expensive and time consuming; thus, strengthening these structures with fiber reinforced polymer (FRP) elements, such as carbon FRP (CFRP) plates, is more practical. Prestressing FRP elements is one of the most economical used solution due to its effect on utilizing the high strength of the FRP materials while improving the performance of structural elements. In order to prestress the FRP component, gripping using anchorages must be provided at both ends. However, anchoring FRP plate is challenging due to its vulnerability to lateral loading; therefore, specially designed anchorage systems are required to grip FRP plates effectively to avoid any premature failure.

The presented work investigates the development and optimization of an innovative anchorage that is reliable, reusable, compact and light in weight for gripping CFRP plates. To fulfil these requirements, a wedge anchorage system is chosen as the most suitable for gripping CFRP plates Material selection process is conducted to select the optimal materials for the sleeves, the wedges and the barrel of the anchorage.

An FEM model of the wedge anchorage is developed using ABAQUS finite element package. An optimization process is performed to find the optimal dimensions of the anchorage through which the anchoring strength and the reusability of the anchorage are improved. The effect of the presetting distance on the performance of the optimized anchorage is investigated. Several failure theories are used to investigate the likelihood of CFRP premature failure. Two new analytical models are developed to verify the accuracy of the FEM model. The results of the analytical models are compared well to the FEM results.

The optimized wedge anchorage is then manufactured and experimentally tested. Eight tensile tests are performed to evaluate the performance of the optimized anchorage by gripping the sides of the CFRP plates using the optimized anchorage and a larger dead-end anchorage. Five tests are performed by presetting the optimized anchorage using presetting rig, two of which use hard copper sleeves. The other three tests are conducted by hammering the optimized anchorage. The dead-end is presetted in every test to avoid CFRP slipping. The optimized anchorage system is capable to carry the guaranteed ultimate tensile strength of the CFRP plate when soft sleeves are used. The effect of presetting distance on the CFRP slipping is investigated. Damage analysis is performed after conducting eight tensile tests to examine the reusability of the optimized wedge anchorage.

# Acknowledgements

I would like to express my sincere appreciation and gratitude to my mother and my father for their continuous support, guidance and encouragement throughout my life. I wouldn't have accomplished a thing if it wasn't for them. I owe them my endless gratitude that I would never be able to pay back.

I would also like to express my gratitude to my supervisor, Professor Adil Al-Mayah from Civil Engineering at the University of Waterloo, for his support and guidance during the research program. His humbleness, kindness and positive attitude allowed me to work with him more as a friend than a supervisor. I have learned valuable lessons from my experience with him that I will always apply throughout my academic life.

I would also like to thank the technicians Douglas Hirst, Richard Morrison, Peter Volcic, Jorge Cruz and Phill Laycock from the Civil Engineering Laboratories and the Engineering Machine Shop. I would also like to thank my officemate and my friend Wanis Nafo for his continuous support.

Special thanks to my sponsor, King Faisal University, and to the College of Engineering at King Faisal University for giving me the chance to pursue graduate studies.

*To MY Parents*

# Table of Contents

# List of Figures

# List of Tables

# 1

# Introduction

## 1.1. General Background

A significant number of concrete structures worldwide are currently degraded and in need of repair and strengthening. This is mainly attributed to the degradation of concrete structures due to reinforcement corrosion, creep and fatigue. In addition, most concrete structures are increasingly subjected to higher loads than their designed capacity. Replacement of concrete structures is considerably expensive and time consuming; thus, repair and strengthening these structures with fiber reinforced polymer (FRP) elements, such as carbon FRP (CFRP) plates, is more practical.

Prestressing FRP elements is one of the most economical used solution due to its effect on utilizing the high strength of the FRP materials while improving the performance of structural elements. In order to prestress the FRP component, gripping using anchorages must be provided at both ends. However, anchoring FRP plates is challenging due to its vulnerability to lateral loading; therefore, specially designed anchorage systems are required to grip FRP plates effectively to avoid any premature failure. Hence, several anchorage systems including wedge anchorages, clamp anchorages, and resin potted anchorages are developed to anchor FRP elements effectively.

Although a number of anchorages have been designed by researchers, most of these anchorages are far from being optimal as there is still a huge area of improvement in terms of

- cutting down its cost,
- reducing its weight, and
- improving its gripping performance and reusability.

In order to design the optimal anchorage for CFRP plates, a comprehensive investigation of the factors that can affect the performance and the reusability of the anchorage is conducted. A complete optimization process is then performed to identify the ideal materials and dimensions of the anchorage. The designed anchorage is experimentally tested to examine its performance.

## 1.2. Thesis Structure

The presented work investigates the development and optimization of an innovative anchorage system for CFRP plates in terms of increasing the gripping capacity, enhancing the reusability, and minimizing the cost. Wedge anchorage system is selected, optimized analytically and numerically, manufactured and experimentally tested. The thesis consists of seven chapters. Chapter 1 introduces the general background of the problem statement along with the thesis structure.

The literature review presented in Chapter 2 provides a comparison between fiber reinforced polymer (FRP) materials and steel as well as an assessment of wedge anchorage system, clamp anchorage system and resin potted anchorage system. The different failure modes of an FRP anchorage are briefly described.

A material selection process is presented in Chapter 3. 440C stainless steel is selected as the optimal material for manufacturing the wedges and the barrel. Annealed copper sleeves are used to enhance the gripping strength of the anchorage. The mechanical properties of the CFRP plate, the annealed copper sleeves, and the 440C stainless steel barrel and wedges are presented.

An FEM model is developed in Chapter 4 via ABAQUS software, and a convergence analysis is conducted. An optimization process is performed to design a wedge anchorage that can effectively grip CFRP plates without experiencing plastic deformation. Failure analysis is conducted using various FRP failure theories to confirm the unlikelihood of CFRP premature failure. The effect of the presetting distance on the performance of the anchorage is investigated.

Two new analytical models are created in Chapter 5 to validate the accuracy of the FEM model. The two models are based on different assumptions. Model 1 is mathematically more complex than model 2; however, both models are proven to be exceptionally accurate.

The optimized wedge anchorage is manufactured and experimentally tested as presented in Chapter 6. The test elements and the testing procedure are briefly described. The results of the experimental tests illustrate the performance and the reusability of the optimized anchorage. The reusability of the optimized anchorage is studied by examining the plastic deformation induced after conducting eight tests. The self-seating feature of the optimized anchorage is tested by effectively gripping the CFRP plate by hammering the wedges only. The experimental results are utilized to validate the FEM results.

Chapter 7 provides the conclusion and the recommendations for future work.

# 2

# Literature Review

## 2.1. Introduction

This chapter introduces FRP materials along with their application in concrete structures and mechanical properties. Mechanical gripping and resin bonding anchoring mechanisms are discussed. A comparison between wedge anchorages, clamp anchorages, and resin potted anchorages as well as the common anchorage failure modes are presented. The chapter is concluded by selecting the most suitable anchorage system and identifying the critical mechanical properties that can affect its performance.

## 2.2. FRP Plate Materials

Fiber reinforced polymer (FRP) is a composite material made of a polymer matrix, such as a thermosetting resin, or resin that is reinforced with fibers as shown in Figure 2.1, which specifically depicts a continuous unidirectional FRP element. The polymer matrix is often made of vinylester or epoxy that is reinforced with fiber filaments such as glass fibers, aramid fibers or carbon fibers [1], [2]. The manufacturing process of an FRP element can be briefly described as a pultrusion of fiber filaments followed by fiber impregnation with polymer resin [1]–[3]. The typical mechanical properties of some fiber filaments and resins are shown in Table 2.1 and Table 2.2 respectively. Unidirectional FRP elements are orthotropic due to the fact that the reinforcing fiber filaments have much higher strength and stiffness along the axial direction than along the transverse directions [1], [2], [4]. While fiber filaments reinforce and enhance the strength of the reinforced resins, polymer resins not only improve the transformability of the applied loads to the reinforcing fibers but also protect the fibers from corrosion and detrimental environments [2], [4], [5]

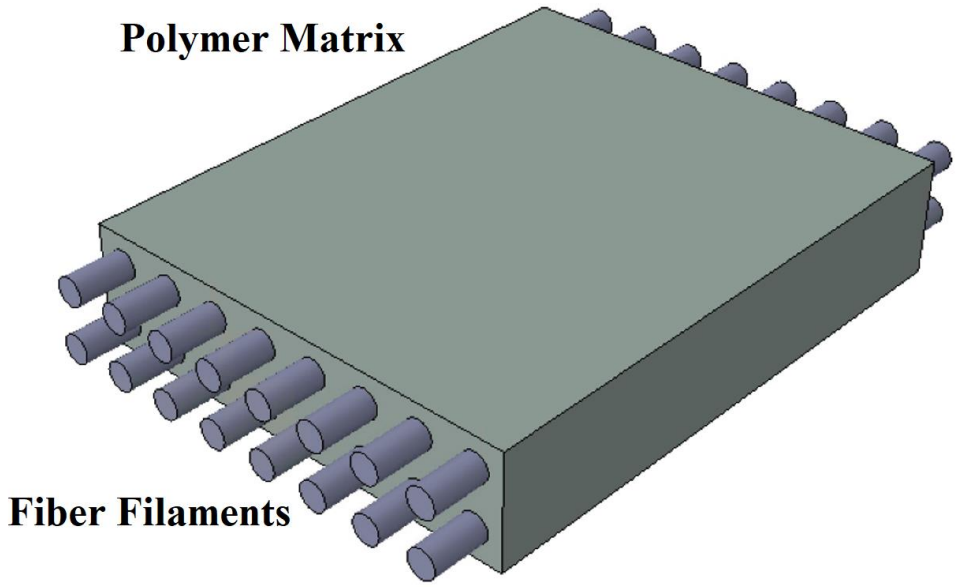


*Figure 2.1: Illustration of Unidirectional FRP Element*

*Table 2.1: Typical Mechanical Properties of Carbon, Aramid and Glass Fibers*

| Property | Carbon Fibers | | | Aramid Fibers | | | Glass Fibers | |
|---|---|---|---|---|---|---|---|---|
| | High Modulus | Intermediate Modulus | Low Modulus | Kevlar | Technora | Twaron | E-Glass | S-Glass |
| **Tensile Strength (GPa)** | 2.41[1] | 2.9[1] | 5.65[1] | 3.4[1]-3.6[1] | 3.5[1] | 2.3[2]-3[1] | 1.8[3]–2.7[3] | 3.4[3]–4.8[3] |
| **Tensile Modulus (GPa)** | 758[1] | 390[1] | 290[1] | 82[1]-179[1] | 74[1] | 70[1]-145[2] | 65[3]–73[3] | 85[3]–90[3] |
| **Ultimate Strain (%)** | 0.2[3]-0.32[1] | 0.5[3]-0.7[1] | 1.2[3]-1.8[1] | 1.9[1]-2.8[1] | 4.6[1] | 2[2]-2.5[2] | 4.5[3] | 5.4[3] |
| **Density (g/cm$^3$)** | 2.15[1] | 1.8[1] | 1.8[1] | 1.45[1] | 1.39[1] | 1.45[1] | 2.58[4] | 2.5[5] |

[1] Academic paper titled "Aramid and carbon fibre-reinforced plastic prestressed ground anchors and their field applications" [2]

[2] Academic paper titled "Glass Concrete Thin Sheets Prestressed with Aramid Fiber Mesh" [6]

[3] Canadian Standards Association [7]

[4] Academic paper titled "Model of concrete confined by fiber composites" [8]

[5] Academic paper titled "Chemical treatments of natural fiber for use in natural fiber-reinforced composites: a review" [9]

*Table 2.2: Typical Mechanical Properties of Epoxy and Vinyl Ester Resins [2]*

| Property | Epoxy | Vinyl ester |
|---|---|---|
| **Tensile Strength (MPa)** | 55-130 | 73–81 |
| **Tensile Modulus (GPa)** | 2.75–4.10 | 3.0–3.5 |
| **Ultimate Strain (%)** | 1-9 | 3.5–5.5 |
| **Poisson's Ratio** | 0.20–0.33 | 0.37 |
| **Density (g/cm$^3$)** | 1.2–1.3 | 1.12–1.32 |

FRP materials are utilized to enhance the flexural strength of concrete as it is susceptible to flexural failure as illustrated in Figure 2.2. The flexural strength of reinforced concrete can be improved further by prestressing processes as they induced compressive stress within the concrete. The most common FRP elements used to reinforce concrete structures are carbon fiber reinforced polymer (CFRP), aramid fiber reinforced polymer (AFRP) and glass fiber reinforced polymer (GFRP) [2]. FRP elements have been studied for decades to replace prestressing steel since steel is heavy, difficult to handle, and vulnerable to corrosion [10]. The typical mechanical properties of CFRP, AFRP, GFRP and prestressing steel are shown in Table 2.3. FRP elements, such as CFRP, are superior compared to steel in terms of being lightweight and having relatively high axial strength, relatively low axial thermal expansion, excellent corrosion resistance and outstanding fatigue properties [4], [11], [12]. However, FRP elements have some drawbacks such as having a high cost, a low modulus of elasticity, an inadequate fracture strain, and a weak resistance to ultraviolet radiation [12], [13]. CFRP, as shown in Table 2.3, has exceptional mechanical properties compared to other prestressing materials making it preferable for prestressing concrete structures; however, it is relatively more expensive. Therefore, it is used in small quantities to reinforce concrete structures [4].

FRP materials used in structural applications are available in different forms such as circular tendons, sheets, and plates. Although, all forms have been used in repair and strengthening, attaching FRP plates to concrete structures is easier and more preferred in the field. FRP plates have relatively high axial tensile strength yet low transverse strength; thus, they are susceptible to premature failure caused by transverse loadings [14], [15]. As a result, while prestressing processes are crucial for enhancing the flexural strength of the concrete and preventing separation failure mode shown in Figure 2.2, they are difficult to perform as proper anchoring of FRP plates is challenging [13], [16]. Thus, anchorage systems designed especially for FRP plates are utilized to allow the implementation of prestressing processes.

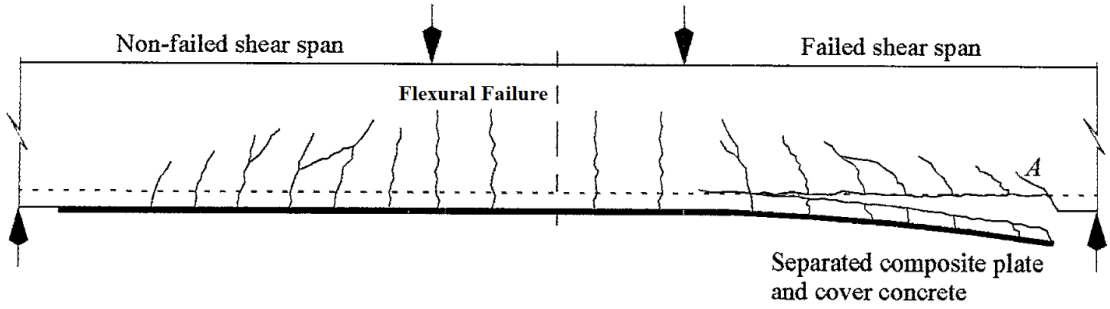


*Figure 2.2: Flexural and Separation Failure Modes of Concrete Structure [17]*

*Table 2.3: Typical Mechanical Properties of Commercially Available FRP Plates [7]*

| Property | CFRP | AFRP | GFRP | Prestressing Steel |
|---|---|---|---|---|
| **Tensile Strength (MPa)** | 1400[1]–2000[1] | 1050[1]–1700[1] | 690[1]–1400[1] | 1379[1]–1862[1] |
| **Tensile Modulus (GPa)** | 117[1]–145[1] | 100[1]–125[1] | 35[1]–48[1] | 186[1]–200[1] |
| **Yield Strength (MPa)** | ----- | ----- | ----- | 1034[1]–1396[1] |
| **Yield Strain (%)** | ----- | ----- | ----- | 1.4[1]–2.5[1] |
| **Ultimate Strain (%)** | 1[1]–1.5[1] | 2[1]–3[1] | 2[1]–3[1] | 4[1] |
| **Coefficient of Thermal Expansion ($\frac{10^{-6}m}{m^oC}$)** | 0.2[2] | −5.7[2] | 7[2] | 11.12[3] |
| **Density (g/cm$^3$)** | 1.5[1]–1.6[1] | 1.25[1]–1.4[1] | 1.25[1]–2.4[1] | 7.9[1] |

[1] Canadian Standards Association [7]
[2] Academic paper titled "FRP reinforcement for concrete structures" [12]
[3] Academic paper titled "Measurement of the thermal expansion coefficient of AISI 420 stainless steel between 20 and 293 K" [18]

## 2.3. FRP Anchorage Systems

FRP anchorage systems are utilized to perform prestressing processes which can increase the efficiency of concrete strengthening by maintaining tensile stress within the FRP plates, thus, enhancing the load carrying capacity of the concrete structure in addition to preventing or delaying debonding induced by interfacial cracking [19]. Several anchorages are developed to improve the anchoring effectiveness of FRP elements [13], [15], [20]–[22]; however, there is still an area of improvement through minimizing the weight and the total cost of the anchorage while maintaining its anchoring effectiveness. The followings are the main requirements of successful anchoring of FRP elements [13], [23]:

- An FRP element must be able to sustain at least 95% of its axial tensile strength after being anchored.
- During the entire service life of an FRP element, the anchorage system should not experience considerable creep or fatigue damage that might lead to its failure.
- The anchorage system must maintain high performance throughout its service life; therefore, corrosion and environmental erosion should not occur within the system.

## 2.4. FRP Anchoring Mechanisms

Two fundamental anchoring mechanisms of FRP plates are mechanical or friction gripping and resin bonding.

### 2.4.1. Friction Gripping

Utilizing friction between the surfaces of the FRP plate and the anchorage system is the essential concept of mechanical anchoring. The friction gripping force is greatly influenced by the area of contact, the contact pressure, the hardness of the associated elements and surface ploughing [24]. Since the area of contact and the contact pressure are self-explanatory, the hardness and the surface ploughing are briefly described.

#### 2.4.1.1. Hardness

Hardness is defined as the resistance of an element to penetration [25]. Hardness is expressed as the ratio of the applied load over the projected area of indentation [26]. Rockwell Hardness Test (HR), Vickers Hardness Test (VHT), Brinell Hardness Test (HBW), or Knoop Hardness Test (HK) are different tests performed to measure the hardness of a material by applying penetrative load via a certain indenter over a small area [25]–[27]. The elements of an anchorage must have sufficiently high hardness to minimize local plastic deformation as that would maintain the performance and enhance the reusability of the anchor.

#### 2.4.1.2. Surface Ploughing

Surface ploughing is defined as the continuous penetration of a surface of a hard material into a surface of a softer material as one element slides on the other due to the existence of asperities as shown in Figure 2.3. Asperities can cause local penetration, ploughing and tearing of the softer element causing local plastic deformation [24].

In general, surface ploughing and friction within a mechanical anchorage can be minimized by manufacturing the anchor's elements with materials of similar hardness, and smoothing and lubricating the sliding surfaces [28].

However, applying lubrication with caution is critical since the friction between the FRP plate and the anchorage is desired to prevent slippage of the FRP plate unlike the friction between the wedges and the barrel of the wedge anchorage.

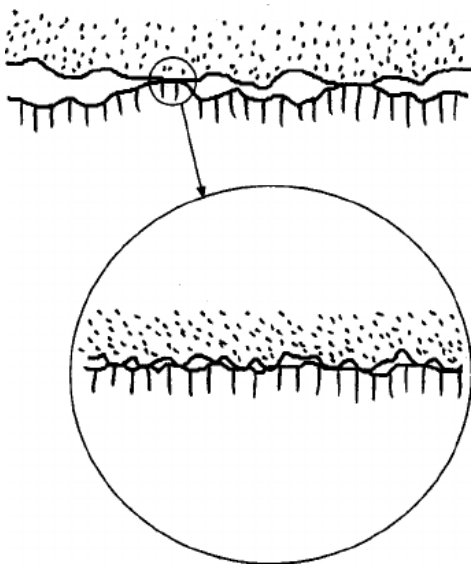

*Figure 2.3: Illustration of Surface Asperities [29]*

### 2.4.2. Resin Bonding

Resin bonding anchoring mechanism is based on a non-mechanical adhesive bond that is created by pouring a resin between the FRP plate and the sleeve of the resin potted anchorage. The roughness of the adhered surface of the sleeve is crucial for enhancing the bond between the resin and the sleeve. Unlike mechanical gripping, resin bonding does not induce lateral loads on the FRP plate, so the occurrence of premature failure within the FRP plate is unlikely. However, the strength of the resin bonding is crucially affected by the curing temperature, the curing period and the surrounding environment and temperature [30]; thus, resin bonding is unreliable in terms of long-term usage.

## 2.5. Common FRP Anchorage Systems

There are numerous existing anchorages; however, the main and most common anchorage systems are clamp anchorages, wedge anchorages and resin potted anchorages. These anchorages utilize different mechanisms to produce the required anchoring strength as described in detail in the following subsections.

### 2.5.1. Clamp Anchorage System

Clamp anchorage system, shown in Figure 2.4, is mainly made of two relatively thick clamping plates fastened together by a certain number of bolts [14]. The FRP plate is first inserted between the clamping plates then the bolts are fastened such that the desired contact pressure is created between the FRP plate and the clamping plates. Normally two thin sleeves made of a soft material, such as copper, are placed between the FRP plate and the clamping plates to improve gripping [20].

The anchoring mechanism of a clamp anchorage is based on uniform gripping of the FRP plate via friction induced by a uniform contact pressure between the FRP plate and the clamp anchorage as shown in Figure 2.5. A clamp anchorage can produce a non-uniform contact pressure across the FRP plate by fastening the bolts differently; however, controlling the induced lateral stress across the FRP plate is complex. Thus, the uniform contact pressure produced by the clamp anchorage can cause stress concentration at the loading edge of the FRP plate leading to premature failure. Despite its simple design, clamp anchorages are also relatively large, heavy and hard to install as regular bolt refastening is required to maintain the contact pressure.

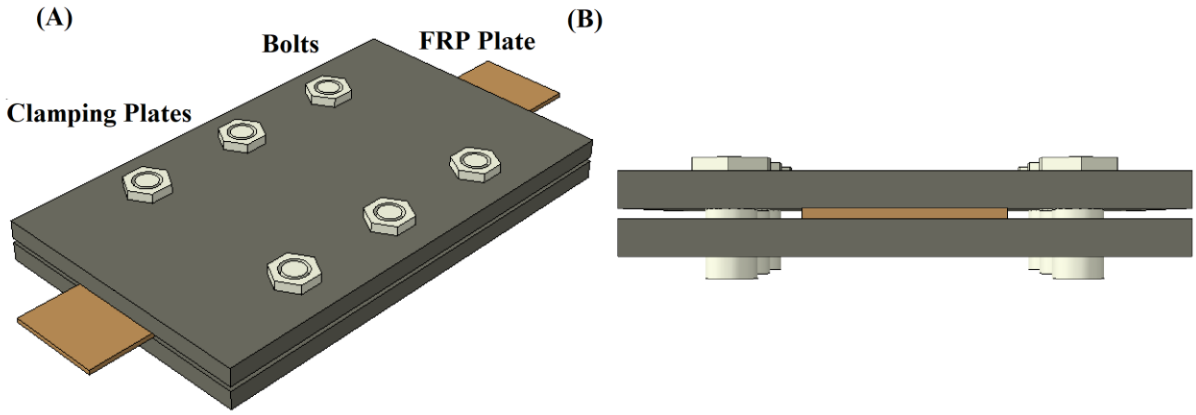


*Figure 2.4: 3D View (A) and Front View (B) of a Clamp Anchorage*

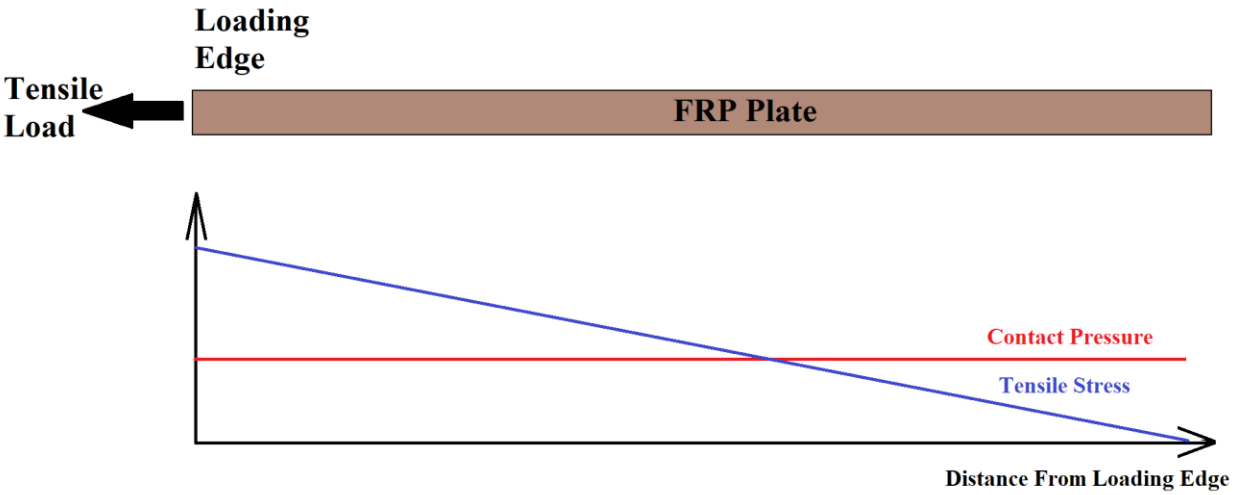


*Figure 2.5: Tensile Load and Contact Pressure Distribution across the Length of the FRP Plate for Clamp Anchorage*

### 2.5.2. Wedge Anchorage System

Wedge anchorage system, shown in Figure 2.6, often consists of two major elements which are a barrel and a certain number of wedges. Wedge anchorage system is commonly utilized to anchor FRP tendons; however, wedge anchorage can be designed to anchor FRP plates as well. The wedge anchorage is assembled by placing the FRP plate between the wedges before presetting the wedges into the barrel. Contact pressure is induced on the FRP plate due to the existing interference between the wedges and the barrel. Two thin sleeves made of a soft material can be inserted between the FRP plate and the wedges to enhance gripping [20].

Unlike the clamp anchorage system, the anchoring mechanism of the wedge anchorage system can produce a precise non-uniform distribution of contact pressure across the FRP plate. This ability gives wedge anchorage an advantage over clamp anchorage as premature failure of FRP plate can be prevented. As illustrated in Figure 2.7, wedge anchorage can minimize the contact pressure at the loading edge of the FRP plate and maximize it around the other edge. This feature allows wedge anchorage to increase the overall gripping strength per contact length without risking premature failure of the FRP plate.

However, due to the existence of high contact pressure between the wedges and the barrel, the contacting surfaces of the wedge and the barrel must be as smooth as possible to the minimize shear stresses. Lubricants can be applied to minimize the friction between the wedges and the barrel even further [28]. While a wedge anchorage system is somewhat complicated to design, it is compact, light in weight, reliable and easy to install since no regular refastening is needed.

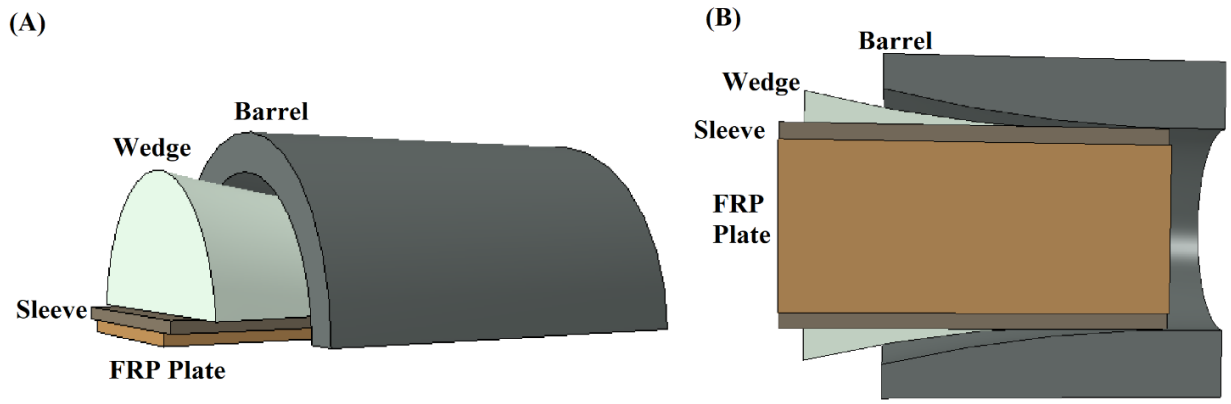


*Figure 2.6: 3D View (A) and Bottom View (B) of Half-Section View of Wedge Anchorage*

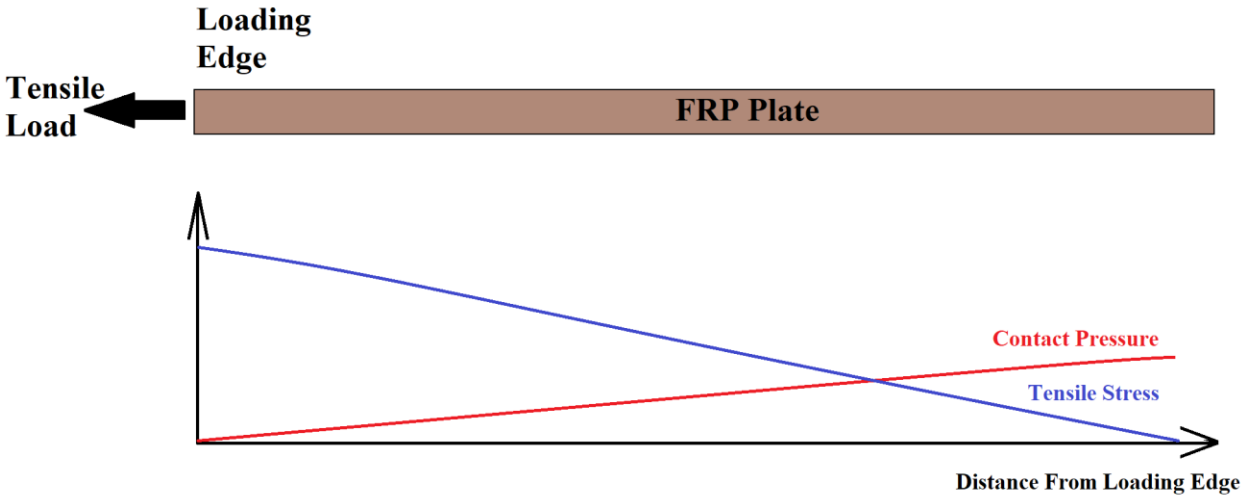


*Figure 2.7: Tensile Load and Contact Pressure Distribution across the Length of the FRP Plate for Wedge Anchorage*

### 2.5.3. Resin Potted Anchorage System

There is a significant number of resin potted anchorages; nevertheless, the common elements of a resin potted anchorage are an outer sleeve and a bonding resin such as cementite or epoxy. The outer sleeve can be designed as straight sleeve or contoured sleeve in order to manipulate the bonding resin distribution across the FRP element as shown in Figure 2.8 and Figure 2.9 respectively. One main advantage of most bonded anchorages over mechanical anchorages is the fact that applying transverse loading on the FRP element is not a necessity to maintain gripping. However, some bonded anchorages use expansive material couplers such as expansive cement which can induce lateral loads on the FRP element [15].

The resistance to surrounding environment as well as the shear strength of the bonding resin are critical factors that can crucially affect the gripping strength and durability of the resin potted anchorage. The roughness of the associated surface of the sleeve is important to enhance the bond between the sleeve and the resin. Controlling the stresses within a resin potted anchorage is difficult [14]; thus, a resin potted anchorage must be designed with caution if expansive materials are to be used as the induced lateral loads on the FRP plate can cause premature failure [15]. The sensitivity of the bonding resin to the surrounding environment and temperature, the lengthy curing time of the bonding material as well as the difficulty of controlling the induced lateral load distribution on the FRP element are the main weaknesses of the resin potted anchorages [14], [30].

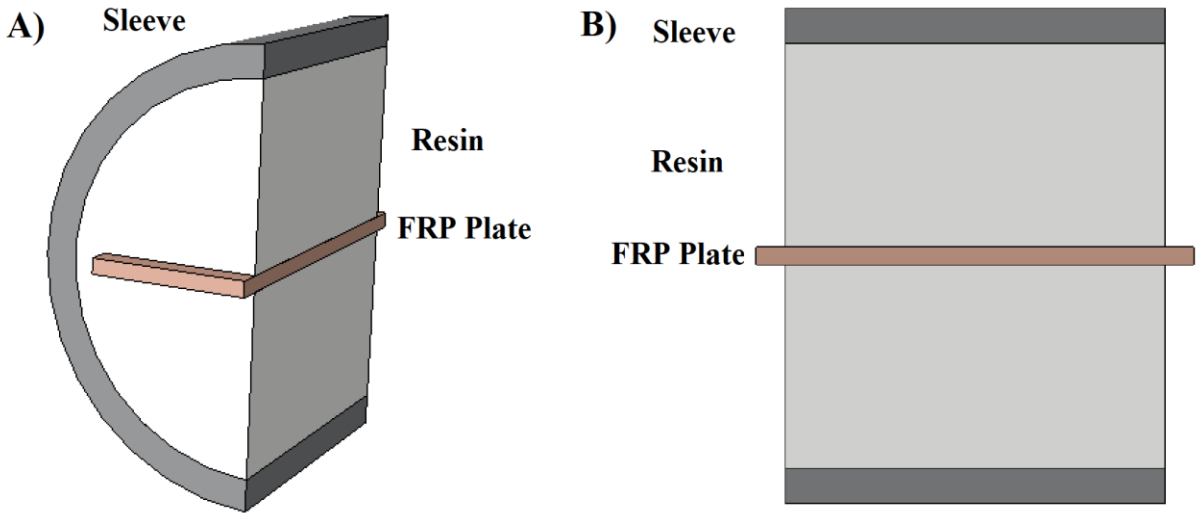


*Figure 2.8: 3D View (A) and Side View (B) of Half-Section View of Straight Sleeve Resin Potted Anchorage*

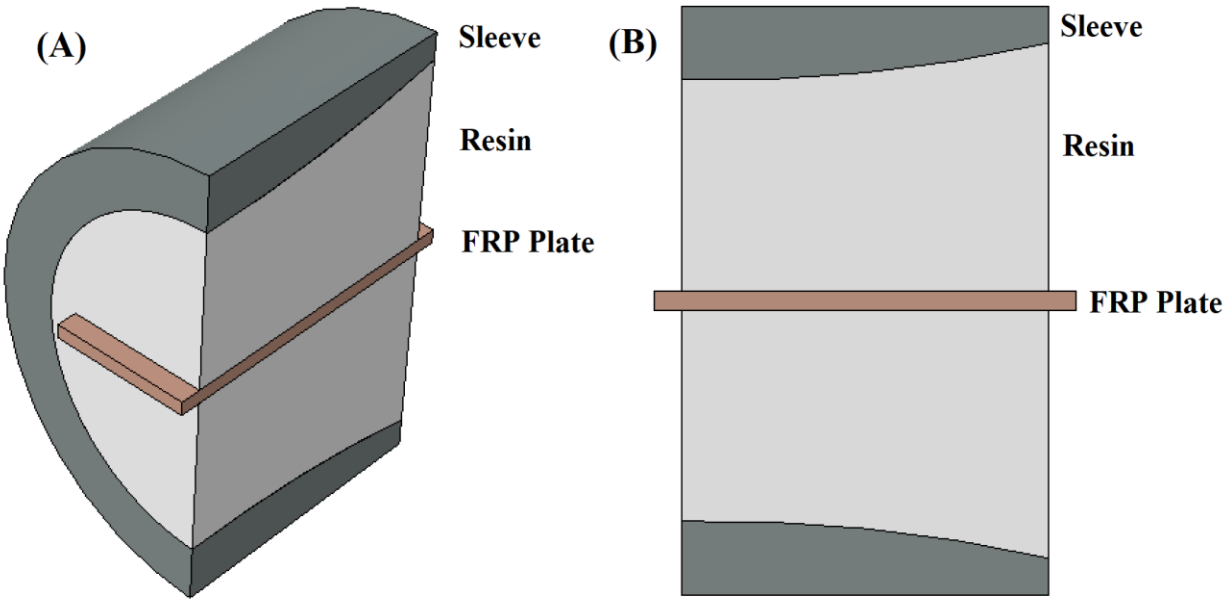


*Figure 2.9: 3D View (A) and Side View (B) of Half-Section View of Contoured Sleeve Bonded Anchorage*

## 2.6. FRP Anchoring Failure Modes

There are several failure modes of an anchorage system. The anchorage failure modes can be divided into short-term and long-term failure modes.

### 2.6.1. Short-Term Failure Modes

The followings are some common short-term failure modes of FRP anchorage systems.

- **Tensile Fracture of FRP Plate**

This the optimal and the desired failure mode where the FRP plates sustain a load of at least 95% of the tensile strength before going though tensile failure [31], [32].

- **Slipping of FRP Plate**

FRP plate slipping occurs in mechanical anchorages when the gripping strength is not sufficiently high to withstand the tensile load [32]. Slipping can be prevented by increasing the contacting area and the contact pressure on the FRP plate.

- **Debonding of FRP Plate**

Debonding failure happens when the tensile loading exceeds the bonding strength [33], [34]. The strength of the resin bond can be gradually deteriorated by the surrounding environment and temperature causing debonding failure during the service life of the resin potted anchorages.

- **Pre-mature Rupture of FRP Plate**

Premature failure of FRP plate occurs in mechanical anchorages when high transverse load is applied around the loading edge of the FRP plate, therefore, creating stress concentration [31]. Unlike tensile fracture of FRP plates, premature failure occurs inside the anchorage system.

- **Fracture of Barrel**

This failure mode occurs in wedge anchorages when the induced tensile hoop stress within the barrel exceeds its strength. Explosive tensile fracture of the barrel is caused by low strength or insufficient thickness of the barrel. It can be prevented simply by increasing the thickness or manufacturing the barrel with a stronger material.

### 2.6.2. Long-Term Failure Modes

- **Corrosion Failure**

Corrosion is an electro-chemical process of gradual deterioration of an element, usually a metal, because of its reaction with the surrounding environment through which electrons are extracted from the element and oxides are created [35], as shown in Figure 2.10. The surroundings of a corroding element may vary; however, the same essential factors must exist for corrosion to occur which are the existence of an electron-donating element, an electron-receiving element, an electrolyte and a driving force in the form of voltage difference [36]. Unlike the mechanical properties of a material, the corrosion resistance of an element is predominantly dependent on the environment it is exposed to [37]. As a result, selecting a material with an appropriate corrosion resistance for a specific application is critical as the material cost increases significantly as the corrosion resistance is improved. Corrosion failure can be prevented or delayed by using corrosion resisting materials, applying inhibitors or protective coatings, and utilizing a sacrificial anode [37].

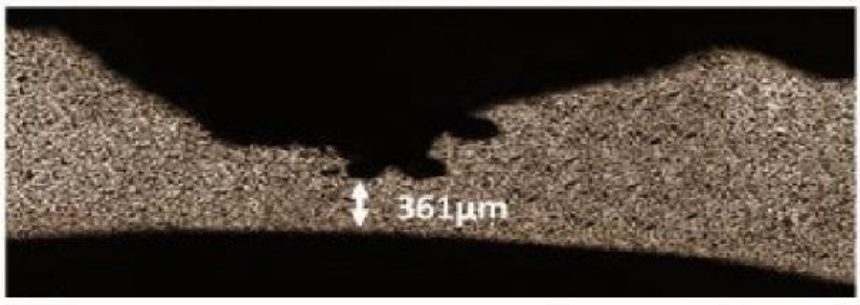


*Figure 2.10: Thickness reduction of a cylinder pipe because of corrosion [38]*

- **Fatigue Failure**

Fatigue is a process of gradual degradation of an element induced by repeated cyclic loading resulting in sudden and rapid fatigue rupture [39]. Cracks are created and propagated within the element during the cyclic loading to a point where concentrated stresses are higher than the static strength of a material; as a result, sudden ductile failure is caused as shown in Figure 2.11. There are three stages of crack growth during the fatigue process, which are microcrack initiation, macrocrack propagation, and final rupture [39]. Fatigue, unlike creep and corrosion, is not detectable; therefore, in addition to applying a sufficient factor of safety, it is important to estimate fatigue life of an element with a satisfactory accuracy. There are several methods to predict the fatigue life of an element such as analyzing the stress/cycle and the strain/cycle curves [40], [41]. In general, any cyclic loading, no matter how low it is, can cause fatigue fracture after a certain number of cycles; however, this is not entirely true for materials that exhibit fatigue limit or endurance limit. Endurance limit is defined as the maximum cyclic loading that an element can be endure indefinitely [42]. The fatigue life under endurance limit cyclic loading is around $1x10^6$ and $1x10^7$ cycles [40], [43]. It is worthy to note that fatigue failure might occur within the FRP anchorage instead of the CFRP plate which has excellent fatigue properties.

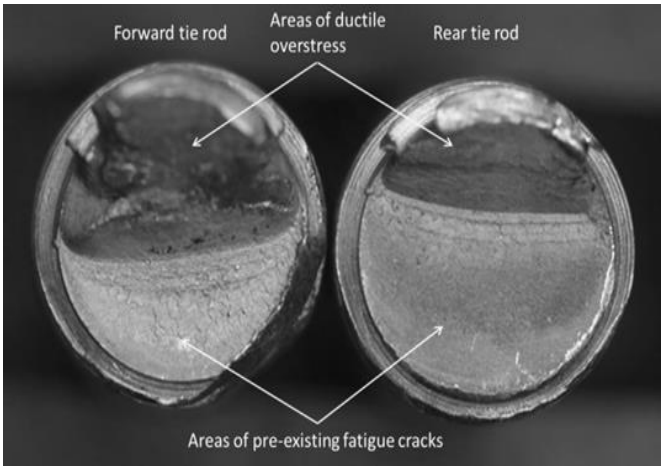


*Figure 2.11: Fatigue Rupture of a Rod [44]*

- **Creep Failure**

Creep is a phenomenon of time-dependent plasticity that occurs when a material is loaded at elevated temperatures during which plastic strain is induced and increased over time even when a relatively low constant load is applied [43], [45]. Creep occurs in metals and ceramics when a material is stressed at a temperature of 30-40% of its melting temperature [43]. The typical behaviour of the time-dependent plasticity of creep when a constant is applied can be divided into three stages which are primary creep, secondary or steady-state creep, and tertiary creep respectively [43], [45]. Creep failure is not experienced only by metals in the form of ductile failure, as shown in Figure 2.12, but also by FRP elements as well as resins [46].

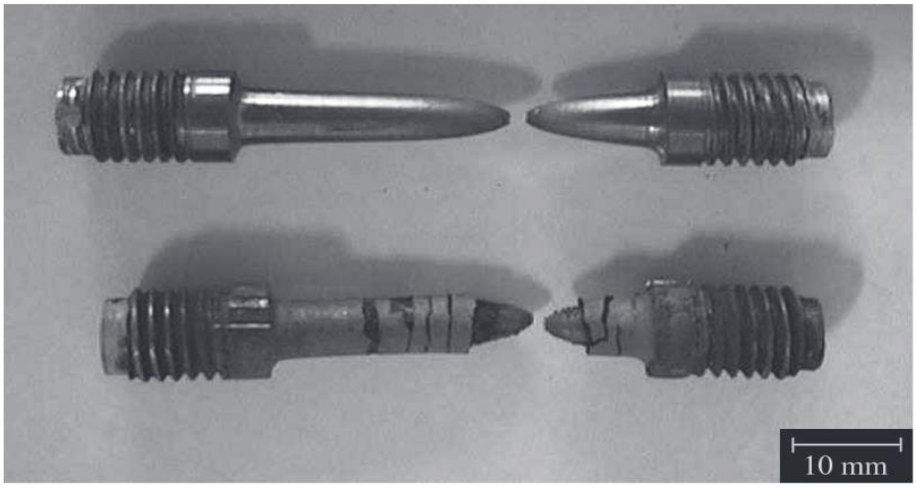


*Figure 2.12: Creep Fracture Elements [47]*

## 2.7. Conclusion

Strengthening structural element, such as concrete beams and slabs, with FRP plates is essential as steel plates are susceptible to corrosion. FRP plates, especially CFRP plates, have an outstanding tensile strength to weight ratio, an excellent corrosion resistance and low stress relaxation; nevertheless, CFRP plates are vulnerable to lateral loads and expensive. To utilize the high strength of CFRP plate and enhance the performance of strengthened structural elements, anchorages systems are utilized to allow prestressing of FRP plates. FRP anchorages along with their anchoring mechanisms are assessed. Anchoring FRP plates with a resin potted anchorage is difficult to apply in the field mainly because of the long resin curing time, and large size. Clamp anchorage is smaller and easier to install than resin potted anchorage; however, regular bolt refastening is required to maintain the performance of the clamp anchorage which makes it expensive in terms of long-term usage. Wedge anchorage is superior to both resin potted anchorage and clamp anchorage as it is more compact, easier to install and handle and cheaper for long-term usage. Also, wedge anchorage can prevent premature failure by controlling the lateral load distribution across the FRP plate. Therefore, wedge anchorage is selected as the most reliable anchorage system. The performance of the wedge anchorage is enhanced by assembling two sleeves made of a soft material between the FRP plate and the wedges. Several failure modes of the anchorage system as well as the main factors that trigger them are discussed. These factors are considered in the material selection process and the optimization process performed in Chapter 3 and Chapter 4 respectively.

# 3

# Material Selection

## 3.1. Introduction

The initial step in designing the optimal wedge anchorage for gripping CFRP plates is to select the most suitable materials for its elements, which are the wedges, the barrel and the sleeves. This chapter starts by presenting the mechanical properties of the anchored CFRP plate and introducing the material selection process of the sleeves, the barrel and the wedges of the anchorage. It concludes by summarizing the results of the material selection process.

## 3.2. Mechanical Properties of Unidirectional CFRP Plate

The anchored unidirectional CFRP plate, called Sika CarboDur type S [48], [49], is manufactured by Sika company. It is 1 m long, 50 mm wide and 1.2 mm thick. The mechanical properties of the CFRP plate are listed in Table 3.1. The mechanical properties of the carbon fiber filaments and the epoxy resin are used to compute the axial and transverse modulus of elasticity, the axial and transverse Poisson's ratios, and the axial and transverse modulus of rigidity of the CFRP plate. The equation parameters presented throughout this section are defined in Table 3.2.

*Table 3.1: Provided Mechanical Properties of CFRP Plate*

| Mechanical Property | Magnitude |
|---|---|
| $\sigma_{T-Axial}\ (MPa)$ | 2800[1] |
| $\sigma_{T-Lateral}\ (MPa)$ | 62[1] |
| $\sigma_{C-Lateral}\ (MPa)$ | 350 |
| $\tau_{f-Axial}\ (MPa)$ | 100[2] |
| $\epsilon_{Ult}\ (\%)$ | 1.7%[1] |
| $E_1\ (MPa)$ | 165,000[1] |
| $\rho\ (\frac{g}{cm^3})$ | 1.5[1] |
| **Volumetric Fraction of Fibers (%)** | >68%[1] |

[1] Sika, Canada [48], [49]

[2] Academic paper titles "Effect of curing conditions on strength development in an epoxy resin for structural strengthening" [30]

*Table 3.2: Defined Equation Parameters*

| Parameter | Definition |
|---|---|
| $V_f$ | Volumetric ratio of the carbon fibers to the composite lamina. |
| $E_1$ | Axial modulus of elasticity of the composite lamina. |
| $E_2$ | Transverse modulus of elasticity of the composite lamina. |
| $E_{f1}$ | Longitudinal modulus of elasticity of the carbon fibers. |
| $E_{f2}$ | Transverse modulus of elasticity of the carbon fibers. |
| $E_m$ | Modulus of elasticity of the epoxy resin. |
| $v_{12}$ | Longitudinal Poisson's ratio of the composite lamina. |
| $v_{23}$ | Transverse Poisson's ratio of the composite lamina. |
| $v_{f12}$ | Longitudinal Poisson's ratio of the carbon fibers. |
| $v_m$ | Poisson's ratio of the epoxy resin. |
| $G_{12}$ | Axial modulus of rigidity of the composite lamina. |
| $G_{23}$ | Transverse modulus of rigidity of the composite lamina. |
| $G_{f12}$ | Longitudinal modulus of rigidity of the carbon fibers. |
| $G_m$ | Modulus of rigidity of the epoxy resin. |
| $\sigma_{C-m}$ | Matrix compressive strength. |
| $\tau_{f-Axial}$ | In-plane shear strength. |
| $\sigma_{C-Axial}$ | Axial compressive strength of CFRP plates. |

*Table 3.3: Mechanical Properties of Carbon Fibers and Epoxy Resin*

| Property | Carbon Fibers | Epoxy Resin |
|---|---|---|
| $\sigma_C$ $(MPa)$ | --------- | 62[1] |
| $E_1$ $(MPa)$ | 230,000[1] | 11,200[1] (tensile) |
| $E_2$ $(MPa)$ | 16,000[2] | 9,600[1] (compressive) |
| $v_{12}$ | 0.35[3] | 0.35[4] |
| $G_{12}$ $(MPa)$ | 8963[2] | 4148 |

[1] Sika, Canada [48], [49]

[2] Academic paper "Effect of curing conditions on strength development in an epoxy resin for structural strengthening" [30]

[3] Academic paper "The elastic properties of carbon fibres and their composites" [50]

[4] Academic paper "Measurement of epoxy resin tension, compression, and shear stress-strain curves over a wide range of strain rates using small test specimens" [51]

As listed in Table 3.3, the carbon fiber filaments and epoxy resin have the same longitudinal Poisson's ratio $v_{12}$; thus, based on the rule of mixture given by equation **(3.1)**, the longitudinal Poisson's ratio of the CFRP plate is the same as that of the carbon fiber filaments and the epoxy resin [50]–[52]. The transverse modulus of elasticity of the CFRP plate is calculated by averaging the results of the Halpin-Tsai and the Hopkins-Chamis methods shown in equations **(3.2)** and **(3.4)** respectively where $\xi = 2$ [30], [53].

$$v_{12} = v_{f12}(V_f) + v_m(1 - V_f) \tag{3.1}$$

$$E_2 = E_m(\frac{1 + \xi\eta V_f}{1 - \eta V_f}) \tag{3.2}$$

$$\eta = \frac{\frac{E_{f2}}{E_m} - 1}{\frac{E_{f2}}{E_m} + \xi} \tag{3.3}$$

$$E_2 = E_m\left[\left(1 - \sqrt{V_f}\right) + \frac{\sqrt{V_f}}{1 - \sqrt{V_f}\left(1 - \frac{E_m}{E_{f2}}\right)}\right] \tag{3.4}$$

Similarly, the longitudinal shear modulus of the CFRP plate is calculated by averaging the results of the Halpin-Tsai and the Hopkins-Chamis methods shown in equations **(3.5)** and **(3.7)** respectively where $\xi = 2$ [30], [53].

$$G_{12} = G_m(\frac{1 + \xi\eta V_f}{1 - \eta V_f}) \tag{3.5}$$

$$\eta = \frac{\frac{G_{f12}}{G_m} - 1}{\frac{G_{f12}}{G_m} + \xi} \tag{3.6}$$

$$G_{12} = G_m \left[ \left(1 - \sqrt{V_f}\right) + \frac{\sqrt{V_f}}{1 - \sqrt{V_f}\left(1 - \frac{G_m}{G_{f12}}\right)} \right] \tag{3.7}$$

The transverse Poisson's ratio $v_{23}$ and the transverse shear modulus $G_{23}$ of the CFRP plate are computed using equations **(3.8)** and **(3.10)** respectively [54].

$$v_{23} = v_{12}\left(\frac{1 - v_{21}}{1 - v_{12}}\right) \tag{3.8}$$

where

$$v_{21} = v_{12}\left(\frac{E_2}{E_1}\right) \tag{3.9}$$

$$G_{23} = \frac{E_2}{2(1 + v_{23})} \tag{3.10}$$

The axial compressive strength of the CFRP plate is calculated using Chamis method shown in equation **(3.11)** [30].

$$\sigma_{C-Axial} = 10\ \tau_{f-Axial} + 2.5\sigma_{C-m} \tag{3.11}$$

The results of the above theoretical analysis are shown in Table 3.4. Note that since the CFRP plate is transversely isotropic, its transverse Poisson's ratio $v_{23}$ is bounded between 0 and 1; therefore, it is acceptable for the transverse Poisson's ratio to exceed a value of 0.5 [50], [55], [56].

*Table 3.4: Calculated Mechanical Properties of CFRP Plate*

| Mechanical Property | Magnitude |
|---|---|
| $\boldsymbol{\sigma_{C-Axial}\ (MPa)}$ | 1155 |
| $\boldsymbol{E_{2,3}\ (MPa)}$ | 13580 |
| $\boldsymbol{v_{12}\ and\ v_{13}}$ | 0.35 |
| $\boldsymbol{v_{23}}$ | 0.523 |
| $\boldsymbol{G_{12}\ and\ G_{13}\ (MPa)}$ | 6386 |
| $\boldsymbol{G_{23}\ (MPa)}$ | 4458 |

## 3.3. Material Selection of Sleeves

Most existing wedge anchorages use sleeves made of a soft material between the FRP element and the wedges to increase the actual contact area and enhance gripping [14], [57], [58]. Sleeves can be manufactured from aluminium or copper [14], [58]. On one hand, aluminium sleeves are vulnerable to corrosion, so they are unreliable for long-term applications. On the other hand, copper sleeves are corrosion resistant. Thus, copper sleeves are preferred for anchoring CFRP plates effectively throughout the service life of the wedge anchorage.

The anchoring strength achieved using annealed copper sleeves is proven to be higher than that reached using hard copper sleeves [58]. This is due to the fact that a softer sleeve would fill the surface asperities of the wedge and the CFRP plate; as a result, more shear, or gripping, is produced. Therefore, annealed copper is selected to manufacture the sleeves. Thin annealed copper sleeves are purchased from McMaster-Carr [59]. The copper sleeves are 75 mm long, 0.81 mm thick and 50 mm wide. The mechanical properties of the annealed copper sleeves are listed in Table 3.5.

The occurrence of excessive plastic deformation within the sleeves is predicted since they are soft; thus, the sleeves must be replaced after each test to maintain the performance of the wedge anchorage. This is not a concern, however, as the annealed copper sleeves are low in cost compared to the overall cost of the wedge anchorage, and they do not require machining.

*Table 3.5: Mechanical Properties of an Annealed Copper Sleeve*

| Mechanical Property | Magnitude |
|---|---|
| $\sigma_{Ult}\ (MPa)$ | 236.49[1] |
| $\sigma_{Y}\ (MPa)$ | 87.56[1] |
| $\sigma_{C}\ (MPa)$ | 87.56[1] |
| $\tau_{f}\ (MPa)$ | 50.52 |
| $\epsilon_{Ult}\ (\%)$ | 45%[2] |
| $E_1, E_2\ and\ E_3\ (MPa)$ | 117,210[2] |
| $v_{12}\ , v_{13}\ and\ v_{23}$ | 0.33 |
| $G_{12}, G_{13}\ and\ G_{23}\ (MPa)$ | 44,000[1] |
| $\rho\ (\frac{g}{cm^3})$ | 8.913[2] |

[1] Aurubis, Germany [60]

[2] McMaster-Carr, United States [59]

## 3.4. Material Selection of Barrel and Wedges

Manufacturing the barrel and the wedges of the anchorage with the most suitable materials is an extremely vital step as that will reflect on its anchoring strength, reusability, durability, weight and cost. The wedge anchorage must have sufficient stiffness to produce an adequate anchoring strength, high strength to endure the induced stresses, and suitable hardness to minimize local plastic deformation in addition to an excellent corrosion resistance to withstand detrimental environments. Minimizing the plastic deformation within an anchorage is critical to improve its reusability making it more cost-efficient. The corrosion resistance is an essential factor when dealing with corrosive environments as corrosion is crucially affected by the surrounding environment, and it is almost undetectable in the field which would result in a sudden failure of the wedge anchorage as well as the reinforced concrete structure. Creep and fatigue are considered as additional factors that can be considered in future investigations.

Different stainless-steel families are considered in the material selection process including austenitic stainless steel, ferritic stainless steel, and martensitic stainless steel. Some of the common stainless-steel grades along with their major properties are listed in Table 3.6. Since high corrosion resistance is desired, the corrosion resistant grades are picked for comparison. The yield strength and tensile strength of the corrosion resistant grades are shown in Table 3.7. Based on Table 3.7, the 440 grade of stainless steel has both an excellent corrosion resistance as well as superior yield and tensile strengths.

This grade of stainless steel is divided into three different grades which are 440A, 440B and 440C. While quenched 440C grade has slightly lower corrosion resistance compared to 440A and 440B grades, it has the highest tensile strength and yield strength as shown in Table 3.8 [61]. The corrosion resistance of the 440C grade is suitable for usage in concrete structures as the surrounding environment is not highly corrosive. Thus, the 440C grade of stainless steel is selected as the optimal material for manufacturing the wedges and the barrel of the wedge anchorage. It is worth mentioning that regular steel with comparable mechanical properties can be used to examine the performance of the wedge anchorage. Note that the wedges and the barrel are manufactured with the same material to minimize surface ploughing. The mechanical properties of 440C stainless steel are summarized in Table 3.9.

*Table 3.6: Common Stainless-Steel Grades [62]*

| Austenitic Stainless Steel | | |
|---|---|---|
| **Basic Grade** | **Property** | **Grades** |
| 304 | High Temperature Resistant | 310 |
| | Corrosion Resistant | 316, 317 |
| | Weld Stabilized | 304L, 316L, 321 |
| | Free Machining | 303 |
| **Ferritic Stainless Steel** | | |
| **Basic Grade** | **Property** | **Grades** |
| 430 | Corrosion Resistant | 444 |
| | High Toughness | 409 |
| | Free Machining | 430F |
| **Martensitic Stainless Steel** | | |
| **Basic Grade** | **Property** | **Grades** |
| 410 | Corrosion Resistant | 431, 440A, 440B, 440C |
| | High Hardness | 420 |
| | Free Machining | 416 |

*Table 3.7: Yield Strength and Tensile Strength of Corrosion Resistant Stainless-Steel Grades*

| Grade | Yield Strength (MPa) | Tensile Strength (MPa) |
|---|---|---|
| 316[1] | 200 – 331 | 579 – 621 |
| 317[1] | 262 – 373 | 593 – 662 |
| 431[1] | 665 | 850 – 1000 |
| 440[1] | 414 – 1896 | 724 – 1965 |
| 444[2] | 360 | 515 |

[1] Atlas Steels Company [61], [63]

[2] AK Steel Holding Company [64]

*Table 3.8: Yield Strength and Tensile Strength of 440A, 440B and 440C Stainless-Steel Grades [61]*

| Grade | Yield Strength (MPa) | Tensile Strength (MPa) |
|---|---|---|
| 440A | 1655 | 1793 |
| 440B | 1862 | 1931 |
| 440C | 1896 | 1965 |

*Table 3.9: Mechanical Properties of 440C Stainless Steel*

| Mechanical Property | Magnitude |
|---|---|
| $\sigma_{Ult}\ (MPa)$ | 1965[1] |
| $\sigma_{Y}\ (MPa)$ | 1896[1] |
| $\tau_{f}\ (MPa)$ | 948[3] |
| $\epsilon_{Ult}\ (\%)$ | 2%[1] |
| $E_1, E_2\ and\ E_3\ (MPa)$ | 200,000[2] |
| $v_{12}\ , v_{13}\ and\ v_{23}$ | 0.28[2] |
| $G_{12}, G_{13}\ and\ G_{23}\ (MPa)$ | 78,125[3] |
| $\rho\ (\frac{g}{cm^3})$ | 7.8[2] |

[1] Nickel Development Institute, Canada [61]

[2] AZoM online publication for the Materials Science community [65]

[3] Calculated analytically

## 3.5. Summary

This chapter introduced the material selection process for the sleeves as well as the wedges and the barrel of the wedge anchorage. Annealed copper is selected the preferable sleeve material as it is soft and corrosion resistant. Several stainless-steel grades are considered for manufacturing the wedge and the barrel of the wedge anchorage. The 440C grade of stainless steel is found as the most suitable material as it has an excellent corrosion resistant and outstanding yield and tensile strengths. The mechanical properties of the CFRP plate, the annealed copper sleeves, and the 440C stainless-steel barrel and wedges are presented. These mechanical properties are used throughout this thesis.

# 4

# Finite Element Modelling

## 4.1. Introduction

This chapter introduces the development process of the FEM model as well as its role in the optimization of the wedge anchorage. It starts by discussing several parameters considered in constructing the FEM model. Convergence analysis is conducted to identify the most suitable mesh size through which accurate results are obtained in a timely manner. An optimization process is performed to identify the optimal dimensions of the wedge anchorage in terms of improving the gripping strength, enhancing the reusability and minimizing the size and cost of the wedge anchorage. The occurrence of premature failure within the CFRP plate is investigated using several FRP failure theories. Finally, the effect of the presetting distance on the contact pressure across the CFRP plate and the stresses within the wedge anchorage is investigated.

## 4.2. Parameters of Finite Element Model

### 4.2.1. Model Configuration

The designed wedge anchorage consists of a CFRP plate, two annealed copper sleeves, two 440C stainless steel wedges and a 440C stainless steel barrel, as shown in Figure 4.1. The outer surface of the wedges and the inner surface of the barrel are made of two profiles which are a circular profile and a linear profile. The configuration parameters of the constructed wedge anchorage are listed below:

$\boldsymbol{Edge\ 1}$ : The loading edge of the wedge anchorage.

$\boldsymbol{Edge\ 2}$ : The presetting edge of the wedge anchorage.

$\boldsymbol{r}$ : The radius of the circular profile of the barrel and the wedges.

$\boldsymbol{L_1}$ : The length of the circular segment of the barrel and the wedges.

$\boldsymbol{L_2}$ : The length of the linear segment of the barrel and the wedges.

$\boldsymbol{W_1}$: The diameter of the wedges including the thickness of the CFRP plate and the two sleeves at the loading edge (edge 1).

$\boldsymbol{W_2}$: The diameter of the wedges including the thickness of the CFRP plate and the two sleeves at the intersection between the circular profile and the linear profile.

$\boldsymbol{W_3}$: The diameter of the wedges including the thickness of the CFRP plate and the two sleeves at the presetting edge (edge 2).

$\boldsymbol{B_1}$ : The inner diameter of the barrel at the loading edge (edge 1).

$\boldsymbol{B_2}$ : The inner diameter of the barrel at the intersection between the circular profile and the linear profile.

$\boldsymbol{B_3}$ : The inner diameter of barrel at the presetting edge (edge 2).

$\boldsymbol{T}$ : The thickness of the CFRP plate and the two sleeves combined.

$\boldsymbol{t}$ : The thickness of the barrel at the presetting edge (edge 2).

$\boldsymbol{\theta_W}$ : The slope angle of the linear profile of the wedges.

$\boldsymbol{\theta_B}$ : The slope angle of the linear profile of the barrel.

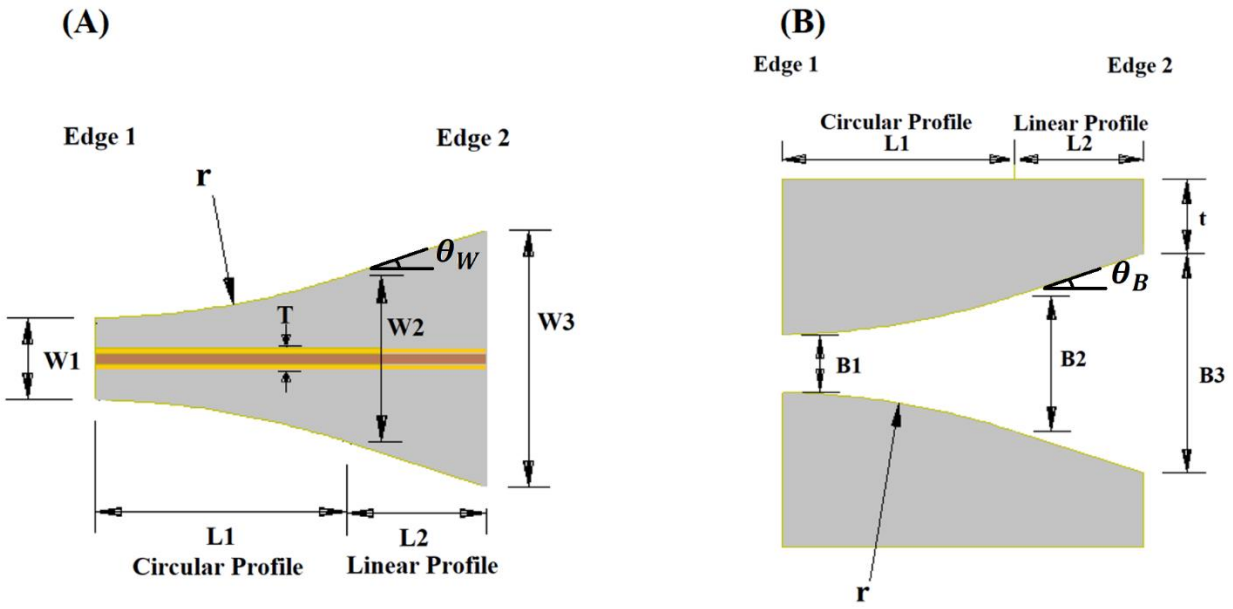


*Figure 4.1: (A) Configuration of Wedges, CFRP Plate and Sleeves. (B) Configuration of Barrel.*

The FEM model of the wedge anchorage, shown in Figure 4.2, is developed using ABAQUS software. Both the standard program and the explicit program of ABAQUS can accurately simulate a quasi-static wedge anchorage system; nevertheless, the explicit program is used as it requires less disk storage and computational power compared to the standard program [66]. Using symmetry, a quarter section of the wedge anchorage is modelled. Hence, half-thickness CFRP plate, one sleeve and one wedge are assembled inside the barrel such that the closest distance between the wedge and the barrel is less than 10 $\mu m$ to increase the precision of the presetting distance analysis.

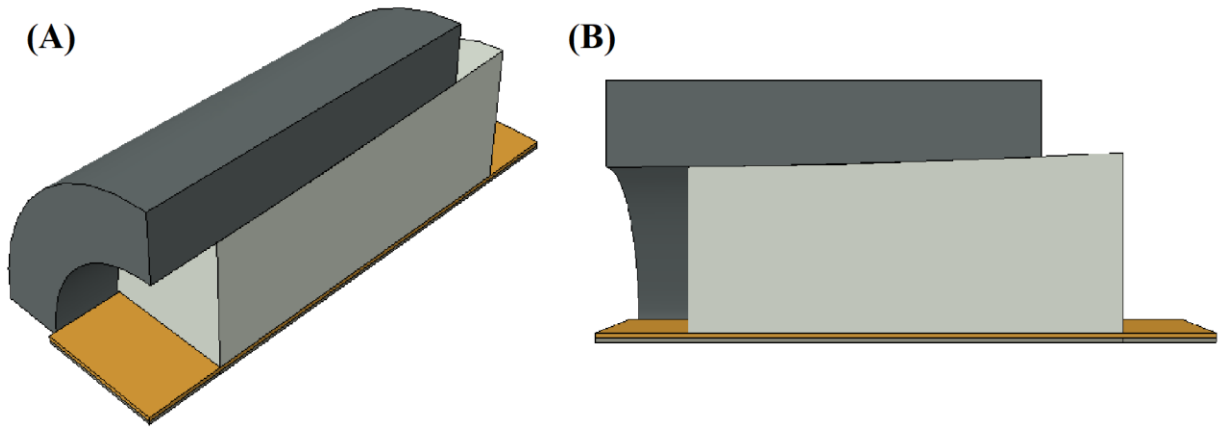


*Figure 4.2: 3D View (A) and Side View (B) of Wedge Anchorage*

### 4.2.2. Material Properties

The mechanical properties of the CFRP plate, the annealed copper sleeves, and the 440C stainless steel wedges and barrel, previously shown in Chapter 3, are listed in Table 4.1.

*Table 4.1: Mechanical Properties of CFRP Plate, Annealed Copper Sleeves and 440C Stainless Steel Wedges and Barrel*

| Properties | CFRP Plate | Annealed Copper Sleeves | 440C Stainless Steel Wedges/Barrel |
|---|---|---|---|
| $\sigma_{T-Axial}\ (MPa)$ | 2800[1] | 236.49[2] | 1965[4] |
| $\sigma_{C-Axial}\ (MPa)$ | 1155[7] | 236.49[2] | 1965[4] |
| $\sigma_{T-Lateral}\ (MPa)$ | 62[1] | 236.49[2] | 1965[4] |
| $\sigma_{C-Lateral}\ (MPa)$ | 350 | 236.49[2] | 1965[4] |
| $\sigma_{Y}\ (MPa)$ | ----- | 87.56[2] | 1896[4] |
| $\tau_{f}\ (MPa)$ | 100[6] | 43.78[7] | 948[7] |
| $\epsilon_{Ult}\ (\%)$ | 1.7%[1] | 45%[3] | 2%[4] |
| $E_1\ (MPa)$ | 165,000[1] | 117,210[3] | 200,000[5] |
| $E_{2,3}\ (MPa)$ | 13580[7] | 117,210[3] | 200,000[5] |
| $v_{12}\ and\ v_{13}$ | 0.35[7] | 0.33[7] | 0.28[5] |
| $v_{23}$ | 0.523[7] | 0.33[7] | 0.28[5] |
| $G_{12}\ and\ G_{13}\ (MPa)$ | 6386[7] | 44,000[2] | 78,125[7] |
| $G_{23}\ (MPa)$ | 4458[7] | 44,000[2] | 78,125[7] |
| $\rho\ (\frac{g}{cm^3})$ | 1.5[1] | 8.913[3] | 7.8[5] |
| **Volumetric Fraction of Fibers (%)** | >68%[1] | NA | NA |

[1] Sika, Canada [48], [49]

[2] Aurubis, Germany [60]

[3] McMaster-Carr, United States [59]

[4] Nickel Development Institute, Canada [61]

[5] AZoM online publication for the Materials Science community [65]

[6] Academic paper titles "Effect of curing conditions on strength development in an epoxy resin for structural strengthening" [30]

[7] Calculated analytically as explained in Chapter 3.

### 4.2.3. Boundary Conditions

In general, the loading edge (edge 1) of the barrel, shown in Figure 4.3 (A), is theoretically the only part of the anchorage that is fixed during the presetting and loading processes. In real life applications, the anchorage might be constrained more for safety purposes; however, that should not affect the performance of the anchorage greatly. In order to minimize the computational power needed, the symmetry of the wedge anchorage across the transverse axes is utilized, and two roller boundary conditions are introduced as illustrated in Figure 4.3 (B and C).

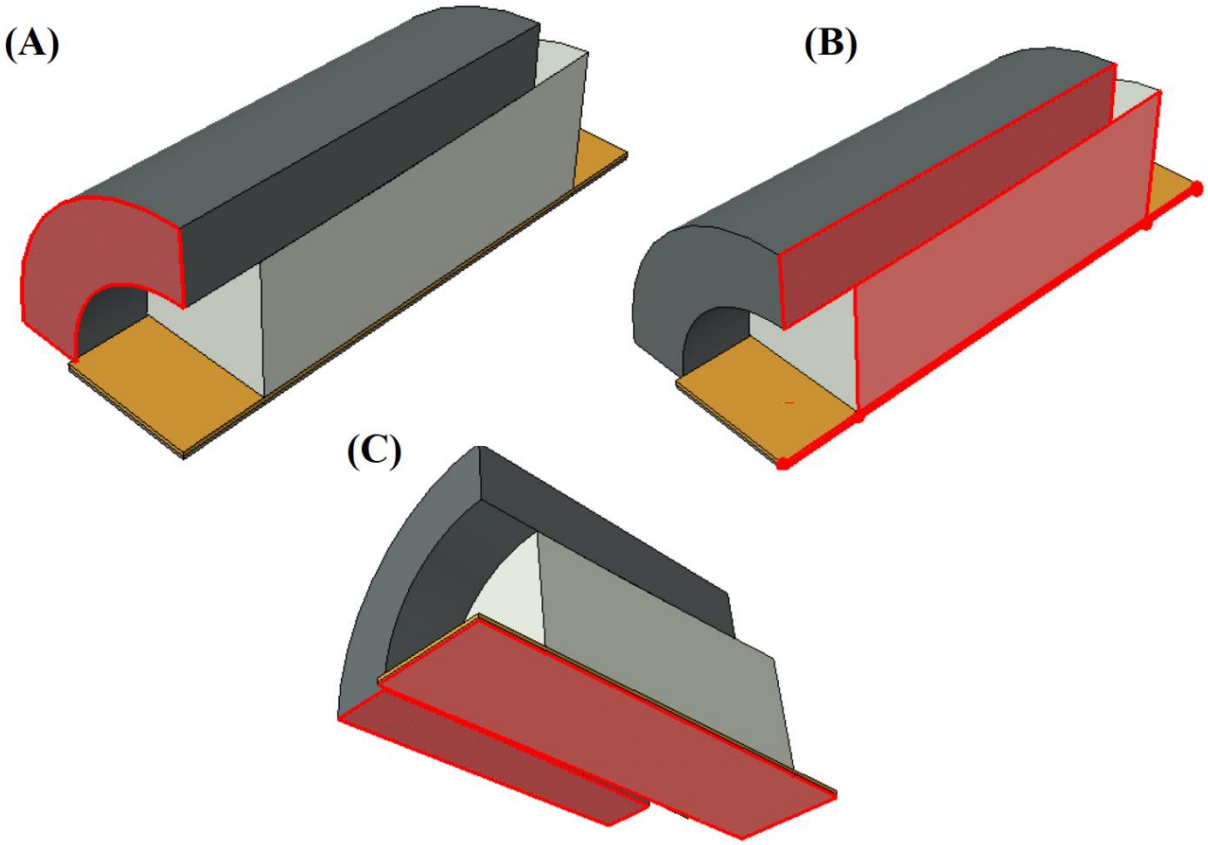


*Figure 4.3: (A) Fixed Loading Edge of the Barrel. (B) Roller Boundary Condition Along the Horizontal Transverse Axis. (C) Roller Boundary Condition Along the Vertical Transverse Axis*

### 4.2.4. Surface Contact Conditions

Three surface interactions are modelled between the four components of the FEM model. The surface interactions are between the top surface of the CFRP plate and the bottom surface of the sleeve, the top surface of the sleeve and the bottom surface of the wedge, the outer surface of the wedge and the inner surface of the barrel as shown in Figure 4.4 (A, B and C) respectively. While a rough friction model is applied at the wedge-sleeve interface, friction coefficients of 0.39 and 0.05 are applied at the CFRP-sleeve interface and the lubricated barrel-wedge interface, respectively [67], [68]. A hard contact is applied to all interacting surfaces to minimize penetration [69]. The surface contact conditions of the interacting surfaces are summarized in Table 4.2.

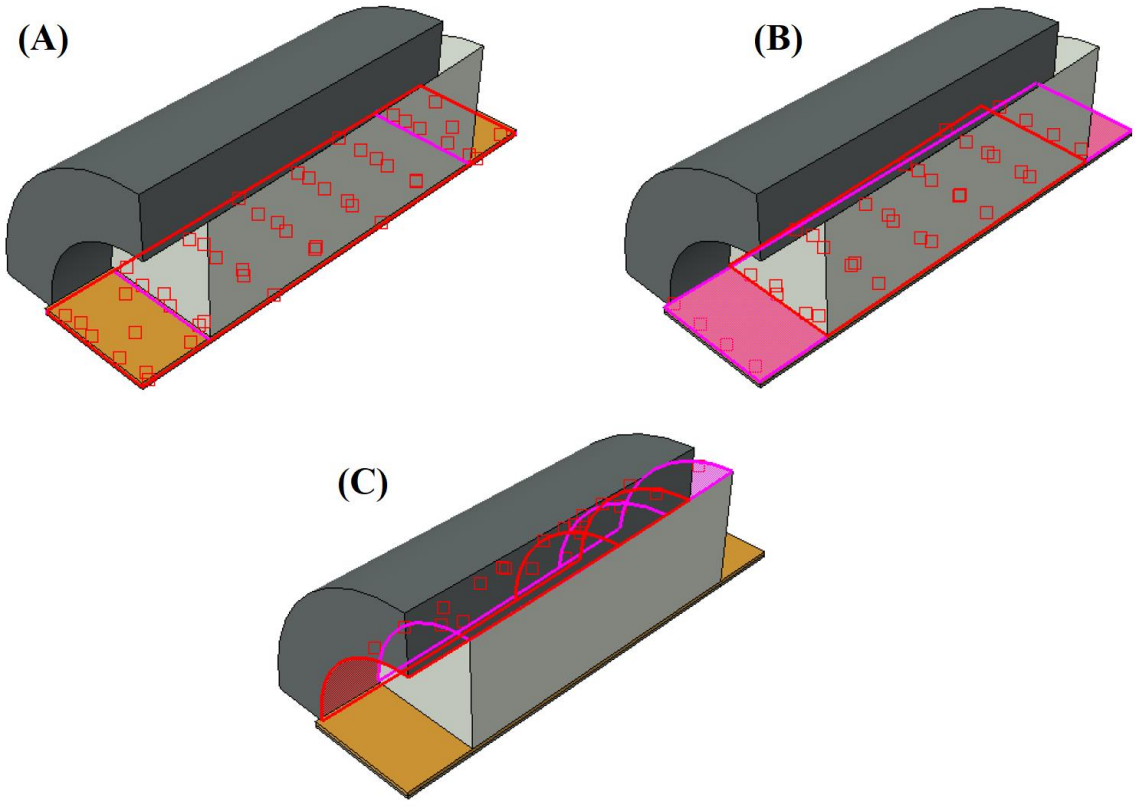


*Figure 4.4: Surface Interactions Between Top Surface of CFRP plate and Bottom Surface of Sleeve (A), Top Surface of Sleeve and Bottom Surface of Wedge (B), and Outer Surface of Wedge and Inner Surface of Barrel (C).*

*Table 4.2: Contact Conditions of Interacting Conditions*

| Property | Interaction 1 | Interaction 2 | Interaction 3 |
|---|---|---|---|
| **Master Surface** | Sleeve – Bottom | Wedge – Bottom | Barrel – Inner |
| **Slave Surface** | CFRP Plate – Top | Sleeve – Top | Wedge – Outer |
| **Normal Behavior** | Hard Contact | Hard Contact | Hard Contact |
| **Tangential Behavior** | Penalty | Rough | Penalty |
| **Friction Coefficient** | 0.39 | ----- | 0.05 |

### 4.2.5. Steps of FEM Model

As discussed in Chapter 2, the anchoring process of a CFRP plate with a wedge anchorage is composed of two steps which are presetting the wedges into the barrel and applying tensile loading on the CFRP plate. Thus, the anchoring process of the wedge anchorage is modelled as two steps, namely: presetting and loading steps. During the presetting step, the wedge is pushed into the barrel through controlled displacement, as shown in Figure 4.5 (A). The insertion distance during the presetting step is critical as high presetting can significantly intensify the internal stresses within the anchorage leading to excessive plastic deformation. The presetting distance is initially assumed as 6 mm during the anchorage optimization process explained in Section 4.4; however, the effect of the presetting distance is further investigated in Section 4.5.4 where different presetting distances ranging from 2 mm to 10 mm are applied. During the loading step, a linearly increasing tensile loading is applied on the cross-sectional area of CFRP plate as shown in Figure 4.5 (B).

The time periods of the presetting step and loading step are 5 seconds and 10 seconds respectively. A mass scaling of 500,000 is applied throughout both steps to shorten the running time of the program. In order to minimize the dynamic error, it is important to maintain the model in a quasi-static condition [70]. The quasi-static condition of the FEM model is tested by plotting the internal energy and the kinetic energy as shown in Figure 4.6.

The kinetic energy of the model is negligible compared to its internal energy; therefore, the model is in a quasi-static condition. The properties of the presetting step and the loading step are summarized in Table 4.3.

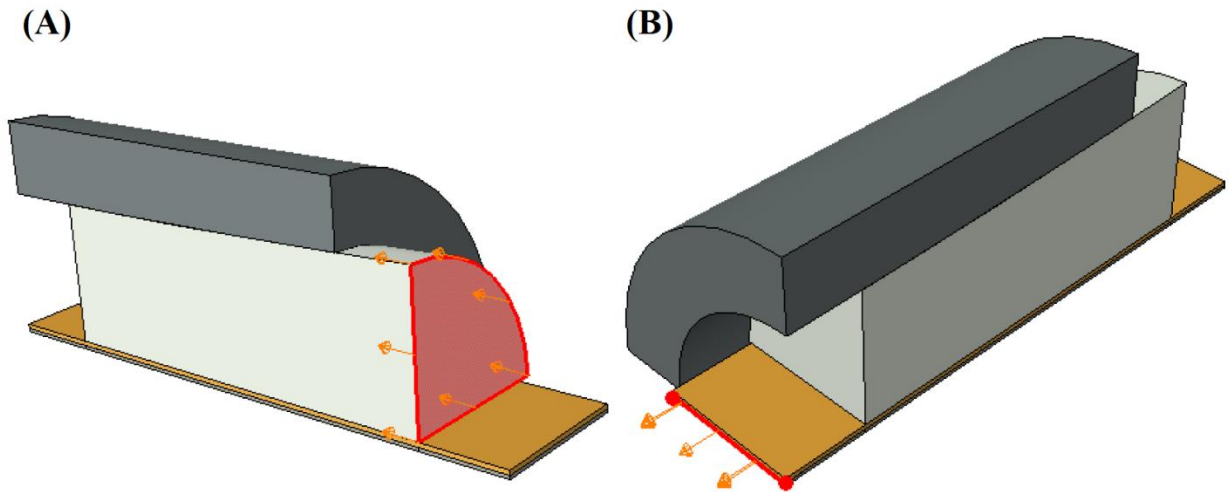


*Figure 4.5: (A) Wedge Insertion During Presetting Step. (B) Applying Tensile Loading on the CFRP Plate During the Loading Step*

*Table 4.3: Properties of Presetting Step and Loading Step*

| Property | Presetting Step | Loading Step |
|---|---|---|
| **Step Period (s)** | 5 | 10 |
| **Loading Type** | Displacement | Uniform Tensile Stress |
| **Load Magnitude** | 6 mm | 2800 MPa |
| **Mass Scaling** | 500,000 | 500,000 |

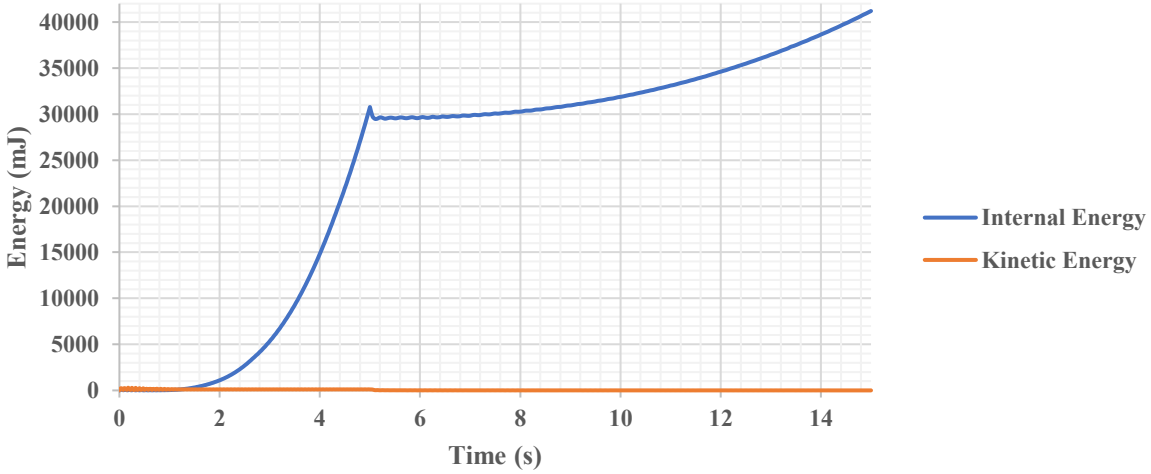


*Figure 4.6: The Internal Energy and Kinetic Energy vs Total Step Time of the FEM Model*

## 4.3. Convergence Analysis

Performing convergence analysis is important to identify the optimal mesh size through which accurate results are obtained in a timely manner. Different mesh sizes ranging from 4 mm to 1 mm are tested using 8-node linear brick elements (C3D8), and the von Mises stress within the barrel and the wedges is recorded to confirm convergence of the FEM model. Note that stress concentration exists within the wedge; therefore, the results obtained from the stress concentration region are divergent. Thus, the von Mises stress within the wedge is collected from an area that is affected slightly by the stress concentration. The von Mises stress within the barrel and the wedge computed using different mesh sizes is shown in Figure 4.7 and Figure 4.8 respectively. It is clear that the von Mises stress within the barrel is much more convergent than the von Mises stress within the wedge due to the absence of stress concentration. However, the stresses in both parts appear to converge as the mesh size is reduced from 3 mm to 1 mm.

To make convergence analysis more precise, the maximum von Mises stress within the barrel and the wedge is plotted against the number of elements of the associated part, and the results are displayed in Figure 4.9 and Figure 4.10 respectively. It can be concluded that the FEM model is convergent, and the optimal mesh size is 2 mm in terms of acquiring accurate results while requiring minimal computational power. Thus, the optimal mesh size is used throughout this chapter.

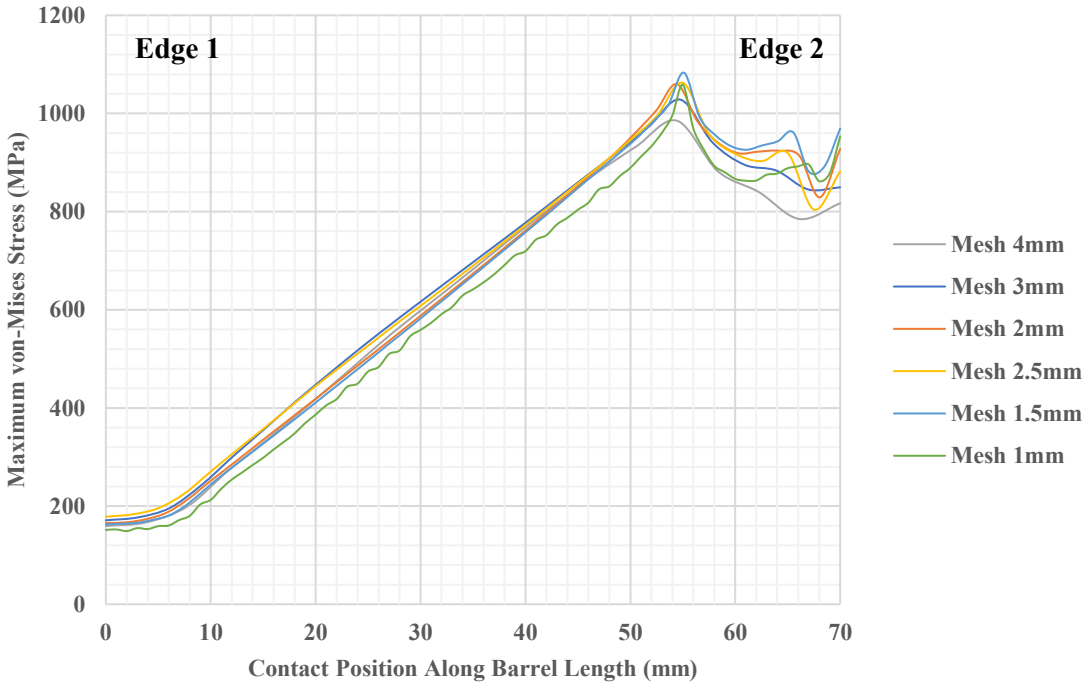


*Figure 4.7: Maximum von Mises Stress Across the Length of the Barrel at Different Mesh Sizes*

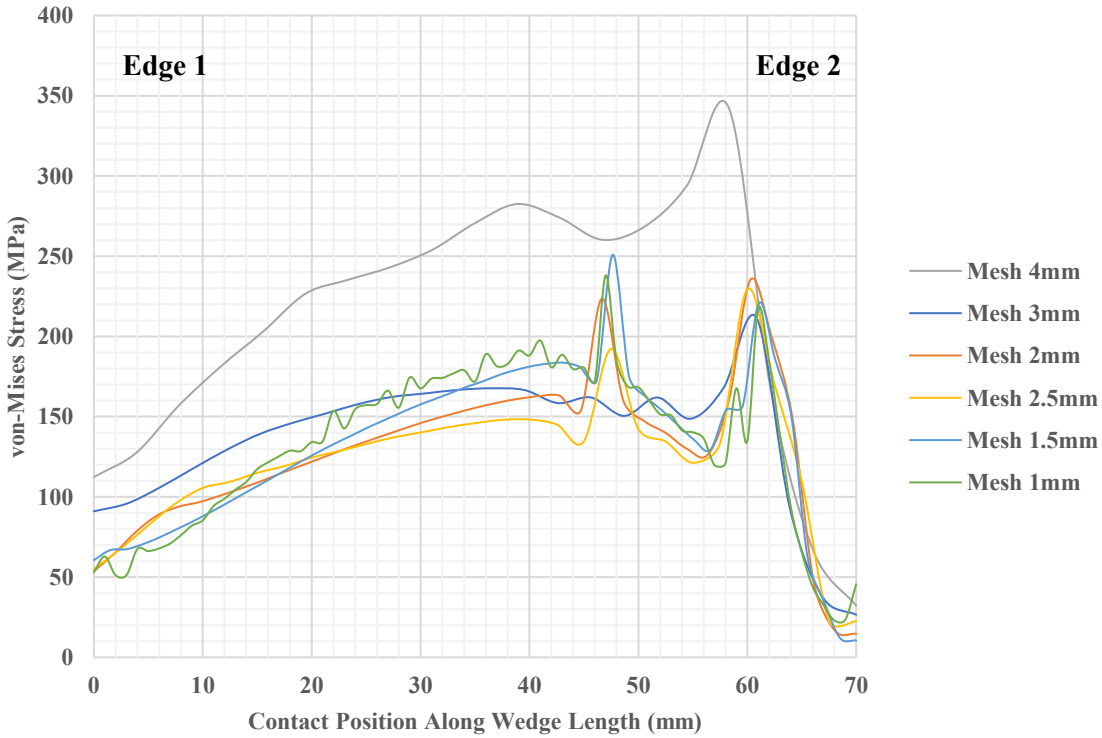


*Figure 4.8: von Mises Stress Across the Length of the Wedge at Different Mesh Sizes*

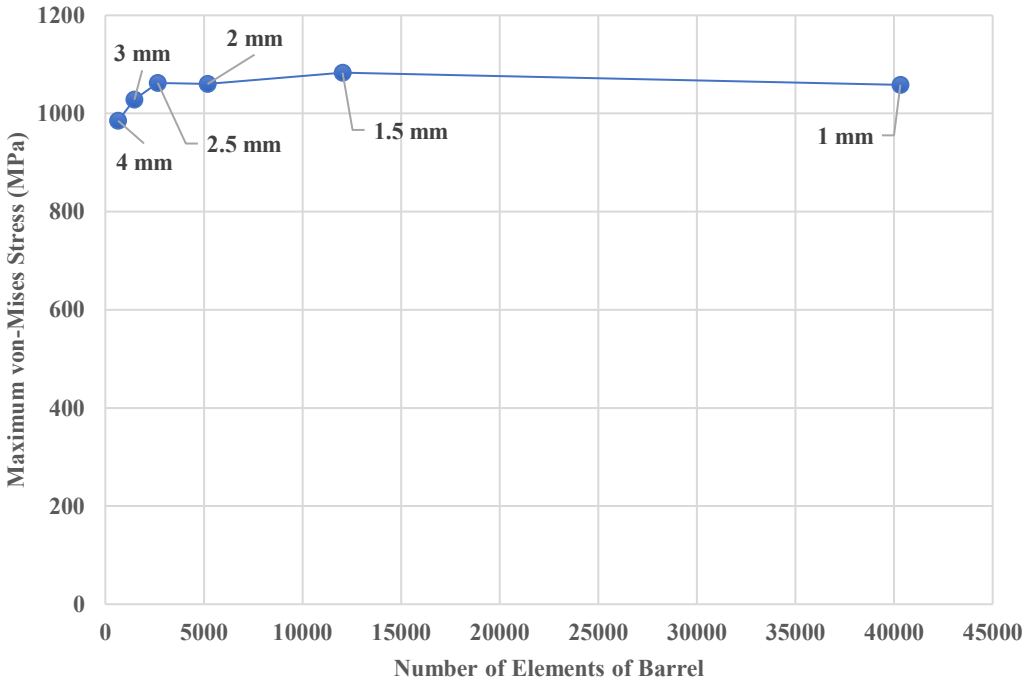


*Figure 4.9: Maximum von Mises Stress Within the Barrel at Different Mesh Sizes*

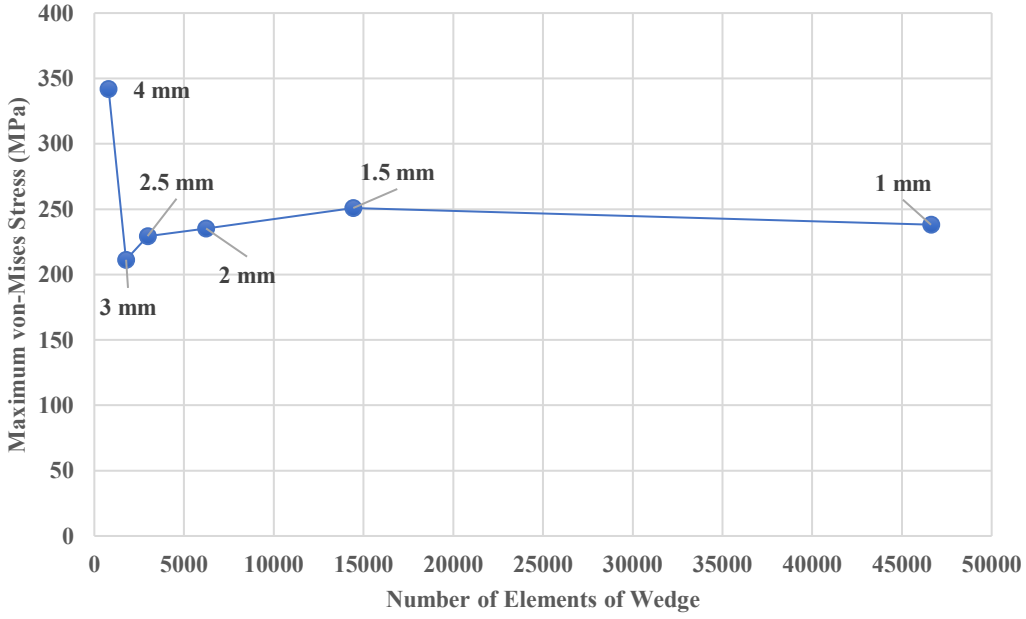


*Figure 4.10: Maximum von Mises Stress Within the Wedge at Different Mesh Sizes*

## 4.4. Optimization Process of Wedge Anchorage

An initial anchorage model is designed then optimized with respect to three optimization parameters which are the slope of linear segments, the radius of circular segments, and the lengths of linear and circular segments. Different sequences of the optimization parameters are used; however, the same optimized design is reached. Each model is evaluated based on the averaged gripping strength of the anchorage, the maximum von Mises stress in both the barrel and the wedges, and the maximum strain of the CFRP plate. This strain is used as a quick method to predict premature failure during the optimization process only. Various FRP failure criteria are applied in Section 4.5.5 to confirm that premature failure of the CFRP plate is unlikely.

### 4.4.1. Optimization of Slope of Linear Segment

The effect of the slope of the linear segments of the barrel and the wedges is investigated. Several FEM models are developed with different combination of slopes of the linear segments. The radius of the circular profiles (r), the length of the circular segments (L1), and the length of the linear segments (L2) are assumed as 1500 mm, 50 mm, and 20 mm respectively. The remaining dimensions of the FEM models are summarized in Table 4.4.

*Table 4.4: Dimensions of Models Considered in the Optimization of Linear Segment Slope*

| Model | W1 (mm) | W2 (mm) | W3 (mm) | $\theta_W$ (Degrees) | B1 (mm) | B2 (mm) | B3 (mm) | $\theta_B$ (Degrees) |
|---|---|---|---|---|---|---|---|---|
| **1** | 25.55 | 26.766 | 27.165 | 1.146 | 25.5 | 26.333 | 26.67 | 0.945 |
| **2** | 25.55 | 26.766 | 27.588 | 2.353 | 25.5 | 26.333 | 27 | 1.909 |
| **3** | 25.55 | 26.766 | 28.01 | 3.56 | 25.5 | 26.333 | 27.34 | 2.873 |
| **4** | 25.55 | 26.766 | 27.433 | 1.909 | 25.5 | 26.333 | 27 | 1.909 |
| **5** | 25.55 | 26.766 | 27.588 | 2.353 | 25.5 | 26.333 | 27.16 | 2.353 |

The slopes of the linear segments of Model 2 are parallel to that of the circular profiles. The slopes of the linear segments are decreased and increased slightly to design Model 1 and Model 3, respectively.

Model 4 and Model 5 are designed such that the interference between the barrel and the wedges is uniform across the linear segments, which is achieved by designing the barrel and the wedges with the same linear segment slope. The slope of the linear segment of the barrel of Model 2 is used for the linear segment of the wedge to design Model 4 while the slope of the linear segment of the wedges of Model 2 is used for the linear segment of the barrel to design Model 5.

The averaged anchoring strength of the anchorage, the maximum von Mises stress in both the barrel and the wedges, and the maximum strain of the CFRP plate are calculated at a loading of 95% of the tensile strength of the CFRP plate, and the results are shown in Table 4.5.

*Table 4.5: Evaluation Parameters of Models Considered in the Optimization of Linear Segment Slope*

| Model | Averaged CFRP Contact Pressure (MPa) | Barrel Max. Mises Stress (MPa) | Wedge Max. Mises Stress (MPa) | Max. Strain (%) |
|---|---|---|---|---|
| **1** | 193.364 | 2210 | 857 | 1.628 |
| **2** | 211.246 | 1846 | 664 | 1.708 |
| **3** | 181.187 | 1784 | 752 | 1.704 |
| **4** | 200.763 | 1202 | 721 | 1.714 |
| **5** | 180.285 | 985 | 573 | 1.697 |

As can be seen from Table 4.5, Model 5 is the optimal design in terms of minimizing the maximum von Mises stress within the barrel and wedges as well as the maximum strain of the CFRP plate while maintaining a sufficient gripping strength. Model 5 is selected for further optimization as it prevents CFRP plate premature failure and improves the reusability of the wedge anchorage.

### 4.4.2. Optimization of Radius of Circular Segment

The effect of the radius of the circular profile is studied. Different models are designed with a profile radius ranging from 1000 mm to 3000 mm. The length of the circular segment (L1), the length of the linear segment (L2) and the minimum thickness of the barrel (t) are assumed as 50 mm, 20 mm and 11.2 mm respectively. The remaining dimensions of the designed models are summarized in Table 4.6.

*Table 4.6: Dimensions of Models Considered in the Optimization of Radius of Circular Segment*

| Model | r (mm) | W1 (mm) | W2 (mm) | W3 (mm) | $\theta_W$ (Degrees) | B1 (mm) | B2 (mm) | B3 (mm) | $\theta_B$ (Degrees) |
|---|---|---|---|---|---|---|---|---|---|
| **5** | 1500 | 25.55 | 26.77 | 27.59 | 2.35 | 25.5 | 26.33 | 27.16 | 2.35 |
| **6** | 1000 | 25.545 | 27.27 | 28.46 | 3.41 | 25.5 | 26.75 | 27.94 | 3.41 |
| **7** | 1625 | 25.545 | 26.69 | 27.45 | 2.19 | 25.5 | 26.27 | 27.03 | 2.19 |
| **8** | 1750 | 25.545 | 26.62 | 27.33 | 2.05 | 25.5 | 26.21 | 26.93 | 2.05 |
| **9** | 1875 | 25.545 | 26.56 | 27.23 | 1.93 | 25.5 | 26.17 | 26.84 | 1.93 |
| **10** | 2000 | 25.545 | 26.51 | 27.14 | 1.81 | 25.5 | 26.13 | 26.76 | 1.81 |
| **11** | 2250 | 25.545 | 26.42 | 26.99 | 1.64 | 25.5 | 26.06 | 26.63 | 1.64 |
| **12** | 2500 | 25.545 | 26.35 | 26.87 | 1.49 | 25.5 | 26.00 | 26.52 | 1.49 |
| **13** | 2750 | 25.545 | 26.29 | 26.76 | 1.37 | 25.5 | 25.96 | 26.43 | 1.37 |
| **14** | 3000 | 25.545 | 26.24 | 26.68 | 1.27 | 25.5 | 25.92 | 26.36 | 1.27 |

The averaged gripping strength of the anchorage, the maximum von Mises stress in both the barrel and the wedges, and the maximum strain of the CFRP plate are calculated at a loading of 95% of the tensile strength of the CFRP plate, and the results are shown in Table 4.7.

*Table 4.7: Evaluation Parameters of Models Considered in the Optimization of Radius of Circular Segment*

| Model | Averaged CFRP Contact Pressure (MPa) | Barrel Max. Mises Stress (MPa) | Wedge Max. Mises Stress (MPa) | Max. Strain (%) |
|---|---|---|---|---|
| **5** | 193.146 | 1050 | 622 | 1.711 |
| **6** | 252.975 | 1337 | 757 | 1.721 |
| **7** | 176.182 | 978 | 571 | 1.697 |
| **8** | 192.5 | 1045 | 596 | 1.712 |
| **9** | 192.634 | 1048 | 602 | 1.709 |
| **10** | 193.146 | 1050 | 622 | 1.711 |
| **11** | 202.691 | 1091 | 617 | 1.721 |
| **12** | 216.121 | 1173 | 651 | 1.724 |
| **13** | 219.007 | 1185 | 636 | 1.728 |
| **14** | 216.929 | 1172 | 664 | 1.727 |

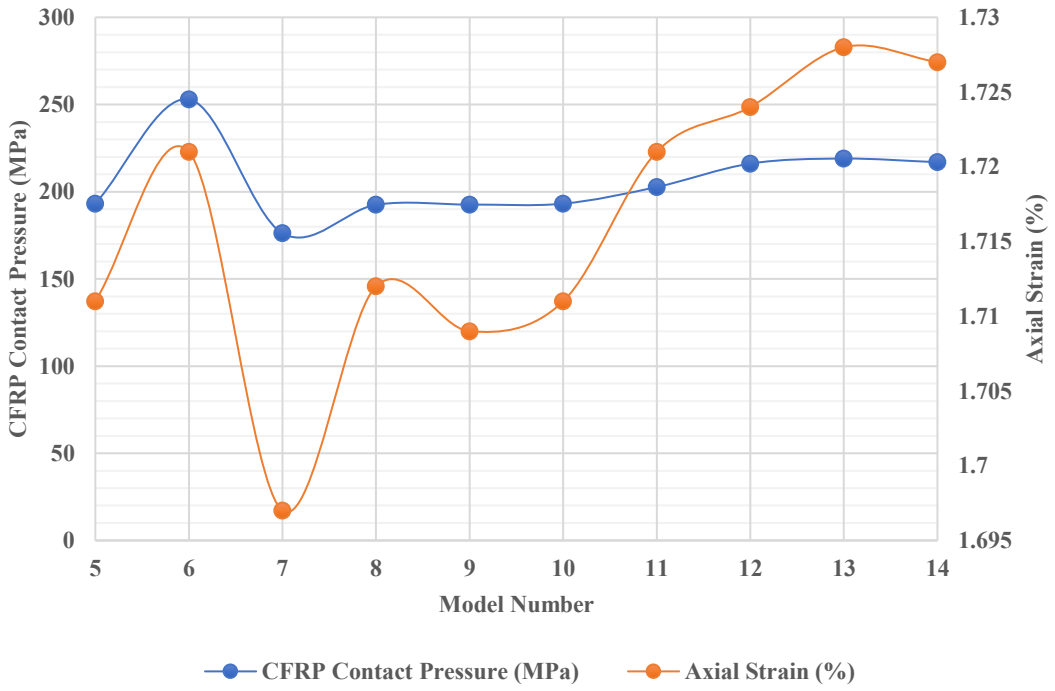


*Figure 4.11: Averaged CFRP Contact Pressure and Maximum Axial Strain for Models Associated with Radius Optimization of Circular Profile*

Since minimizing the maximum axial strain is an important factor to avoid CFRP premature failure, and the averaged CFRP contact pressure is crucial in terms of maintaining a high anchoring strength, the optimal design should minimize the axial strain and maximize the CFRP contact pressure. It is clear from Figure 4.11 that Model 8, Model 9 and Model 10 have almost the same CFRP contact pressure, yet Model 9 and Model 10 have slightly less maximum axial strain than Model 8. However, Model 8 is selected as the optimal model because the wedge slides more into the barrel during the loading process, therefore, guaranteeing higher area of contact between the barrel and the wedges. The area of contact is critical in terms of maintaining the safety of the wedge anchorage as well as shifting the maximum contact pressure to the presetting edge (edge 2) of the CFRP plate. Therefore, Model 8 is chosen for further optimization analysis.

### 4.4.3. Optimization of Lengths of Linear and Circular Segments

The final optimization process focuses on the lengths of the linear and the circular segments. Different designs are studied by shifting the length of the circular segment while fixing the total length of the anchorage. The dimensions of the models considered in this step of the optimization process are listed in Table 4.8 where the circular profile radius (r) and the minimum barrel thickness (t) are 1750 mm and 11.2 mm respectively.

*Table 4.8: Dimensions of Models Considered in Optimization of the Length of Circular Segment*

| Model | L1 (mm) | L2 (mm) | W1 (mm) | W2 (mm) | W3 (mm) | $\theta_W$ (Degrees) | B1 (mm) | B2 (mm) | B3 (mm) | $\theta_B$ (Degrees) |
|---|---|---|---|---|---|---|---|---|---|---|
| **8** | 50 | 70 | 25.55 | 26.62 | 27.33 | 2.05 | 25.5 | 26.21 | 26.93 | 2.05 |
| **15** | 45 | 70 | 25.55 | 26.45 | 27.27 | 1.88 | 25.5 | 26.08 | 26.90 | 1.84 |
| **16** | 55 | 70 | 25.55 | 26.80 | 27.38 | 2.21 | 25.5 | 26.36 | 26.94 | 2.21 |
| **17** | 60 | 70 | 25.55 | 27.00 | 27.42 | 2.38 | 25.5 | 26.53 | 26.94 | 2.38 |

The averaged gripping strength of the anchorage, the maximum von Mises stress in both the barrel and the wedges, and the maximum strain of the CFRP plate are computed at a loading of 95% of the tensile strength of the CFRP plate, and the results are shown in Table 4.9.

*Table 4.9: Evaluation Parameters of Models Considered in the Optimization of the Length of Circular and Linear Segments*

| Model | Averaged CFRP Contact Pressure (MPa) | Barrel Max. Mises Stress (MPa) | Wedge Max. Mises Stress (MPa) | Max. Strain (%) |
|---|---|---|---|---|
| **8** | 192.5 | 1105 | 631 | 1.712 |
| **15** | 190.745 | 997 | 604 | 1.715 |
| **16** | 188.164 | 1093 | 616 | 1.702 |
| **17** | 184.506 | 1110 | 615 | 1.705 |

As shown in Table 4.9, Model 16 is the optimal design mainly because the maximum strain of CFRP plate is minimized so that CFRP premature failure is less likely to occur. It is later shown in Section 4.5 that no CFRP premature failure is expected to happen. Thus, Model 16 is selected to be manufactured and tested.

## 4.5. Results of Finite Element Model

The results of the optimal model, Model 16, including the von Mises stress throughout the barrel and the wedge and the contact pressure across the CFRP plate are recorded after presetting the wedge by 6 mm and applying a tensile loading of 95% of the tensile strength of the CFRP plate. Several FRP failure criteria are tested to study the occurrence of CFRP plate premature failure. The effect of the presetting distance on the von Mises stress within the wedge anchorage as well as the contact pressure on the CFRP plate is investigated.

### 4.5.1. Von Mises Stress Distribution within Barrel

The von Mises stress distribution throughout the barrel is shown in Figure 4.12. As it can be seen from Figure 4.12, designing the linear segments of the barrel and the wedges with the same slope proved to be useful in smoothing the internal stresses within the barrel throughout the linear segment. However, based on Figure 4.13, the maximum von Mises stress occurs at a 55 mm distance from the loading edge (edge 1) of the barrel, which is the point of profile change from circular to linear, then decreases slightly along the linear segment. This is due to the decrease of the barrel thickness along its length as shown in Figure 4.1. The maximum von Mises stress within the barrel is 1,141 MPa which is much lower than its yield strength of 1896 MPa; therefore, plastic deformation can be theoretically avoided within the barrel during both the presetting process as well as the loading process.

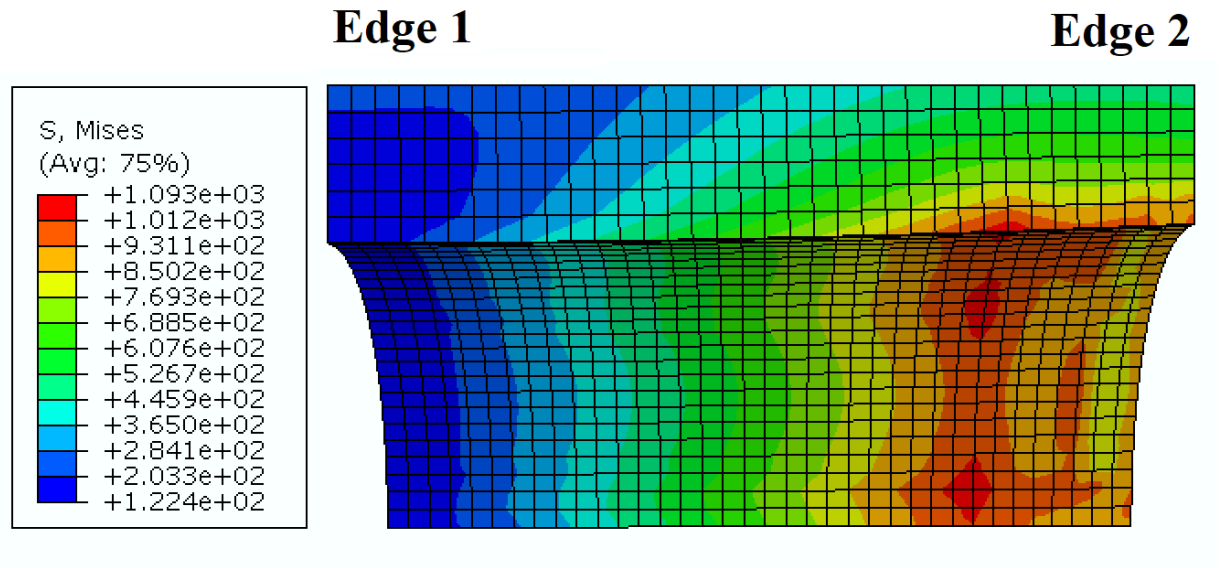


*Figure 4.12: Side View of von Mises Stress Distribution (MPa) Across the Barrel*

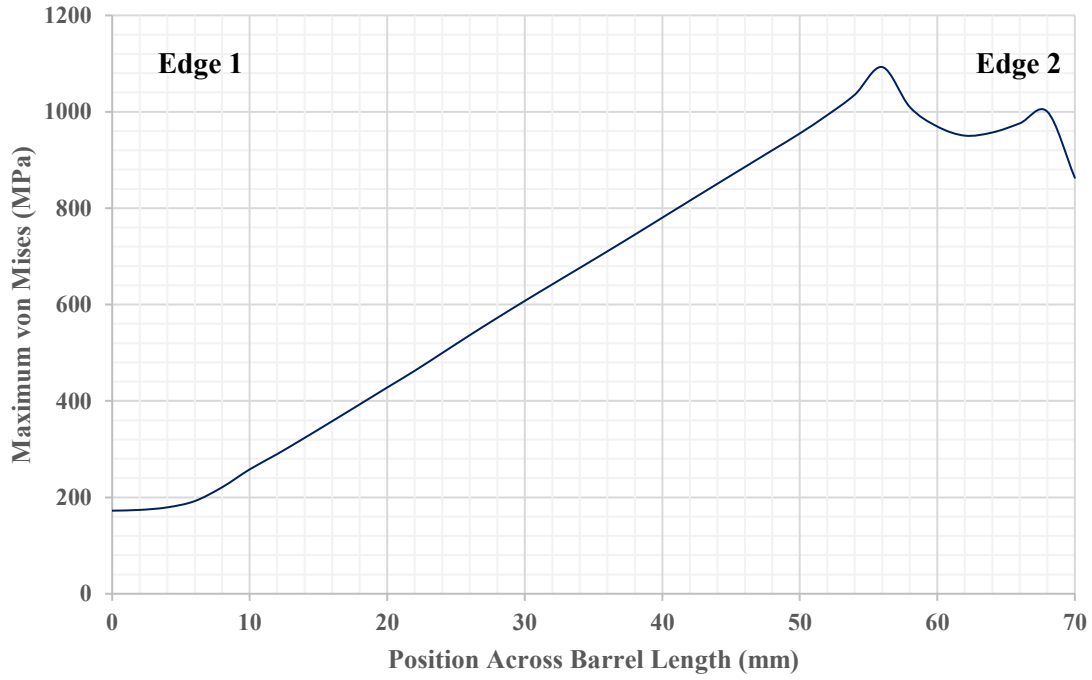


*Figure 4.13: Maximum von Mises Stress Distribution (MPa) Across the Length of the Barrel (mm)*

### 4.5.2. von Mises Stress Distribution within Wedge

The von Mises stress distribution within the wedges is shown in Figure 4.14. The maximum von Mises stress is 640 MPa; thus, no plastic deformation is expected within the wedges. As observed from Figure 4.14, the maximum von Mises stress occurs at the outer surface of the wedge at its contact with the copper plate. This is because of the existence of stress concentration between the wedge and the CFRP plate and the copper sleeve due to the fact that the width of the wedges is increasing along the length while the width of the CFRP plate and the copper sleeve is constant. Because of stress concentration, the stress distribution shown in Figure 4.15 is not as smooth as that shown in Figure 4.13.

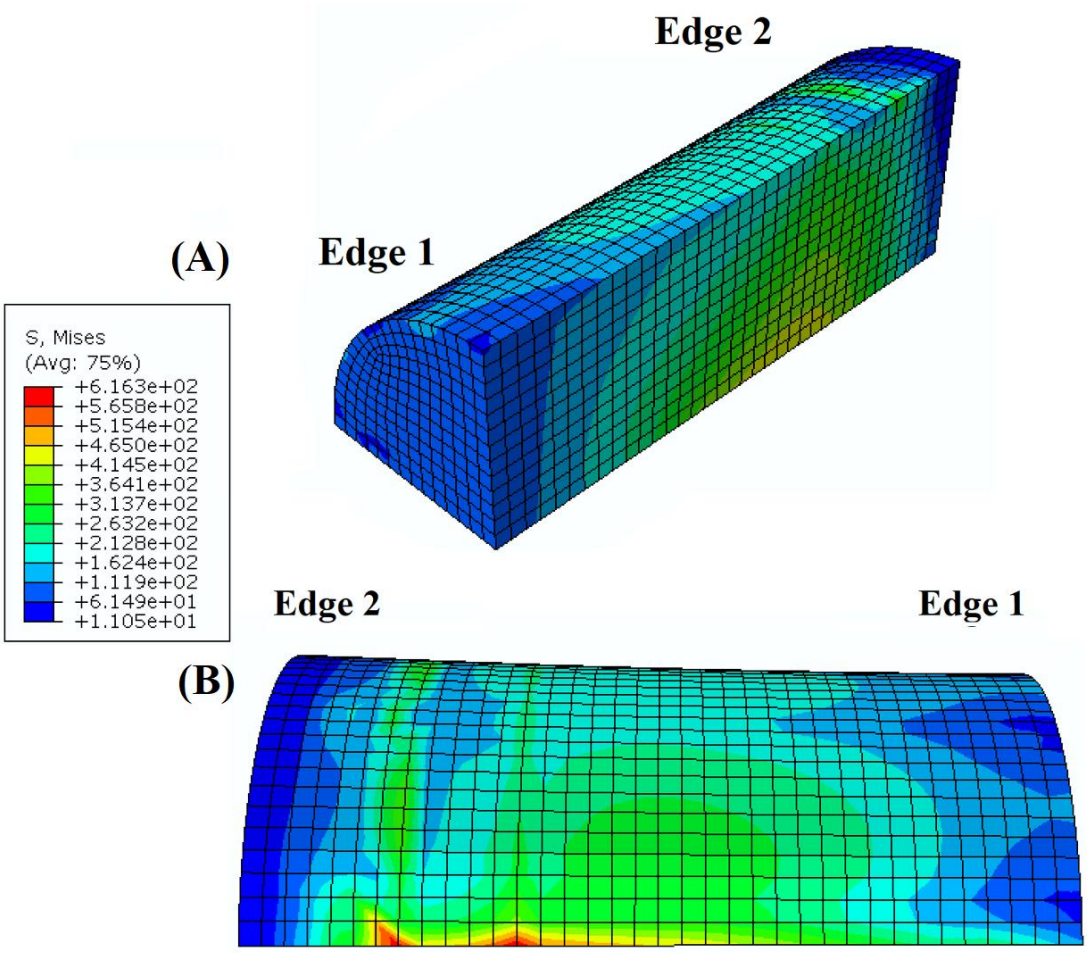


*Figure 4.14: (A) 3D View of von Mises Stress Distribution (MPa) across the Wedge. (B) Side View of von Mises Stress Distribution (MPa) across the Wedge*

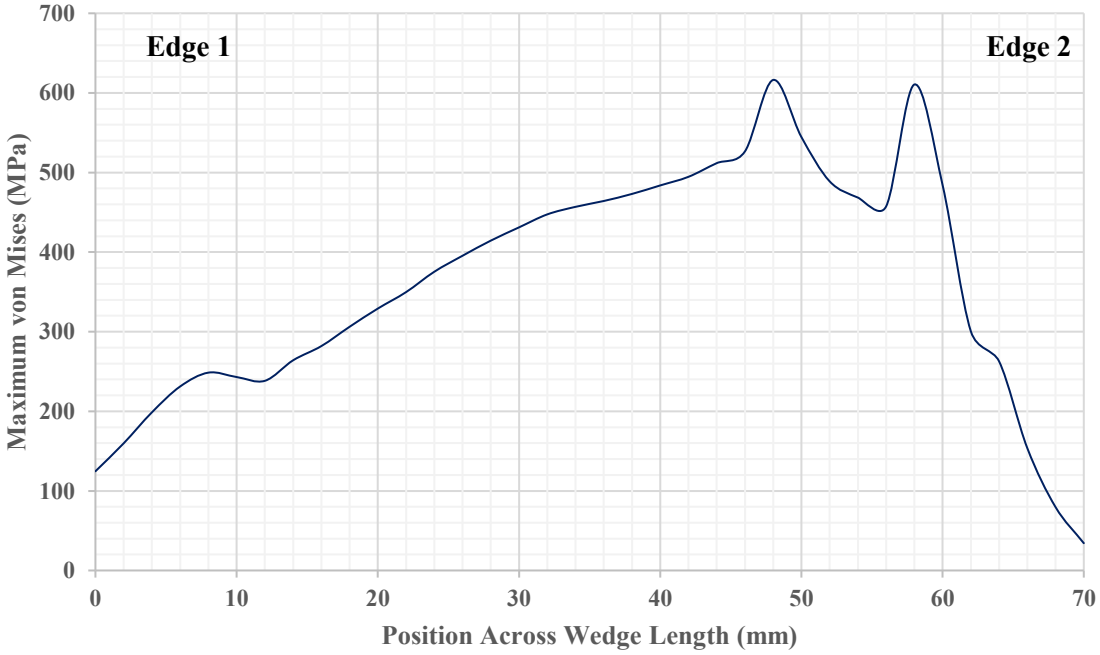


*Figure 4.15: Maximum Von Mises Stress Distribution (MPa) along the Length of the Wedge (mm)*

### 4.5.3. Contact Pressure Distribution across CFRP Plate

The contact pressure distribution throughout the anchored area of the CFRP plate is shown in Figure 4.16 and Figure 4.17. Based on these two figures, the following points can be deduced:

- The loading edge (edge 1) of the CFRP plate has very low contact pressure which is desired to avoid premature failure caused by stress concentration.
- The maximum contact pressure is near the middle section of the CFRP plate. The maximum contact pressure can be shifted toward the presetting edge (edge 2) by increasing the presetting distance.
- Since the wedges are wider than the CFRP plate, stress concentration is created at the sides of the CFRP plate as shown in Figure 4.16.

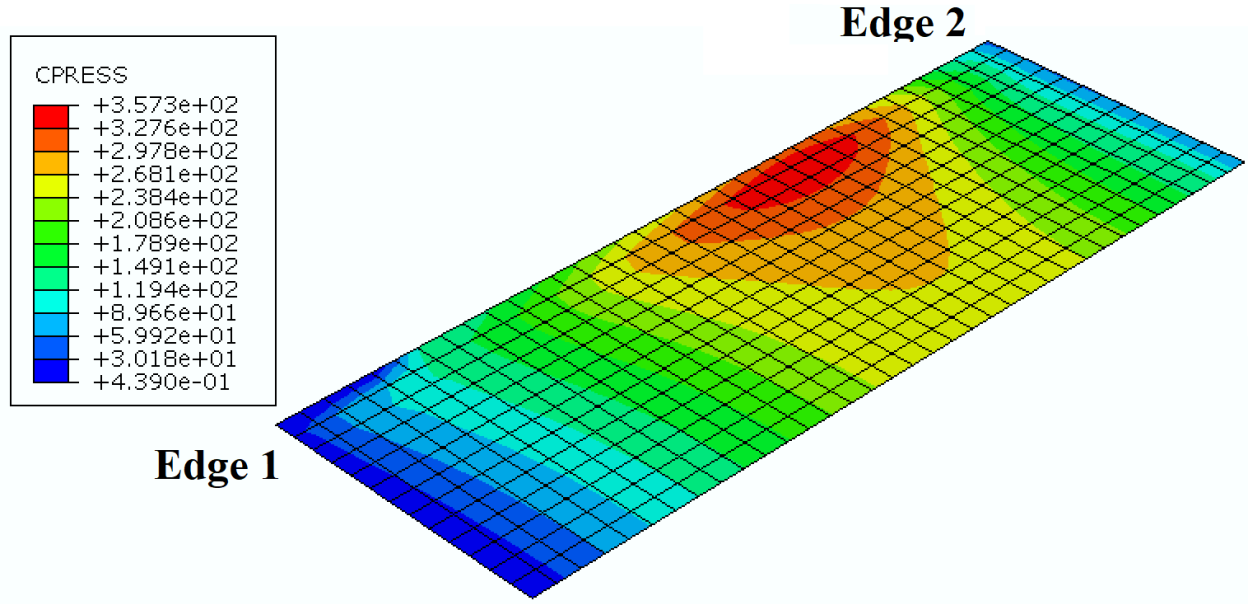


*Figure 4.16: Contact Pressure Distribution (MPa) across the Anchored Length of CFRP Plate*

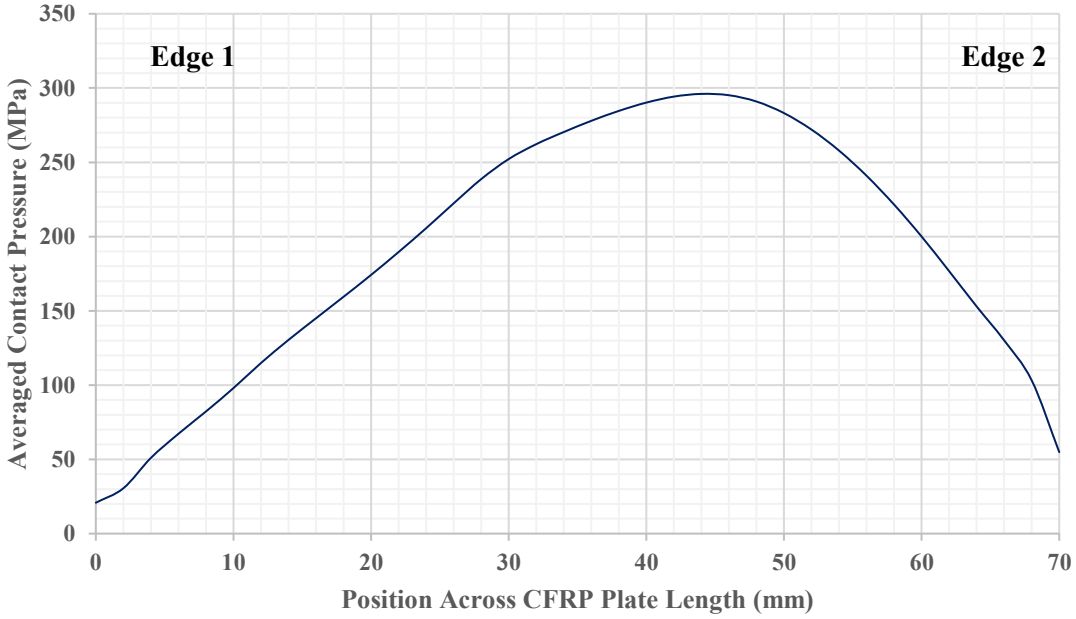


*Figure 4.17: Averaged Contact Pressure Distribution (MPa) across the Anchored Length of CFRP Plate (mm)*

### 4.5.4. Effect of Presetting Distance

The presetting distance is defined as the insertion displacement of the wedges into the barrel during the presetting process. Analysing the effect of the presetting distance is crucial as it can affect the slipping and the contact pressure of the CFRP plate as well as the von Mises stress within the barrel and the wedges. There are two different levels of presetting which are moderate presetting and high presetting. Moderate presetting is preferred in the field as the wedges are hammered into the barrel; however, moderate presetting induces low contact pressure on the CFRP plate, so more CFRP slipping is likely to occur while the anchorage preseat itself during the tensile loading application in a self-seating process. High presetting, on the other hand, requires usage of machinery; therefore, it is harder to perform in the field. High presetting is important to minimize CFRP slipping to very low levels as the CFRP plate is fully anchored even before applying any tensile load. Nevertheless, high presetting will increase the stresses within the barrel and the wedges possibly leading to plastic deformation.

Different presetting distances ranging from 2 mm to 10 mm are simulated to study the effect of the presetting distance and to identify the point of transition from moderate presetting to high presetting. The effect of the presetting distance on the induced contact pressure across the CFRP plate, the von Mises stress within the barrel and the von Mises stress within the wedges is analysed before and after applying the tensile load and the results are illustrated in Figure 4.18 and Figure 4.19, Figure 4.20 and Figure 4.21, and Figure 4.22 and Figure 4.23 respectively.

Based on these figures, the following points can be concluded:

- The moderate presetting distance of up to 7 mm does not affect the contact pressure on the CFRP plate nor the von Mises stress within the barrel and the wedges once the tensile load is applied as can be seen from Figure 4.19, Figure 4.21 and Figure 4.22.
- Operating within the range of moderate presetting distance is generally safer and more recommended since the stresses within the anchorage are minimized; however, since the contact pressure on the CFRP plate is reduced as well then CFRP slipping is more likely to occur as the presetting distance is decreased.
- A presetting distance of 7mm is the transition point from moderate presetting to high presetting as the magnitudes of the CFRP contact pressure and the von Mises stress within the barrel and the wedges are not changing during the loading process which is a sign of high presetting. However, the induced CFRP contact pressure and von Mises stress within the barrel and the wedges are the same as those produced after loading moderately presetted anchorages. Thus, it is concluded that a presetting distance of 7mm is the neutral transition point between moderate presetting and high presetting.
- The high presetting distance, ranging from 7mm and more, can significantly increase the CFRP contact pressure and the stresses within the barrel and the wedges; therefore, the occurrence of plastic deformation within the wedge anchorage is more likely. While high presetting is not generally desired due to the need of machinery usage, it is quite useful for diminishing CFRP slipping.

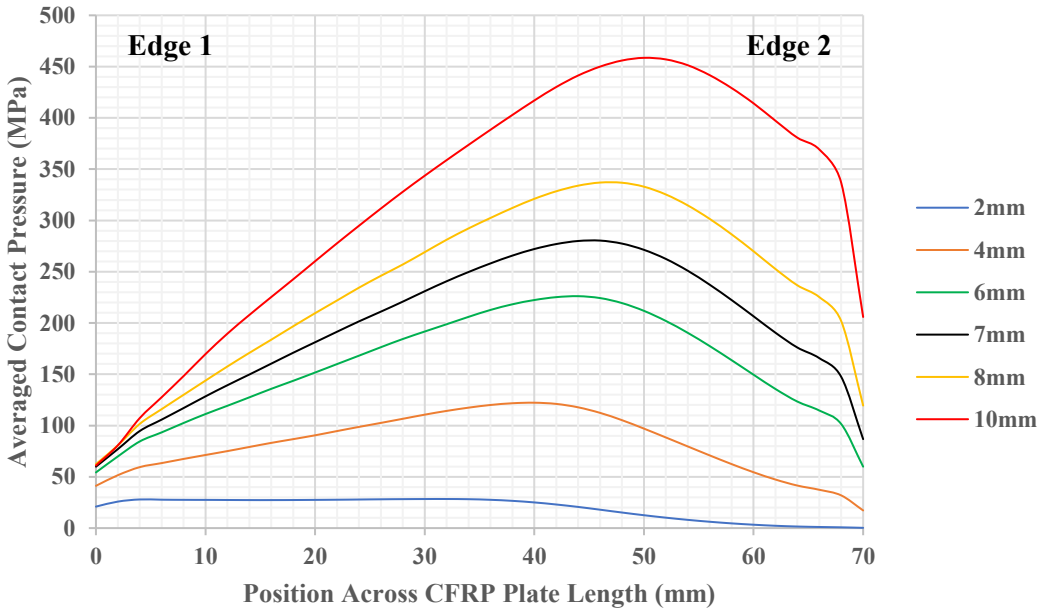


*Figure 4.18: Averaged CFRP Contact Pressure (MPa) before Applying Tensile Load at Different Presetting Distances (mm)*

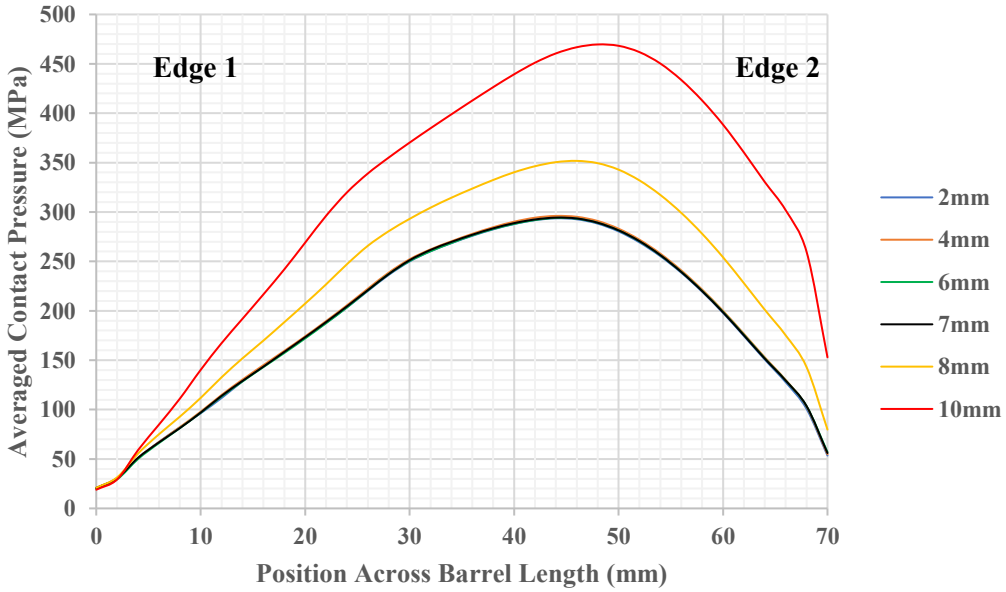


*Figure 4.19: Averaged CFRP Contact Pressure (MPa) after Applying Tensile Load at Different Presetting Distances (mm)*

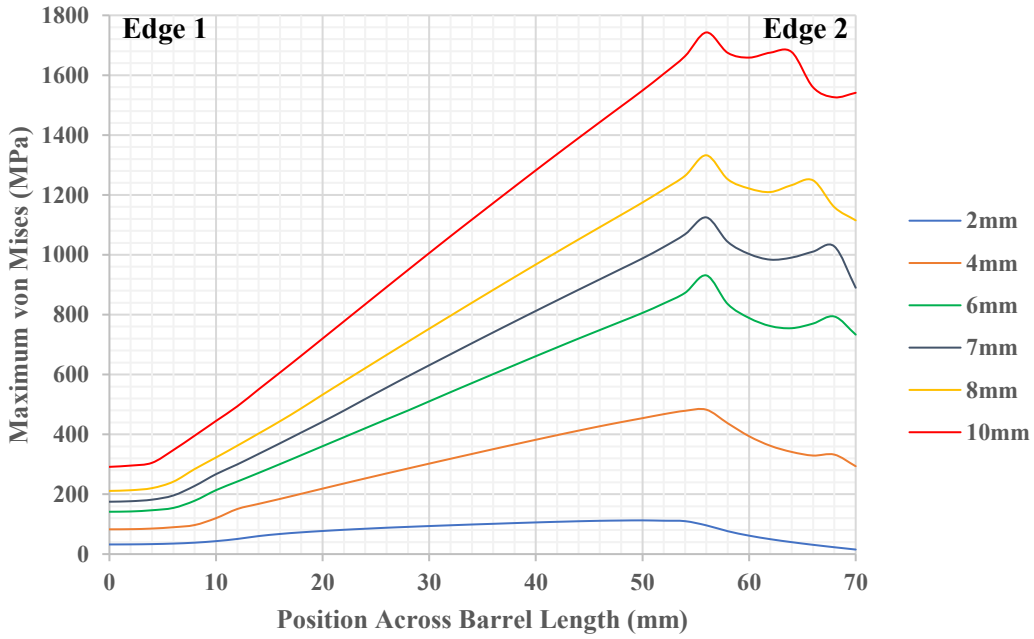


*Figure 4.20: Maximum von Mises Stress (MPa) within the Barrel before Applying Tensile Load at Different Presetting Distances*


*Figure 4.21: Maximum von Mises Stress (MPa) within the Barrel after Applying Tensile Load at Different Presetting Distances*

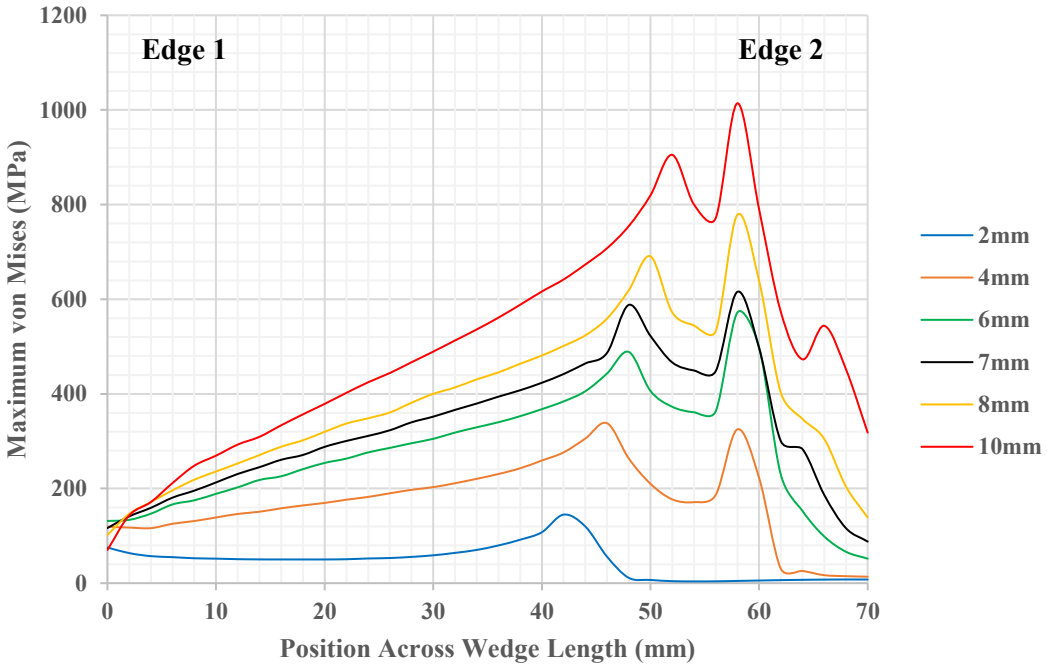


*Figure 4.22: Maximum von Mises Stress (MPa) within the Wedge before Applying Tensile Load at Different Presetting Distances*

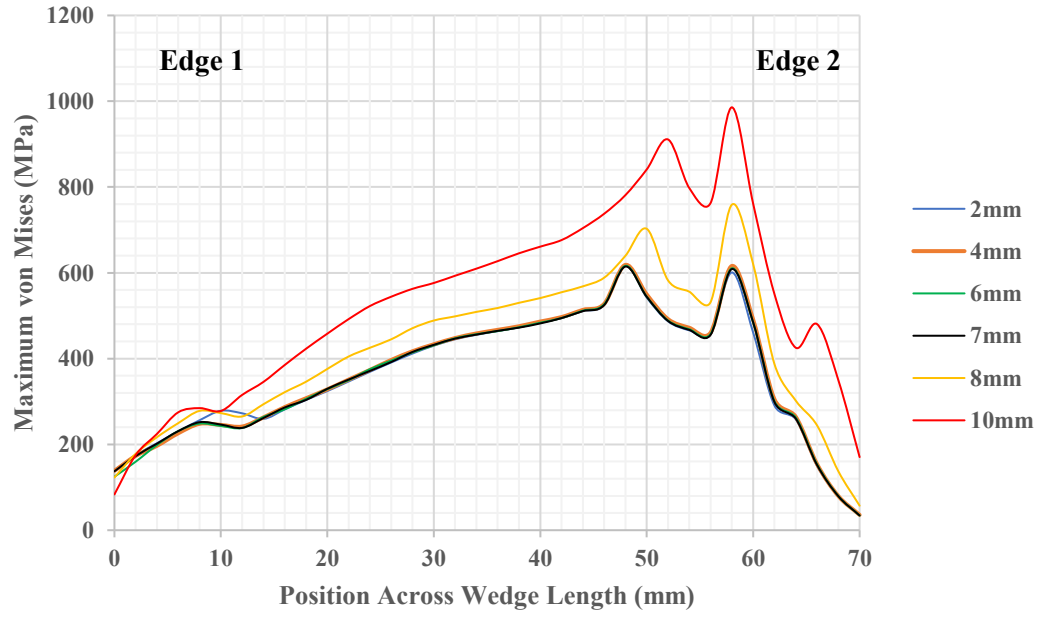


*Figure 4.23: Maximum von Mises Stress (MPa) within the Wedge after Applying Tensile Load at Different Presetting Distances*

### 4.5.5. CFRP Plate Failure Analysis

Several composite failure criteria are tested to confirm that CFRP premature failure is unlikely to occur. The examined failure criteria are maximum stress theory, maximum strain theory, Tsai-Hill theory, and Hashin's theory. The axial strength, the transverse strength and the shear strength as well as the ultimate tensile strain of the CFRP plate previously shown in Section 4.2.2 are listed in Table 4.10. The computed averaged axial stress, transverse stress and shear stress along the width of the CFRP plate after moderately presetting the wedges and applying 95% of the total tensile loading are listed in Table 4.11 and used in the following subsections to investigate the likelihood of the CFRP plate premature failure.

*Table 4.10: Axial, Transverse and Shear Strengths of CFRP Plate*

| Property | Magnitude |
|---|---|
| **Axial Tensile Strength ($S_{ten-A}$)** | 2800 MPa |
| **Axial Compressive Strength ($S_{com-A}$)** | 1155 MPa |
| **Transverse Tensile Strength ($S_{ten-T}$)** | 62 MPa |
| **Transverse Compressive Strength ($S_{com-T}$)** | 350 MPa |
| **In-Plane Shear Strength ($S_{sh}$)** | 100 MPa |
| **Ultimate Axial Tensile Strain ($\varepsilon_{ult}$)** | 1.7% |

*Table 4.11: Averaged Axial, Transverse, and In-Plane Shear Stresses Along the Width of the CFRP Plate at 95% of Tensile Loading*

| Distance from Loading Edge (Edge 1) (mm) | $\sigma_{11}$ (MPa) | $\sigma_{22}$ (MPa) | $\tau_{12}$ (MPa) | $\tau_{13}$ (MPa) |
|---|---|---|---|---|
| **0** | 2656.87 | -6.97 | 0.73 | 1.46 |
| **2** | 2651.19 | -25.64 | 5.61 | 1.86 |
| **4** | 2609.24 | -45.64 | 11.23 | 2.32 |
| **6** | 2532.32 | -63.62 | 16.20 | 3.02 |
| **8** | 2433.38 | -80.64 | 20.77 | 3.58 |
| **10** | 2310.74 | -95.85 | 24.80 | 3.53 |
| **12** | 2166.20 | -108.24 | 27.93 | 2.94 |
| **14** | 2005.03 | -118.54 | 30.19 | 2.09 |
| **16** | 1825.23 | -129.31 | 32.03 | 1.64 |
| **18** | 1631.31 | -142.89 | 34.46 | 1.52 |
| **20** | 1423.98 | -157.85 | 37.47 | 0.74 |
| **22** | 1190.53 | -172.30 | 40.29 | 1.04 |
| **24** | 940.10 | -186.28 | 41.43 | 2.19 |
| **26** | 672.01 | -201.14 | 42.83 | 2.00 |
| **28** | 401.41 | -216.25 | 36.81 | 1.47 |
| **30** | 229.16 | -228.41 | 16.39 | 1.10 |
| **32** | 162.06 | -236.68 | 8.31 | 0.97 |
| **34** | 130.85 | -242.91 | 3.10 | 0.56 |
| **36** | 117.06 | -248.93 | 2.26 | 0.71 |
| **38** | 105.63 | -254.99 | 1.59 | 0.56 |
| **40** | 99.14 | -260.12 | 0.57 | 0.37 |
| **42** | 102.50 | -263.31 | 1.16 | 1.14 |
| **44** | 106.65 | -264.33 | 0.44 | 3.05 |
| **46** | 107.57 | -263.27 | 0.80 | 4.26 |
| **48** | 110.62 | -259.60 | 0.46 | 5.29 |
| **50** | 106.06 | -252.64 | 1.44 | 6.10 |
| **52** | 104.84 | -242.22 | 0.75 | 6.76 |
| **54** | 101.48 | -228.81 | 2.37 | 7.51 |
| **56** | 88.15 | -213.04 | 1.90 | 7.86 |
| **58** | 87.25 | -195.22 | 0.34 | 8.74 |
| **60** | 90.04 | -175.92 | 1.71 | 12.88 |
| **62** | 79.61 | -154.93 | 2.99 | 11.35 |
| **64** | 61.38 | -133.14 | 3.37 | 18.27 |
| **66** | 45.60 | -112.93 | 3.80 | 15.96 |
| **68** | 31.72 | -90.08 | 5.70 | 21.26 |
| **70** | 14.31 | -51.55 | 2.95 | 16.09 |

#### 4.5.5.1. Tsai-Hill Theory

Tsai-Hill theory, which is based on von Mises yield criterion, predicts that failure within CFRP plate will occur once the condition shown in equation **(4.1)** is met [71]. The axial stress, the transverse stress, and the shear stress listed in Table 4.11 are substituted into the equation, and the results of Tsai-Hill equation are shown in Figure 4.24. The maximum value obtained through equation **(4.1)** is 0.91 as shown in Figure 4.24; therefore, according to Tsai-Hill theory, CFRP premature failure is unlikely to occur.

$$\frac{{\sigma_1}^2}{{S_{ten-A}}^2} + \frac{{\sigma_2}^2}{{S_{com-T}}^2} + \frac{{\tau_{12}}^2}{{S_{sh}}^2} - \frac{\sigma_1\sigma_2}{{S_{ten-A}}^2} = \begin{cases} \geq 1 & Failure \\ < 1 & No\ Failure \end{cases} \quad (4.1)$$

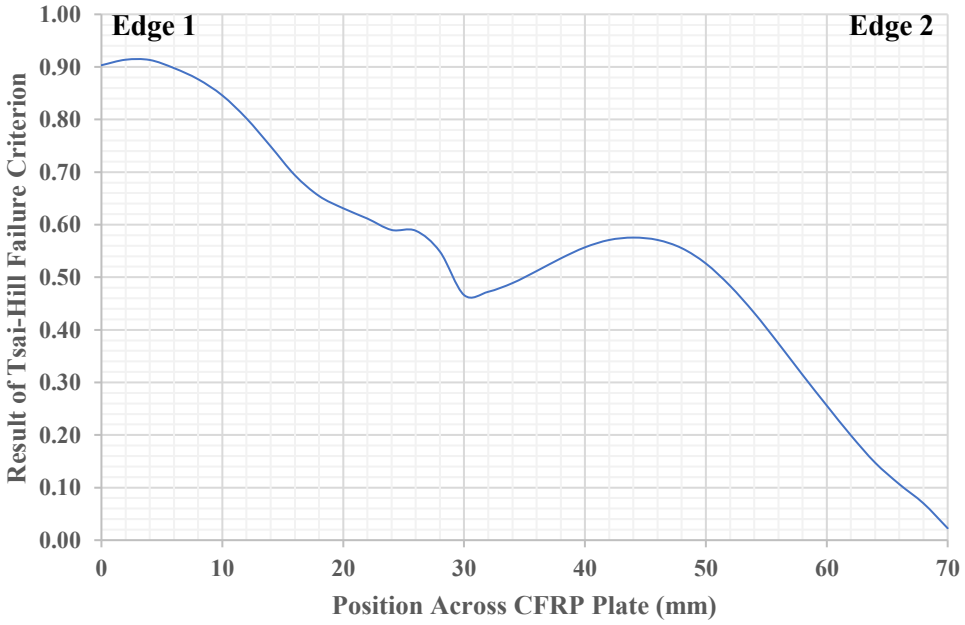


*Figure 4.24: Results of Tsai-Hill Failure Criteria*

### 4.5.5.2. Tsai-Wu Theory

Tsai-Wu theory is used to investigate the likelihood of CFRP premature failure. Based on this theory, failure will occur when the equivalent shown in equation **(4.2)** exceeds a value of 1 [72]. The axial stress, the transverse stress, and the shear stress listed in Table 4.11 are substituted into the equation, and the results are shown in Figure 4.25. As illustrated in Figure 4.25, the maximum value computed from equation **(4.2)** is 0.81; thus, based on the Tsai-Wu failure criterion, premature failure is improbable.

$$f_1\sigma_1 + f_{11}\sigma_1^2 + f_2\sigma_2 + f_{22}\sigma_2^2 + 2f_{12}\sigma_1\sigma_2 + f_{66}\tau_{12}^2 = \begin{cases} \geq 1 & Failure \\ < 1 & No\ Failure \end{cases} \quad (4.2)$$

Where

$$f_1 = \frac{1}{S_{ten-A}} - \frac{1}{S_{com-A}} \qquad f_{11} = \frac{1}{S_{ten-A}S_{com-A}} \qquad f_2 = \frac{1}{S_{ten-T}} - \frac{1}{S_{com-T}}$$

$$f_{22} = \frac{1}{S_{ten-T}S_{com-T}} \qquad f_{12} = \frac{-1}{2}\sqrt{f_{11}f_{22}} \qquad f_{66} = \frac{1}{S_{Sh}^2}$$

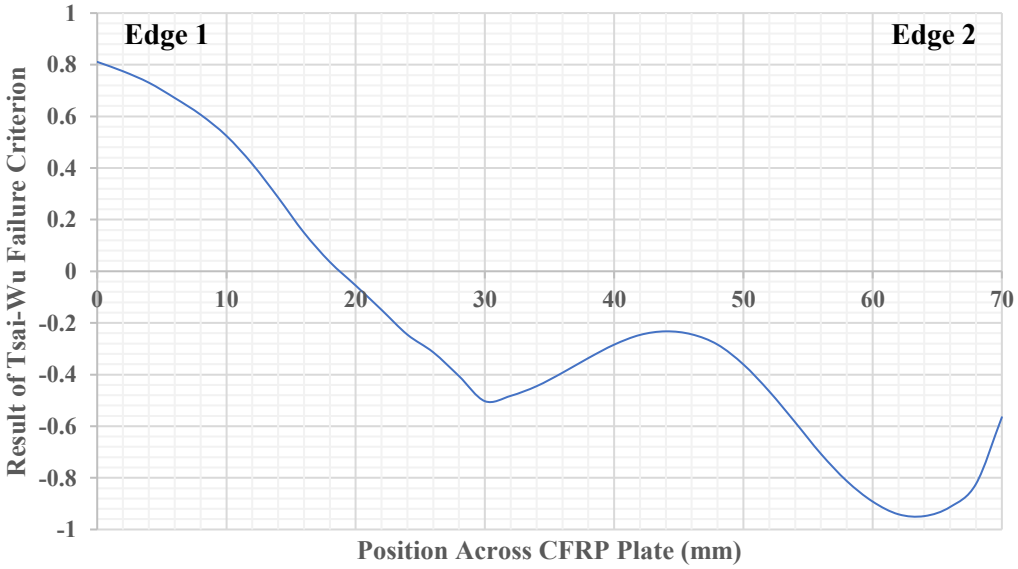


*Figure 4.25: Results of Tsai-Wu Failure Criterion*

#### 4.5.5.3. Hashin Theory

Tensile fiber failure criteria of Hashin theory is applied to predict premature tensile failure within the CFRP plate. Based on this theory, failure will occur when the condition shown in equation **(4.3)** is encountered [72]. The axial stress, the transverse stress, and the shear stress listed in Table 4.11 are substituted into the equation, and the results are shown in Figure 4.26. As shown in Figure 4.26, the maximum value computed from equation **(4.3)** is 0.9; thus, based on the tensile fiber failure criterion, premature failure is improbable.

$$\left(\frac{\sigma_{11}}{S_{ten-A}}\right)^2 + \frac{{\tau_{12}}^2 + {\tau_{13}}^2}{{S_{sh}}^2} = \begin{cases} \geq 1 & Failure \\ < 1 & No\ Failure \end{cases} \tag{4.3}$$

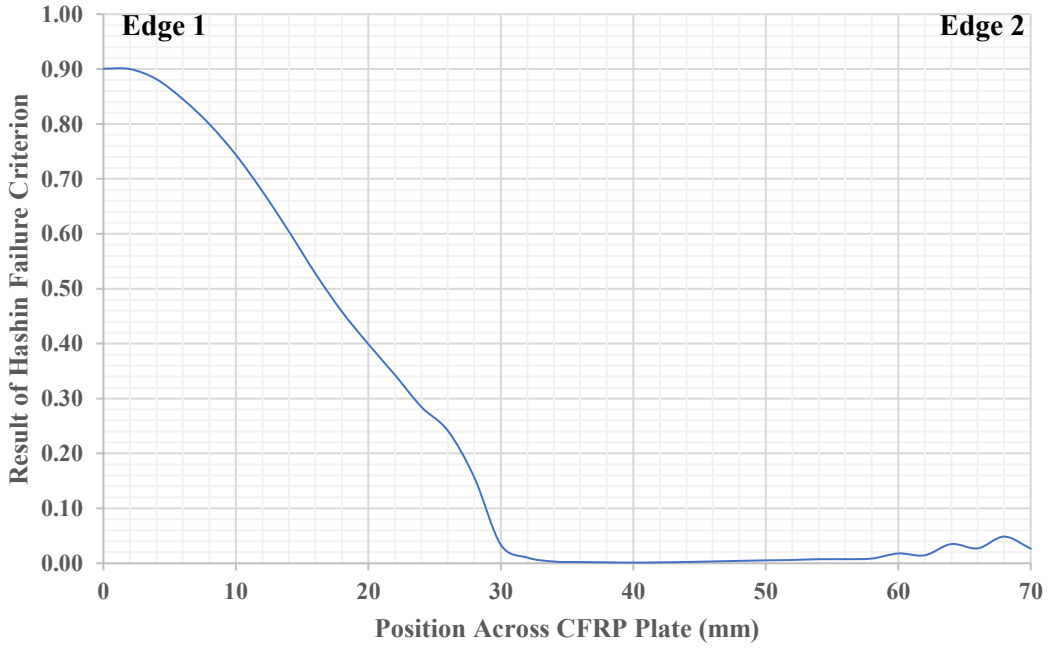


*Figure 4.26: Results of Hashin Failure Criterion*

#### 4.5.5.4. Hoffman Theory

Hoffman theory is used to investigate the likelihood of CFRP premature failure. Based on this theory, failure will occur when the equivalent shown in equation **(4.4)** exceeds a value of 1 [72]. The axial stress, the transverse stress, and the shear stress listed in Table 4.11 are substituted into the equation, and the results are shown in Figure 4.27. As illustrated in Figure 4.27, the maximum value computed from equation **(4.4)** is 0.75; thus, based on the Hoffman failure criterion, premature failure is not expected.

$$\frac{\sigma_1^2}{S_{ten-A}\,S_{Com-A}} - \frac{\sigma_1\sigma_2}{S_{ten-A}\,S_{Com-A}} + \frac{\sigma_2^2}{S_{ten-T}\,S_{Com-T}} - \frac{(S_{ten-A}-S_{Com-A})}{S_{ten-A}\,S_{Com-A}}\sigma_1 - \frac{(S_{ten-T}-S_{Com-T})}{S_{ten-T}\,S_{Com-T}}\sigma_2 + \left(\frac{\tau_{12}}{S_{Sh}}\right)^2 = \begin{cases} \geq 1 & Failure \\ < 1 & No\ Failure \end{cases} \tag{4.4}$$

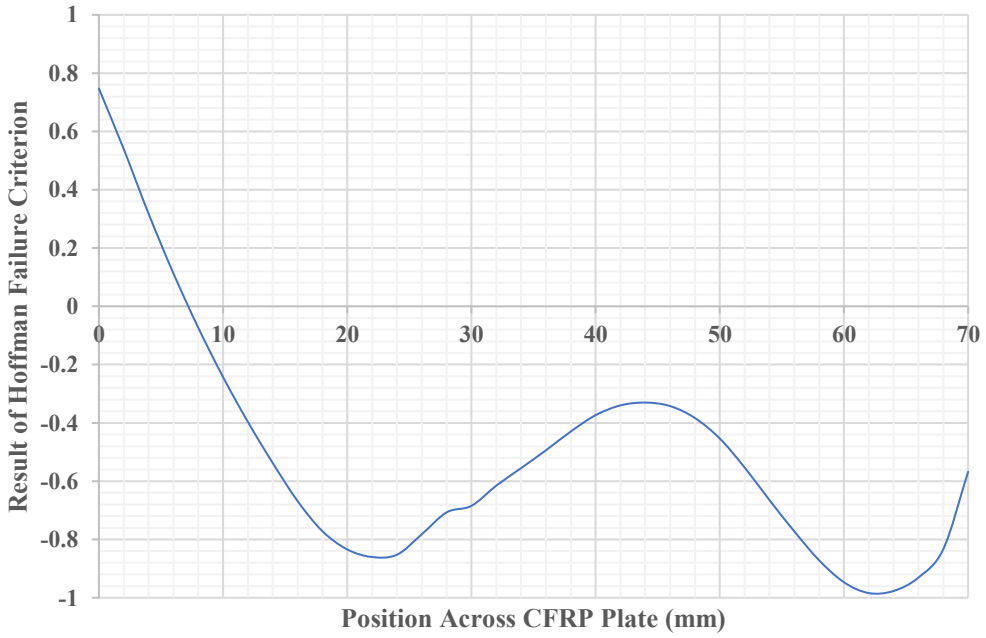


*Figure 4.27: Results of Hoffman Failure Criterion*

## 4.6. Summary

In this chapter, a finite element model of the wedge anchorage system is developed in accordance to the modelling parameters approved by published academic papers. The performed convergence analysis confirmed the convergence of the FEM model where the computed optimal mesh size is 2 mm. The FEM model is then optimized by investigating the effects of the slope of the linear segments, the radius of the circular profile and the lengths of the circular and linear segments on the CFRP contact pressure and the von Mises stress within the barrel and the wedge. The optimization process revealed that Model 16 is the optimal design in terms of reducing the von Mises stress within the barrel and the wedge and minimizing the axial strain of the CFRP plate to prevent CFRP premature failure while maintaining a high anchoring strength of the wedge anchorage. The effect of the presetting distance of the wedges into the barrel on the CFRP contact pressure and the von Mises stress within the barrel and the wedge is then examined. It can be concluded that the range of moderate presetting is up to 7 mm which is taken into consideration in the experimental testing introduced in Chapter 6. CFRP failure analysis is performed by applying various FRP failure theories. All the failure theories confirmed that the occurrence of the CFRP premature failure is unlikely.

# 5

# Analytical Modelling

## 5.1. Introduction

In order to verify the accuracy of the results obtained from the FEM model, an analytical model has been developed. This chapter presents the development of two new analytical models for wedge anchorages used to anchor FRP plates. The chapter starts by introducing the parameters considered and the challenges encountered in the analytical modelling. The assumptions and steps followed in creating each analytical model are discussed in detail. The interference equations are then derived, and the results of the two analytical models are compared to that of the FEM model.

## 5.2. Challenges of Analytical Modelling

Creating an analytical model of the wedge anchorage utilized to grip FRP plates is challenging due to the following reasons.

- The FRP plate and the sleeves create discontinuity of the circular cross-section of the two wedges; as a result, a non-uniform deformation of the wedges and the barrel is expected. Therefore, “thick-walled cylinder” assumption cannot be used directly.
- While the width of the FRP plate and the sleeves is constant, the diameter of the wedges is increasing along the anchorage; thus, stress concentration is anticipated at the edges of the FRP plate and the wedges as discussed in Chapter 4.

## 5.3. Interference Equations

The first step in creating the analytical model is computing the interference between each wedge and the barrel; therefore, the profile equations of the outer surface of each wedge and the inner surface of the barrel must be derived.

### 5.3.1. Parameters of Interference Equations

The parameters considered in deriving the interference equations are defined in Table 5..

*Table 5.1: Parameters of Interference Equations*

| Parameter | Definition |
|---|---|
| $X_1$ | Axial coordinate of the loading edge (edge 1) of the wedges and the barrel which is used as a reference point and given a value of zero. |
| $X_2$ | Axial coordinate of the profile change from circular to linear for the wedges and the barrel. It is equivalent to the length of the circular segment of the anchorage. |
| $X_3$ | Axial coordinate of the presetting edge (edge 2) of the wedges and the barrel. It is equivalent to the length of the anchorage. |
| $X_o$ | Shift of the center of the circular profile of the wedges along the x-axis. |
| $Y$ | Vertical component of the profile radius of the wedges and the barrel. |
| $x_{extra}$ | Extra length of the wedges and the barrel that is not being used after the loading process. |
| $\delta_{int}$ | Initial non-corrected interference. |
| $r$ | Radius of the circular profile of the wedges and the barrel. |
| $r_1$ | Total radius of half-thickness FRP plate, one sleeve and one wedge combined. |
| $r_2$ | Barrel inner radius. |
| $r_3$ | Barrel outer radius. |
| $r_{initial-barrel}$ | Initial inner radius of the barrel at the loading edge (edge 1). |
| $m_1$ | Slope of the linear profile of the wedge. |
| $m_2$ | Slope of the linear profile of the barrel. |

### 5.3.2. Inner Surface Profile of Barrel

The profile of the inner surface of the barrel is constructed from two parts which are a circular profile and a linear profile as shown in Figure 5.1. For the circular profile section of the barrel ($X_1 \leq X \leq X_2$), the profile radius ($r$) is given by $r = \sqrt{X^2 + Y^2}$ which is rewritten as $Y = \sqrt{r^2 - X^2}$. Therefore, the inner radius of the barrel ($r_2$) can be written as shown in equation **(5.1)**. As for the linear profile ( $X_2 \leq X \leq X_3$), the inner radius of the barrel in the linear segment is a simple equation of a straight line given by equation **(5.2).**

$$r_2 = r_{initial-barrel} + r - Y$$

$$r_2 = r_{initial-barrel} + r - \sqrt{(r)^2 - (X)^2} \tag{5.1}$$

$$r_2 = r_{initial-barrel} + r - \sqrt{(r)^2 - (X_2)^2} + m_2(X - X_2) \tag{5.2}$$

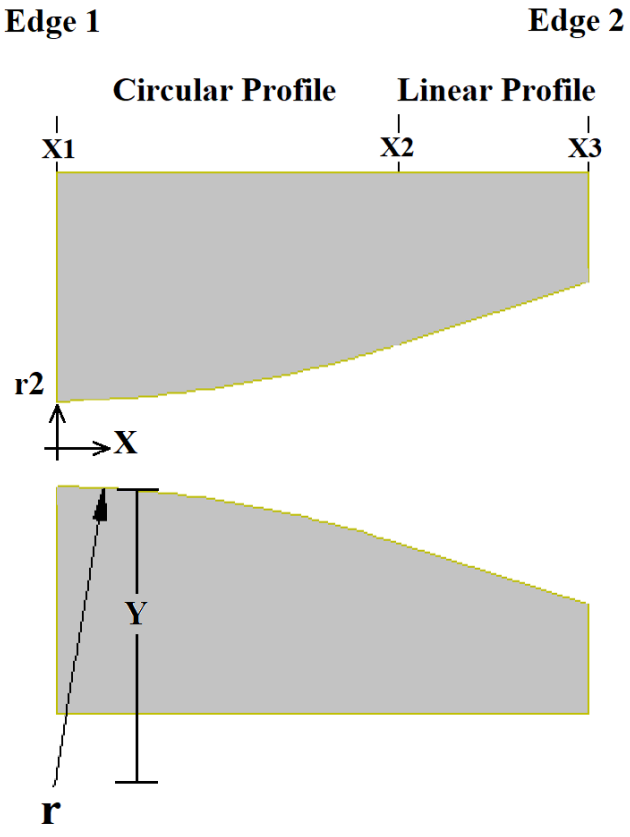


*Figure 5.1: Inner Profile of Barrel*

### 5.3.3. Outer Surface Profile of Wedge

Similar to the inner surface of the barrel, the outer surface profile of the wedge is constructed from a circular profile and a linear profile as shown in Figure 5.2. The equation of the circular profile of the wedges ($X_1 \leq X \leq X_2$) is based on the fact that the center of the circular profile of the wedges is shifted by $X_o$ along the x-axis. Hence, the profile radius ($r$) is given by $r = \sqrt{(X + X_o)^2 + Y^2}$ which can be rewritten as $Y = \sqrt{r^2 - (X + X_o)^2}$. Therefore, the radius of each wedge ($r_1$) is given by equation **(5.3)**.

$$r_1 = r_{initial-barrel} + r - Y$$

$$r_1 = r_{initial-barrel} + r - \sqrt{(r)^2 - (X + X_o)^2} \tag{5.3}$$

As for the linear segment of the wedges ($X_2 \leq X \leq X_3$), the radius of each wedge in the linear segment is a simple equation of a straight line given by equation **(5.4)**.

$$r_1 = r_{initial-barrel} + r - \sqrt{(r)^2 - (X_2 + X_o)^2} + m_1(X - X_2) \tag{5.4}$$

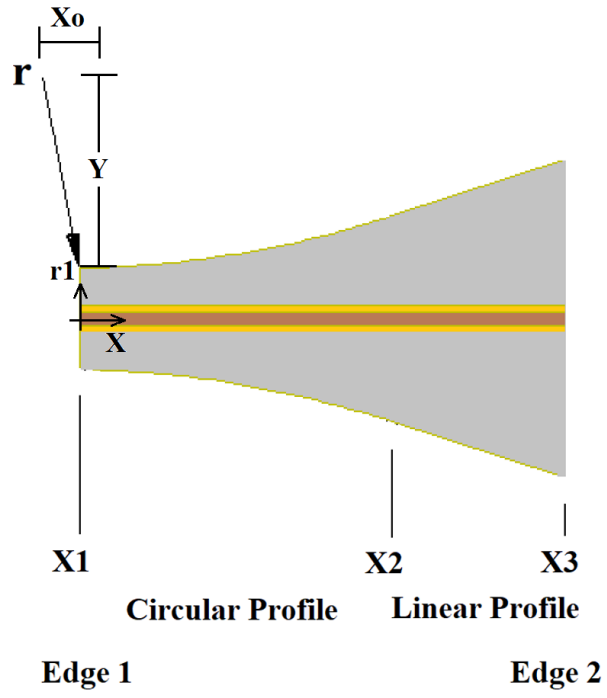


*Figure 5.2: Outer Profile of Wedge*

### 5.3.4. Interference between wedge and barrel

The interference between the wedges and the barrel can be calculated simply by subtracting the radius of the wedge by the inner radius of the barrel; however, some minor changes need to be done on the profile equations in case of incomplete insertion of the wedges into the barrel. If the wedges are inserted partially into the barrel then there is an extra length $x_{extra}$ of the wedges and the barrel that is not being used. It is possible to divide the interference across the length of the anchorage into 3 different segments which are circular profile interference, circular-linear profile interference, and linear profile interference.

The circular profile interference ($0 \leq X \leq X_2 - X_{extra}$) is defined as the interference between the circular segments of the barrel and the wedges. The circular profile equation of the barrel **(5.1)** is modified by including $X_{extra}$ to obtain equation **(5.5)** which takes into account the effect of partial insertion of the wedges. The circular profile equation of the wedge is given by equation **(5.3)**. Therefore, the interference equation of the circular profile region is calculated by equation **(5.7)**.

$$r_2 = r_{initial-barrel} + r - \sqrt{(r)^2 - (X + X_{extra})^2} \tag{5.5}$$

$$Interference = \delta_{int} = r_1 - r_2 \tag{5.6}$$

$$\delta_{int} = \sqrt{(r)^2 - (X + X_{extra})^2} - \sqrt{(r)^2 - (X + X_o)^2} \tag{5.7}$$

The circular-linear profile interference ($X_2 - X_{extra} \leq X \leq X_2$) is defined as the interference between the circular segment of the wedges and the linear segment of the barrel. The circular profile equation of the wedge is given by equation **(5.3)**. $X_{extra}$ is included in equation **(5.2)** to find the linear profile equation of the barrel in case of partial insertion of wedges which is given by equation **(5.8)**. Therefore, the interference is estimated by equation **(5.9)**.

$$r_1 = r_{initial-barrel} + r - \sqrt{(r)^2 - (X_2 + x_{extra})^2} + m_2(X - (X_2 + x_{extra})) \tag{5.8}$$

$$\delta_{int} = \sqrt{(r)^2 - (X_2 + x_{extra})^2} - \sqrt{(r)^2 - (X + X_o)^2} - m_2(X - (X_2 + x_{extra})) \tag{5.9}$$

The linear profile interference ($X_2 \leq X \leq X_3 - x_{extra}$) is defined as the interference between the linear segments of the wedges and the barrel. The linear profile equation of the wedges and the barrel are given by equations **(5.4)** and **(5.8)** respectively. Therefore, the interference is calculated by equation **(5.10)**

$$\delta_{int} = \sqrt{(r)^2 - (X_2 + x_{extra})^2} - \sqrt{(r)^2 - (X_2 + X_o)^2} + m_1(X - X_2) - m_2(X - (X_2 + x_{extra})) \tag{5.10}$$

## 5.4. Analytical Model 1

### 5.4.1. Assumptions and Methodology of Model 1

Model 1 is an iterative analytical model that is based primarily on the thick-walled cylinder assumption. Its iterative nature stems from the fact that the FRP plate and the sleeves are initially assumed to be part of the wedges in the 1st step in order to simplify the calculation of the initial interference between the wedge and the barrel. The thick-walled cylinder assumption is then applied to calculate the initial contact pressure on the FRP plate and the sleeve. Although the initial contact pressure obtained in the 1st step is somewhat inaccurate, it can still be used to calculate the transverse deformation of the half-thickness FRP plate and the sleeve caused by the initial contact pressure calculated in the 1st step.

The transverse deformation is then used in the 2nd step to modify the interference equations to take into account the deformation of the half-thickness FRP plate and the sleeve during the press-fitting process. The corrected contact pressure is then calculated by applying the thick-walled cylinder assumption on the modified interference equations. The accuracy can then be enhanced by utilizing the iterative ability of model 1. Note that a small number of iterations will be required to optimize the accuracy of the model due to the fact that the thicknesses of the FRP plate and the sleeves are relatively very small compared to the wedges. The methodology of model 1 is summarized in the flowchart shown in Figure 5.3.

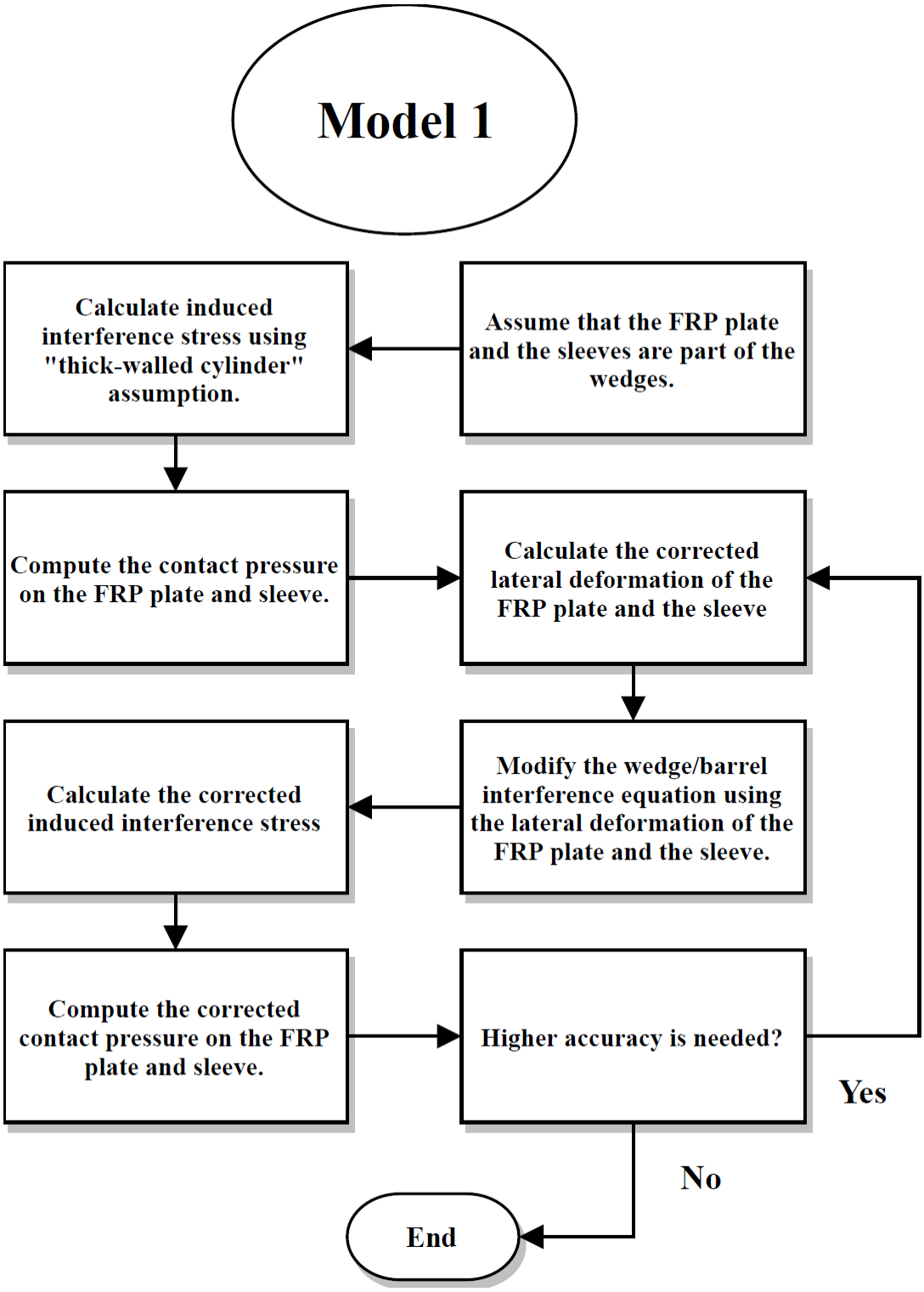


*Figure 5.3: Flowchart of the Methodology of Model 1*

### 5.4.2. Parameters of Model 1

The parameters considered in the development of the analytical model 1 are defined in Table 5.2.

*Table 5.2: Parameters of Analytical Model 1*

| Parameter | Definition |
|---|---|
| $\delta_{int}$ | Initial non-corrected interference. |
| $\delta_{int-mod}$ | Modified and corrected interference. |
| $r_1$ | Total radius of half-thickness FRP plate, one sleeve and one wedge combined. |
| $r_2$ | Barrel inner radius. |
| $r_3$ | Barrel outer radius. |
| $v_1$ | Poisson' s ratio of the wedges. |
| $v_2$ | Poisson' s ratio of the barrel. |
| $E_1$ | Modulus of elasticity of the wedges. |
| $E_2$ | Modulus of elasticity of the barrel. |
| $E_{FRP}$ | Transverse modulus of elasticity of the FRP plate. |
| $E_S$ | Modulus of elasticity of the sleeve. |
| $t_{FRP}$ | Thickness of half-thickness FRP plate. |
| $t_S$ | Thickness of the sleeve. |
| $W$ | Width of the FRP plate or the sleeve. |
| $P_{int}$ | Stress induced by interference between the wedge and the barrel. |
| $P_{int-mod}$ | Stress induced by the corrected interference between the wedge and the barrel. |
| $N_v$ | Averaged vertical load distribution on the FRP plate and the sleeve. |
| $N_{v-mod}$ | Corrected averaged vertical load distribution on the FRP plate and the sleeve. |
| $P_c$ | Contact pressure on the FRP plate and the sleeve. |
| $P_{c-mod}$ | Corrected contact pressure on the FRP plate and the sleeve. |
| $d_{FRP}$ | Transverse deformation of half-thickness FRP plate. |
| $d_S$ | Transverse deformation of the sleeve. |
| $d_W$ | Transverse deformation of half-thickness FRP plate and sleeve when modelled as part of the wedge |
| $d_{tot}$ | Total transverse deformation of half-thickness FRP plate and the sleeve combined. |

### 5.4.3. Analysis of Model 1

The thick-walled cylinder assumption is applied to compute the initial interference stresses between the barrel and each wedge which is then used to determine the initial contact pressure on the FRP plate and the sleeves. According to Qiu and Zhou [73], the stress induced by press-fitting a cylinder into another thick hollow cylinder is given by the equation **(5.11)**.

$$P_{int} = \frac{-\delta_{int}}{r_1\left(\frac{v_1 - 1}{E_1}\right) + \frac{r_2}{E_2}\left(\frac{r_2{}^2(v_2 - 1) - r_3{}^2(1 + v_2)}{r_3{}^2 - r_2{}^2}\right)} \tag{5.11}$$

The averaged vertical load distribution on the FRP plate and the sleeves at any point X across the length can be calculated by performing the integration shown in equation **(5.12)**.

$$N_V(X) = \frac{dF(X)}{dX} = \int_{\theta_1}^{\theta_2} P_{int} r_1 \sin(\theta)\, d\theta \tag{5.12}$$

Where the limit of the angle $\theta$ is $0 \leq \theta \leq \pi$.

Therefore, the initial averaged vertical load distribution is given by equation **(5.13)**.

$$N_V(X) = \frac{r_1 * (cos(\theta_2) - cos(\theta_1)) * (r_1 - r2)}{\frac{r_1 * (v - 1)}{E} + \frac{r_2 * \left(r_2{}^2(v - 1) - r_3{}^2(1 + v)\right)}{E * (r_3{}^2 - r_2{}^2)}} \tag{5.13}$$

Note that in equation **(5.12)**, the stress is multiplied with $r_1 d\theta$ to calculate the load distribution then multiplied by $\sin(\theta)$ to determine only the vertical component of the load distribution. The contact pressure on the FRP plate and the sleeve at any point X across the length can then be estimated simply by dividing the averaged vertical load distribution by the width of the FRP plate or the sleeve. The initial contact pressure ($P_c$) is given by equation **(5.15)**.

$$P_c = \frac{N_V}{W} \tag{5.14}$$

$$P_c(X) = \frac{r1 * (cos(\theta_2) - cos(\theta_1)) * (r1 - r2)}{\left(\frac{r1 * (v - 1)}{E} - \frac{r2 * \left((v - 1) * r2^2 + (-v - 1) * r3^2\right)}{E * (r2^2 - r3^2)}\right) W} \quad (5.15)$$

Since the same contact pressure is applied on both the FRP plate and the sleeve then total transverse deformation of the half-thickness FRP plate and the sleeve can be calculated as follows.

$$P_c = E_{2-FRP}\, \epsilon_{FRP} = E_S\, \epsilon_S \quad (5.16)$$

The transverse engineering strain is given by equation **(5.17)**.

$$\epsilon = \frac{deformation}{thickness} = \frac{d}{t} \quad (5.17)$$

Therefore, the total transverse deformation of the half-thickness FRP plate and the sleeve is given by equations **(5.18)** and **(5.19)**.

$$d_{tot} = d_{FRP} + d_S - d_W \quad (5.18)$$

$$d_{tot} = P_c \left(\frac{t_S}{E_S} + \frac{t_{FRP}}{E_{FRP}} - \frac{t_{FRP-S}}{E_1}\right) \quad (5.19)$$

Thus, the modified radius of each wedge at any angle $\theta$ can be determined by the following steps. The x and y components of the radius of each wedge are

$$x = r_1 \cos(\theta)$$

$$y = r_1 \sin(\theta)$$

The total transverse deformation of the half-thickness FRP plate and the sleeve is included in the y component of the radius as shown in equation **(5.20)**.

$$y = r_1 \sin(\theta) - d_{tot} \quad (5.20)$$

Hence, the modified radius of each wedge is given by equation **(5.21)**.

$$r_{1-mod} = \sqrt{x^2 + y^2} = \sqrt{(r_1 \cos(\theta))^2 + (r_1 \sin(\theta) - d_{tot})^2}$$

$$r_{1-mod} = \sqrt{{r_1}^2 - 2 r_1 d_{tot} \sin(\theta) + {d_{tot}}^2} \quad (5.21)$$

The modified interference is then calculated by equation **(5.22)**.

$$\delta_{int-mod} = r_{1-mod} - r_2 \tag{5.22}$$

The corrected interference stress is computed by substituting equation **(5.22)** into equation **(5.11)** to obtain equation **(5.23)**.

$$P_{int-mod} = \frac{-\delta_{int-mod}}{r_{1-mod}\left(\frac{v_1 - 1}{E_1}\right) + \frac{r_2}{E_2}\left(\frac{r_2{}^2(v_2 - 1) - r_3{}^2(1 + v_2)}{r_3{}^2 - r_2{}^2}\right)} \tag{5.23}$$

Thus, the corrected averaged vertical load distribution is calculated by equation **(5.24)**

$$Nv_{mod} = \int_{\theta_1}^{\theta_2} \frac{-\delta_{int-mod}\, r_{1-mod} \sin(\theta)\, d\theta}{r_{1-mod}\left(\frac{v_1 - 1}{E_1}\right) + \frac{r_2}{E_2}\left(\frac{r_2{}^2(v_2 - 1) - r_3{}^2(1 + v_2)}{r_3{}^2 - r_2{}^2}\right)} \tag{5.24}$$

The corrected contact pressure given by equation **(5.25)** is obtained by substituting equation **(5.24)** into equation **(5.14)**.

$$P_{c-mod}(X) = \int_{\theta_1}^{\theta_2} \frac{-\delta_{int-mod}\, r_{1-mod} \sin(\theta)\, d\theta}{W\left(r_{1-mod}\left(\frac{v_1 - 1}{E_1}\right) + \frac{r_2}{E_2}\left(\frac{r_2{}^2(v_2 - 1) - r_3{}^2(1 + v_2)}{r_3{}^2 - r_2{}^2}\right)\right)} \tag{5.25}$$

The integration given in equation **(5.25)** is not analytically possible to perform even with advanced mathematical software such as MATLAB. Therefore, this integration is performed numerically via MATLAB, and the results are shown in Section 5.6.2. The complex form of equation **(5.25)** is shown in Appendix A.

Note that this model has an iterative ability; thus, the accuracy of the results can enhanced further simply by substituting the corrected contact pressure calculated from equation **(5.25)** into equation **(5.19)** and following the exact same procedure. Note that the results obtained will converge after few iterations due to the fact that the thicknesses of the half-thickness FRP plate and the sleeve are much less than the thickness of the wedge; therefore, there is an optimal number of iterations that offers the highest accuracy with minimum computational power.

## 5.5. Analytical Model 2

### 5.5.1. Assumptions and Methodology of Model 2

Model 2 is a mathematically simplified model that is based on a combination of the thick-walled cylinder assumption and a new innovative assumption of varying mechanical properties. The assumption of varying mechanical properties is a modelling technique created to convert the wedge anchorage system into a much more simplified system that consists of one homogenous cylinder (barrel) and one non-homogenous cylinder (the FRP plate, the sleeves and the wedges combined). Both the modulus of elasticity and the Poisson's ratio of the non-homogenous cylinder are varying along the angle θ of the circular cross-section. The 1$^{st}$ step of this model is to apply the assumption of varying mechanical properties to convert the FRP plate, the sleeves and the wedges into a single non-homogenous cylinder with an equivalent modulus of elasticity and an equivalent Poisson's ratio. The 2$^{nd}$ step is using the thick-walled cylinder on the homogenous barrel and the non-homogenous inner cylinder to obtain the contact pressure on the FRP plate and the sleeve. The methodology of model 2 is summarized in the flowchart shown in Figure 5.4.

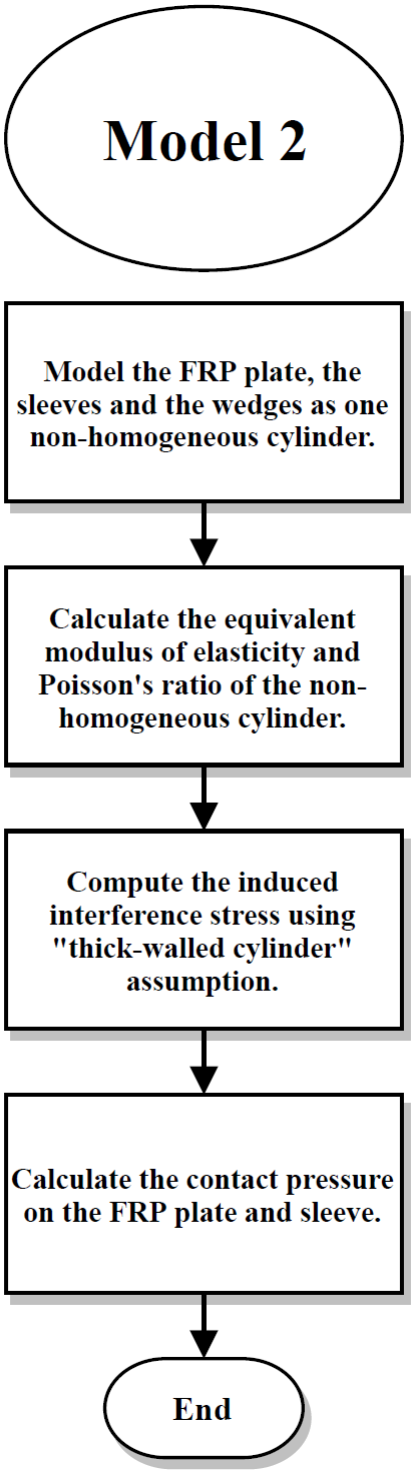


*Figure 5.4: Flowchart of the Methodology of Model 2*

### 5.5.2. Parameters of Model 2

The parameters considered in the development of the analytical model 2 are defined in Table 5.3.

*Table 5.3: Parameters of Analytical Model 2*

| Parameter | Definition |
|---|---|
| $\delta_{int}$ | Initial non-corrected interference. |
| $r_1$ | Total radius of half-thickness FRP plate, one sleeve and one wedge combined. |
| $r_2$ | Barrel inner radius. |
| $r_3$ | Barrel outer radius. |
| $r_{FRP}$ | Equivalent radius of half-thickness FRP plate. |
| $r_S$ | Equivalent radius of one sleeve. |
| $r_{FRP-S}$ | Equivalent radius of half-thickness FRP plate and one sleeve combined. |
| $r_W$ | Equivalent radius of one wedge |
| $v_1$ | Poisson' s ratio of the wedges. |
| $v_2$ | Poisson' s ratio of the barrel. |
| $v_{FRP}$ | Poisson' s ratio of the FRP plate. |
| $v_S$ | Poisson' s ratio of the sleeve. |
| $v_{eq}$ | Equivalent Poisson' s ratio of half-thickness FRP plate, a sleeve and a wedge. |
| $E_1$ | Modulus of elasticity of the wedges. |
| $E_2$ | Modulus of elasticity of the barrel. |
| $E_{FRP}$ | Transverse modulus of elasticity of the FRP plate. |
| $E_S$ | Modulus of elasticity of the sleeve. |
| $E_{eq}$ | Equivalent modulus of elasticity of half-thickness FRP plate, one sleeve and one wedge combined. |
| $t_{FRP}$ | Thickness of half-thickness FRP plate. |
| $t_S$ | Thickness of the sleeve. |
| $t_{FRP-S}$ | Thickness of half-thickness FRP plate and the sleeve combined. |
| $W$ | Width of the FRP plate or the sleeve. |
| $P_{int}$ | Stress induced by interference between the wedge and the barrel |
| $N_v$ | Averaged vertical load distribution on the FRP plate and the sleeve. |
| $P_c$ | Contact pressure on the FRP plate and the sleeve. |

### 5.5.3. Analysis of Model 2

After deriving the interference equations in Section 5.3.4, the next step is to calculate the equivalent radii of the half-thickness FRP plate, the sleeve and the wedge as a function of the angle ($\theta$) as shown in Figure 5.5 by using equations **(5.26)**, **(5.28)** and **(5.29)** respectively.

$$r_{FRP} = \frac{t_{FRP}}{\sin(\theta)} \tag{5.26}$$

$$r_{FRP-S} = \frac{t_{FRP-S}}{\sin(\theta)} \tag{5.27}$$

$$r_S = \frac{t_{FRP-S}}{\sin(\theta)} - \frac{t_{FRP}}{\sin(\theta)} = \frac{t_S}{\sin(\theta)} \tag{5.28}$$

$$r_W = r_1 - \frac{t_{FRP-S}}{\sin(\theta)} \tag{5.29}$$

The limit of the angle $\theta$ is given by equation **(5.30)**

$$tan^{-1}\left(\frac{2\,t_{FRP-S}}{W}\right) \leq \theta \leq \pi - tan^{-1}\left(\frac{2\,t_{FRP-S}}{W}\right) \tag{5.30}$$

Therefore, by applying the "Rule of Mixtures", the equivalent modulus of elasticity at any angle $\theta$ can be estimated by equation **(5.32)**.

$$\frac{1}{E_{eq}} = \frac{1}{r_1}\left(\left(\frac{r_{FRP}}{E_{FRP}}\right) + \left(\frac{r_S}{E_S}\right) + \left(\frac{r_W}{E_1}\right)\right) \tag{5.31}$$

$$\frac{1}{E_{eq}} = \frac{t_{FRP}}{r_1 E_{FRP}\sin(\theta)} + \frac{t_S}{r_1 E_S \sin(\theta)} + \frac{r_1\sin(\theta) - t_{FRP-S}}{r_1 E_1 \sin(\theta)} \tag{5.32}$$

By following the same concept, the equivalent Poisson's ratio is given by equation **(5.33)**. The results of equation **(5.31)** and **(5.33)** are shown in Figure 5.6.

$$\frac{1}{v_{eq}} = \frac{t_{FRP}}{r_1 v_{FRP}\sin(\theta)} + \frac{t_S}{r_1 v_S \sin(\theta)} + \frac{r_1\sin(\theta) - t_{FRP-S}}{r_1 v_1 \sin(\theta)} \tag{5.33}$$

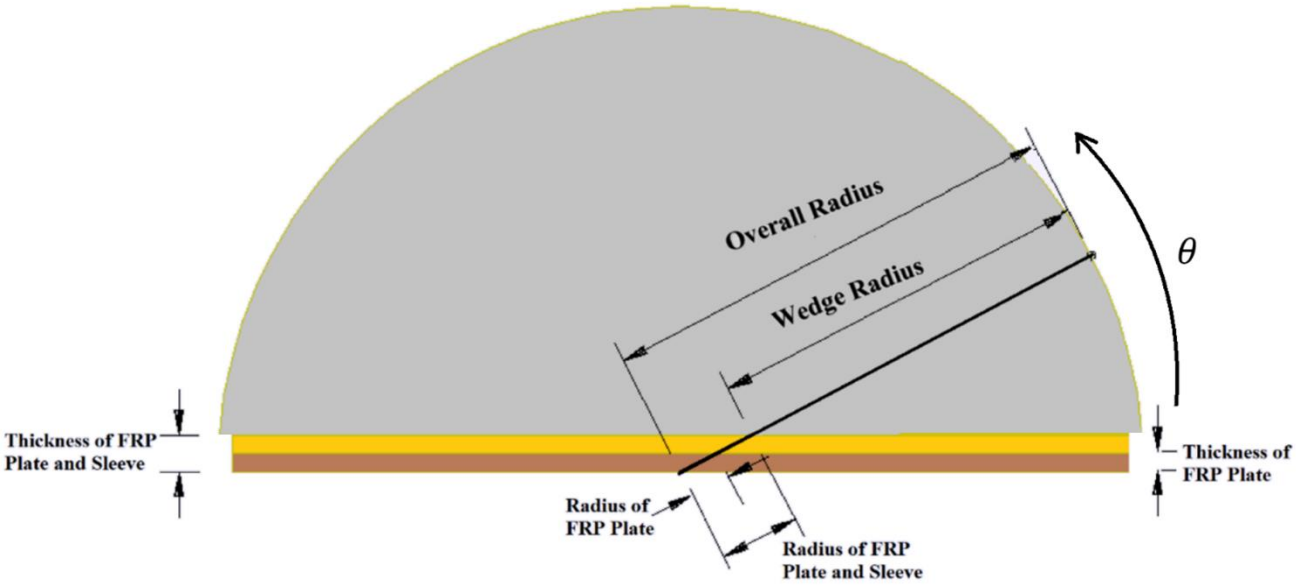


*Figure 5.5: Illustration of Parameters of Varying Mechanical Properties Assumption*

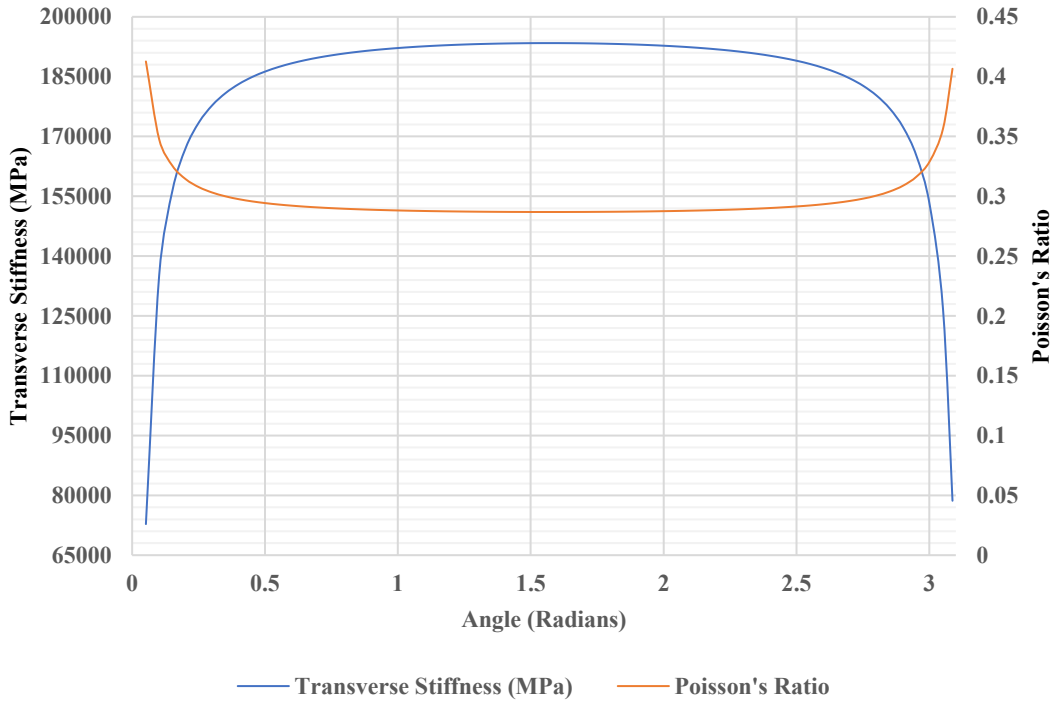


*Figure 5.6: Equivalent Modulus of Elasticity and Poisson's Ratio of Non-Homogenous Cylinder*

The thick-walled cylinder assumption is applied to compute the interference stresses between the barrel and the inner non-homogenous cylinder. By substituting the equivalent modulus of elasticity and the equivalent Poisson's ratio of the non-homogenous cylinder calculated by equations **(5.32)** and **(5.33)** respectively into equation **(5.11)**, the interference stress can then be determined by equation **(5.34)**.

$$P_{int} = \frac{-\delta_{int}}{r_1\left(\frac{v_{eq}-1}{E_{eq}}\right) + \frac{r_2}{E_2}\left(\frac{{r_2}^2(v_2-1) - {r_3}^2(1+v_2)}{{r_3}^2 - {r_2}^2}\right)} \tag{5.34}$$

The averaged vertical load distribution on the FRP plate and the sleeve at any point X across the length can be found by performing the integration shown in equation **(5.35)**.

$$N_V(X) = \frac{dF(X)}{dX} = \int_{\theta_1}^{\theta_2} P_{int}\, r_1 \sin(\theta)\, d\theta \tag{5.35}$$

Note that in equation **(5.35)**, the stress is multiplied with $r_1 d\theta$ to calculate the load distribution then multiplied by $\sin(\theta)$ to calculate only the vertical component of the load distribution. The contact pressure on the FRP plate and the sleeve at any point X across the length can then be calculated simply by dividing the averaged vertical load distribution by the width of the FRP plate as shown in equation **(5.14)**. Therefore, the FRP plate contact pressure ($P_c$) is given by equation **(5.36)**.

$$P_c(X) = \int_{\theta_1}^{\theta_2} \frac{-\,r_1\,\delta_{int}\sin(\theta)\,d\theta}{W\left(r_1\left(\frac{v_{eq}-1}{E_{eq}}\right) + \frac{r_2}{E_2}\left(\frac{{r_2}^2(v_2-1) - {r_3}^2(1+v_2)}{{r_3}^2 - {r_2}^2}\right)\right)} \tag{5.36}$$

Note that the integration given in equation **(5.36)** is not analytically possible to perform even with advanced mathematical software such as MATLAB. Therefore, this integration is performed numerically via MATLAB, and the results are shown in Section 5.6.2. The complex form of equation **(5.36)** is shown in Appendix B.

## 5.6. Verification of Analytical Models

### 5.6.1. Inputs of the Verification Process

In order to confirm the accuracy of the results obtained from the FEM analysis, the two analytical models are tested using the results of three different FEM models. Note that all three FEM models are made of the same essential elements and dimensions; however, the presetting distance of the wedges into the barrel is varied. The considered mechanical properties, previously shown in Chapter 3, are listed in Table 5.4. A brief summary of the dimensions of both the wedges and the barrel considered in the analytical models is shown in Table 5.5. The presetting distance and the extra length used for each tested model are provided in Table 5.6.

*Table 5.4: Mechanical Properties Considered in the Analytical Models*

| Element | Modulus of Elasticity (MPa) | Poisson's Ratio |
|---|---|---|
| **CFRP plate** | 13,580 | 0.523 |
| **Annealed Copper Sleeve** | 117,210 | 0.33 |
| **Steel Wedge** | 200,000 | 0.28 |
| **Steel Barrel** | 200,000 | 0.28 |

*Table 5.5: Summary of the Dimensions of the Wedges and the Barrel Considered in the Analytical Models*

| | Wedge | Barrel |
|---|---|---|
| **Inner Radius (mm)** | -------- | 25.5 |
| **Outer Radius (mm)** | 25.545 | 38.12963 |
| **Radius of Circular Profile (mm)** | 1750 | 1750 |
| **Length of Circular Segment ($X_2$) (mm)** | 55 | 55 |
| **Slope of Linear Profile** | 0.03862958 | 0.03862958 |
| **Total Anchorage Length ($X_3$) (mm)** | 70 | 70 |

*Table 5.6: Presetting Distances and Extra Lengths of Tests Considered for Verifying the Accuracy of the Analytical Models*

| Test No. | Presetting Displacement (mm) | $x_{extra}\ (mm)$ |
|---|---|---|
| **Test 1** | 6 | 8.3 |
| **Test 2** | 9 | 5.3 |
| **Test 3** | 12 | 2.3 |

### 5.6.2. Results of the Verification Process

The contact pressure on the FRP plate and the sleeve is computed through the numerical FEM model as well as the two analytical models, and the results are shown in Figure 5.7. The root-mean-squared error of the results is calculated by the equation **(5.37)** and listed in Table 5.7 [74]. Note that performing only two iterations on model 1 is sufficient to converge its outcomes as illustrated in Table 5.8. It is worth mentioning that although model 1 and model 2 are based on completely different assumptions, both models provide almost identical results. This fact confirms the creditability of the analytical models.

$$RMS_{avg}\ Error = \frac{1}{N}\sqrt{\sum_{i=1}^{N}\left(\frac{P_{C\_Analytical} - P_{C\_FEM}}{P_{C\_Analytical}}\right)} \quad (5.37)$$

*Table 5.7: RMS Error of the Tests Considered for Verifying the Accuracy of the Analytical Models*

| Test No. | RMS Error Model 1 (Before Iteration) | RMS Error Model 1 (After Iteration) | RMS Error Model 2 |
|---|---|---|---|
| Test 1 | 5.671% | 5.658% | 5.656% |
| Test 2 | 4.842% | 5.025% | 4.989% |
| Test 3 | 5.383% | 5.604% | 5.576% |

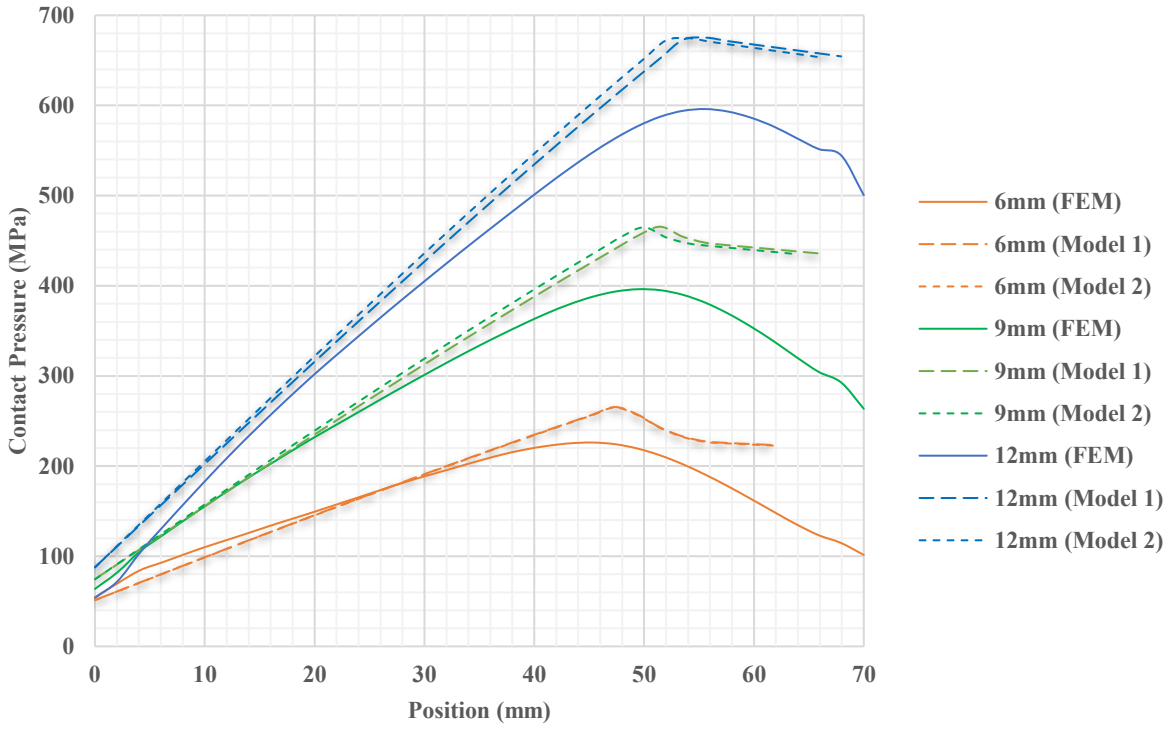


*Figure 5.7: Averaged CFRP Plate Contact Pressure Curves for both FEM Model and Analytical Models*

*Table 5.8: RMS Error of Model 1 of the Tests Considered After Performing Iteration*

| Iteration No. | Test 1 | Test 2 | Test 3 |
|---|---|---|---|
| No Iteration | 5.671% | 4.842% | 5.383% |
| Iteration 1 | 5.658% | 5.046% | 5.624% |
| Iteration 2 | 5.658% | 5.023% | 5.602% |
| Iteration 3 | 5.658% | 5.025% | 5.604% |
| Iteration 4 | 5.658% | 5.025% | 5.604% |
| Iteration 5 | 5.658% | 5.025% | 5.604% |

## 5.7. Summary

Analytical modelling of a wedge anchorage utilized for anchoring FRP plates is a challenging process due to the existence of contact discontinuity and stress concentration between the wedges, the sleeves and the FRP plate. Two analytical models are created in this chapter. While model 1 is solely based on the thick-walled cylinder assumption, model 2 is based on the thick-walled cylinder assumption in addition to the new assumption of varying mechanical properties.

Both analytical models proved their potentials and credibility by providing almost identical results with excellent accuracy. Both models consist of mathematically sophisticated equations which are solved numerically through MATLAB. Even though the two analytical models are used solely to confirm the accuracy of the FEM results, both models have the potential to be utilized to optimize a wedge anchorage more efficiently as they can predict the gripping strength of an anchorage in a matter of seconds instead of hours using FEM analysis.

# 6

# Experimental Testing

## 6.1. Introduction

After selecting the most suitable materials for the wedge anchorage (Chapter 3), designing the wedge anchorage with the optimal dimensions (Chapter 4), and verifying the results of the FEM model using two analytical models (Chapter 5), the optimized wedge anchorage is manufactured and tested. This chapter describes the assembling, presetting, loading processes performed and instruments employed in each test. Several successful tensile loading tests are conducted to investigate the performance of the wedge anchorage. The experimental outcomes are compared to the FEM results to validate the accuracy of the FEM model. The effect of the presetting distance on the CFRP plate slipping is studied. Damage analysis is performed to examine the reusability of the optimized wedge anchorage.

## 6.2. Objectives

The main objectives of the experimental analysis are as follows:

- Investigating the performance of the optimized wedge anchorage,
- Validating the accuracy of the FEM model by comparing its results with the experimental results,
- Studying the effect of the presetting distance on the CFRP plate slipping, and
- Examining the reusability of the optimized wedge anchorage by investigating the induced plastic deformation within the wedge anchorage.

## 6.3. Test Elements

The elements involved in each experimental test are one CFRP plate, four annealed and heat-treated copper sleeves, a relatively larger reusable dead-end wedge anchorage, and the optimized wedge anchorage. The larger reusable dead-end anchorage is used solely to anchor one side of the CFRP plate; thus, all test elements, except for the larger dead-end wedge anchorage, are briefly described.

### 6.3.1. CFRP Plate

The tested CFRP plate, shown in Figure 6.1, is manufactured by SIKA with a reported tensile strength of 2,800 MPa [48]. The length, the width and the thickness of the CFRP plate are 1 m, 50 mm and 1.2 mm, respectively.

*Figure 6.1: CFRP Plate*

### 6.3.2. Annealed Copper Sleeves

Annealed copper sleeves, shown in Figure 6.2, are purchased from McMaster Carr [59]. Two copper sleeves are used in each anchorage. The length, the width and the thickness of the sleeves of the optimized anchorage are 75 mm, 50 mm and 0.81 mm, respectively. The sleeves are softened further by heat-treatment for an hour at a temperature of $500^{o}C$.

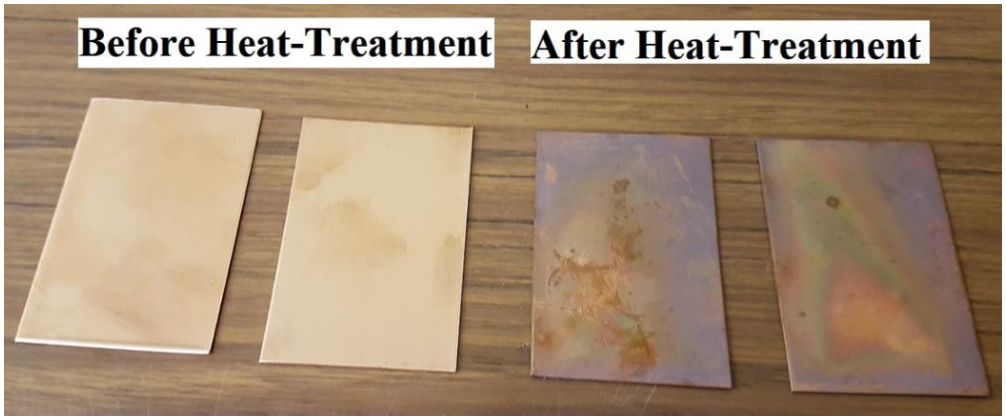


*Figure 6.2: Annealed Copper Sleeves Before and After Heat-Treating*

### 6.3.3. Optimized Wedge Anchorage

The optimized wedge anchorage, shown in Figure 6.3, is machined using "VF-4 CNC Vertical Mill" machine for high cutting precision. Since steel and stainless-steel grades have almost identical mechanical properties but with different yield, shear and tensile strengths then manufacturing the wedge anchorage from any steel grade should not affect its performance as long as the yield strength of the steel grade is higher than the maximum von Mises stress within the optimized anchorage. Thus, the optimized wedge anchorage is manufactured from heat-treated 4140 steel instead of 440C stainless steel for economical consideration. The mechanical properties of the heat-treated 4140 steel and 440C stainless steel are listed in Table 6.1. The second end of the CFRP plate is gripped using a larger reusable wedge anchorage system that is made of hardened steel.

*Table 6.1: Mechanical Properties of 4140 Steel and 440C Stainless Steel*

| Properties | 4140 Steel | 440C Stainless Steel |
|---|---|---|
| $\sigma_{Ult}\ (MPa)$ | 1450[1] | 1965[2] |
| $\sigma_{Y}\ (MPa)$ | 1340[1] | 1896[2] |
| $\tau_{12}\ (MPa)$ | 773[4] | 1094[4] |
| $\epsilon_{Ult}\ (\%)$ | 15%[1] | 2%[2] |
| $E_1, E_2\ and\ E_3\ (MPa)$ | 200,000[3] | 200,000[3] |
| $v_{12}\ , v_{13}\ and\ v_{23}$ | 0.285[3] | 0.285[3] |
| $G_{12}, G_{13}\ and\ G_{23}\ (MPa)$ | 77,821[4] | 77,821[4] |
| $\rho\ (\frac{g}{cm^3})$ | 7.8[3] | 7.8[3] |

[1] Book Chapter Titled "Ultrahigh Strength Steel: Development of Mechanical Properties Through Controlled Cooling" [75]

[2] Nickel Development Institute, Canada [61]

[3] AZoM online publication for the Materials Science community [65], [76]

[4] Calculated Analytically

*Figure 6.3: Optimized Wedge Anchorage*

## 6.4. Testing Procedure

Three main processes are performed in each experimental test which are assembling, presetting and loading processes. Each process along with the employed apparatus are discussed in detail.

### 6.4.1. Assembling Process

The first step of the assembling process is cleaning the CFRP plate, the sleeves, the wedges and the barrels using acetone. The CFRP plate, the sleeves and the wedges of each anchorage are assembled together as shown in Figure 6.4. A high pressure lubricant (Molykote G-n Metal Assembly Paste) is then applied on the interior surface of each barrel as well as the exterior surfaces of the wedges to facilitate wedges movement into the barrel [77]. Lubrication must be applied carefully as placing lubricant on the sleeve-wedge interface and/or the CFRP plate-sleeve interface would deteriorate the anchoring strength of the wedge anchorage leading to CFRP plate slipping or premature failure.

The CFRP plate, the sleeves and the wedges are then carefully inserted into the barrel. Full attention has been paid to the insertion process to avoid any misalignment, such as inserting one wedge more than the other or shifting the CFRP plate to one side of the wedge anchorage. The wedges are then hammered into the barrel to fix the assembled elements together. The assembled wedge anchorages are shown in Figure 6.5.

*Figure 6.4: Assembled Wedges before Lubrication*

*Figure 6.5: Assembled Wedge Anchorages and CFRP Plate*

### 6.4.2. Presetting Process

After assembling the two wedge anchorages to the CFRP plate, the wedges are push further into the barrels by a specific presetting distance using the presetting rig shown in Figure 6.6 (A). The wedge anchorage is placed on top of the supports such that the presetting edge (edge 2) of the anchorage is facing the pressing head of the rig, as shown in Figure 6.6 (B). Two short steel rods of the same length are used to equally push the wedges into the barrel. The applied hydraulic pressure and the presetting distance are measured using a pressure gauge and a caliper respectively. In some tests, the presetting rig is not used and replaced by the light hammering of the wedges.


*Figure 6.6: (A) Presetting Rig Apparatus (B) Setup of the Anchorage in the Presetting Rig Apparatus*

### 6.4.3. Tensile Loading Process

The loading test rig, shown in Figure 6.7 (A), is utilized to test the performance of the optimized wedge anchorage by applying a displacement-controlled loading of 0.6 mm/min. Note that the reusable large dead-end anchorage is placed at the bottom since its sole purpose is gripping one side of the CFRP plate; therefore, no measurement is collected at this end. On the other hand, the optimized wedge anchorage is placed at the top where more space is provided for displacement measurement instrumentations. Two Linear Variable Differential Transducers (LVDTs) are installed to measure the relative displacement of the anchorage components with respect to the barrel as shown in Figure 6.7 (B). The first LVDT is used to measure the insertion distance of the wedges into the barrel as the tensile loading is applied. The other LVDT is used to measure accumulative slipping of the CFRP plate and wedges. Preliminary investigation shows no relative displacement between sleeve and wedges. Therefore, the CFRP slipping is computed by subtracting the readings of both LVDTs.

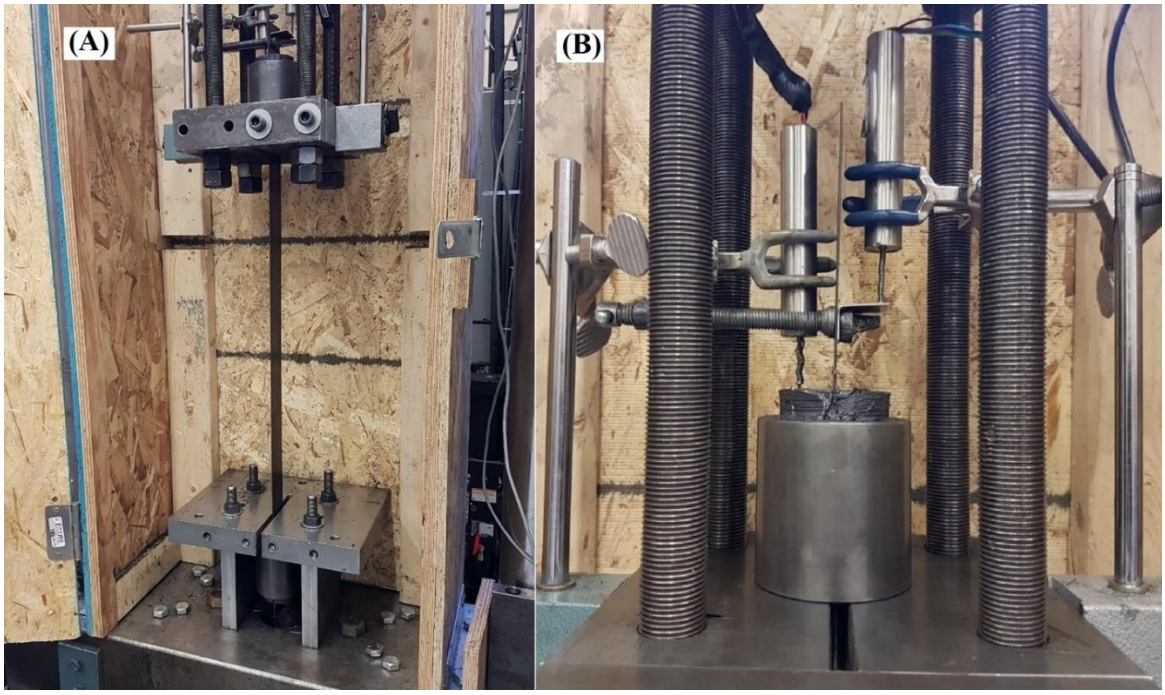


*Figure 6.7: (A) Loading Test Rig (B) Setup of the LVDTs*

## 6.5. Results

### 6.5.1. General

A total of eight tensile loading tests are conducted. The first two tests, tests 1 and 2, are conducted using hard copper sleeves. The remaining six tests are performed using heat-treated copper sleeves. The optimized wedge anchorage is presetted by the presetting rig in the first five tests. In the last three tests, the presetting rig is not used; instead, the optimized wedge anchorage is simply hammered. The applied presetting distances are listed in Table 6.2. The reusable dead-end wedge anchorage is presetted via the presetting rig in every test to minimize CFRP plate slipping using a presetting load ranging between 200 kN-240 kN. A displacement-controlled loading of 0.6 mm/min is applied until failure. An explosive fracture of the CFRP plate shown in Figure 6.8 is observed in every test. The fractured CFRP plate, shown in Figure 6.9, confirms that failure occurs outside the anchored area of the CFRP plate once the tensile strength of the CFRP plate is reached. Based on failure observation of the plate at both anchorages, it seems that the CFRP fracture is initiated at the dead-end wedge anchorage in every test indicating that the full gripping strength of the optimized wedge anchorage can be higher than that reported results. Advanced monitoring, such as high-quality video recording, can be considered in the future to obtain better understanding of the failure process of the CFRP plate. The deformed sleeves, shown in Figure 6.10, prove that no slipping occurred between the sleeves and the wedges as the top surface of each sleeve is not scratched. The general behaviour of the experimental results is shown in Figure 6.11. Higher presetting of the wedge anchorage would result in a less displacement of components; thus, test 5 is predicted to the smallest induced displacement compared to the other tests.

*Table 6.2: Presetting Distances of Tests Performed*

| Test No. | Presetting Method | Presetting Distance (mm) |
|---|---|---|
| **1** | Presetting Rig | 2.9 |
| **2** | Presetting Rig | 4.6 |
| **3** | Presetting Rig | 3.4 |
| **4** | Presetting Rig | 4.17 |
| **5** | Presetting Rig | 4.89 |
| **6** | Hammering | 1.8 |
| **7** | Hammering | 1.8 |
| **8** | Hammering | 1.85 |

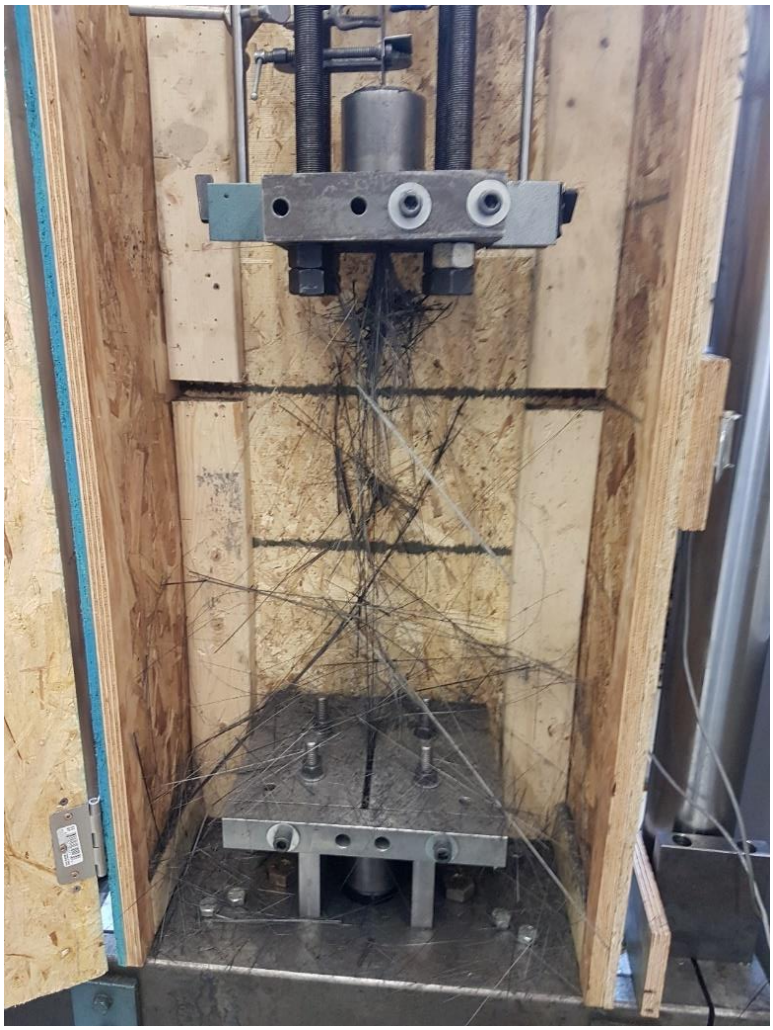

*Figure 6.8: CFRP Plate Explosive Fracture*

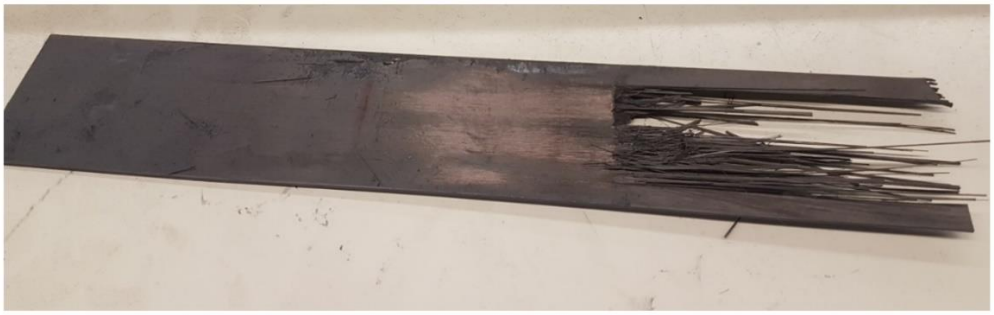

*Figure 6.9: Fractured CFRP Plate*

*Figure 6.10: Damaged Copper Sleeves after Testing*

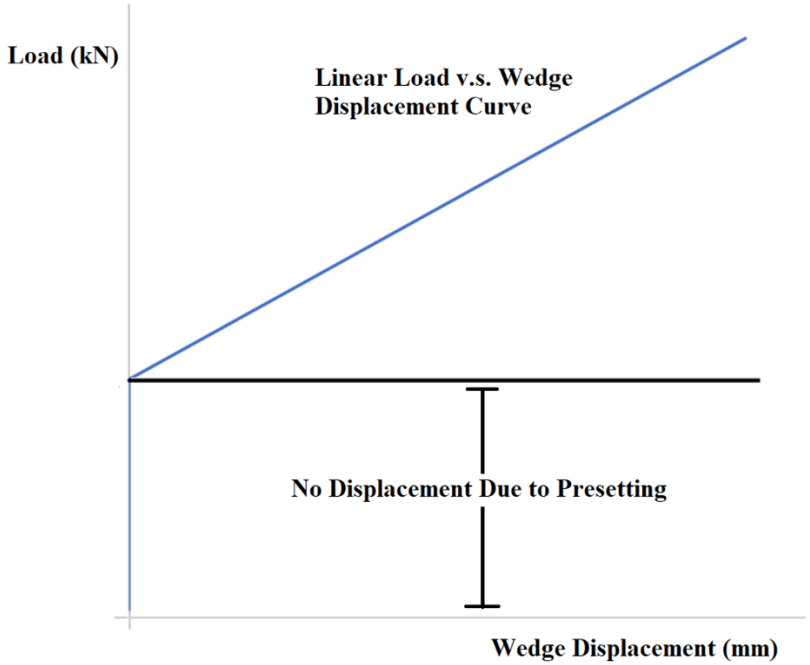


*Figure 6.11: General Load vs Wedge Displacement Behavior of the Results*

### 6.5.2. Experimental Results

The experimental results are presented in two separate sections based on the presetting method performed.

#### 6.5.2.1. Presetting via Presetting Rig

Three tests are conducted using different presetting distances. The applied hydraulic pressure ($P$) on the shaft of the presetting rig is measured using pressure gauge. The shaft diameter ($D$) of the presetting rig is 101 mm. Thus, the presetting load ($F$) is given by equation **(6.1)**. The presetting load applied on the optimized anchorage and the resulted presetting distance for each test are summarized in Table 6.3. A presetting load of 200 kN is applied on the reusable dead-end anchorage. CFRP premature failure occurred in tests 1 and 2 at a tensile loading of 91% and 94% of the tensile strength respectively when hard copper sleeves are used. CFRP premature failure is overcomed in the other tests by softening the copper sleeves with heat treatment.

The recorded wedge displacement of the optimized anchorage as tensile loading is applied for tests 3,4 and 5 is shown in Figure 6.12 along with the FEM results. The CFRP plate displacement for tests 3,4 and 5 is plotted against the wedge displacement in Figure 6.13. As illustrated in Figure 6.12, there is an excellent agreement between the experimental results and the FEM results. The maximum tensile loading reached and the recorded CFRP plate slipping of each test are listed in Table 6.4. The effect of the presetting distance on the CFRP slipping is shown in Figure 6.14. As illustrated in Figure 6.14, the presetting distance is inversely proportional to the CFRP slipping; however, the effect of the presetting distance on the CFRP slipping becomes almost redundant once the presetting distance exceeds 4.45 mm.

$$F = P\left(\pi \frac{D^2}{4}\right) \tag{6.1}$$

*Table 6.3: The Applied Presetting Pressure (Presetting Load) and the Induced Presetting Distance of the Optimized Anchorage*

| Test No. | Presetting Pressure (bar) | Presetting Load (kN) | Presetting Distance (mm) |
|---|---|---|---|
| **1** | 20 | 13.5 | 2.9 |
| **2** | 130 | 104 | 4.6 |
| **3** | 50 | 40.1 | 3.4 |
| **4** | 100 | 80.1 | 4.17 |
| **5** | 150 | 120.2 | 4.89 |

*Table 6.4: The Presetting Distance of the Optimized Anchorage, the Maximum Tensile Load Reached and CFRP Slipping Recorded*

| Test No. | Presetting Distance (mm) | Maximum Tensile Load (kN) | Load to Strength Ratio (%) | CFRP Slipping (mm) |
|---|---|---|---|---|
| **Using Hard Sleeve** | | | | |
| **1** | 2.9 | 151.92 | 90.43% | 2.128 |
| **2** | 4.6 | 157.04 | 93.5% | 0.446 |
| **Using Soft Sleeve** | | | | |
| **3** | 3.4 | 173.98 | 103.6% | 0.6 |
| **4** | 4.17 | 171.94 | 102.4% | 0.287 |
| **5** | 4.89 | 167.8 | 99.9% | 0.253 |

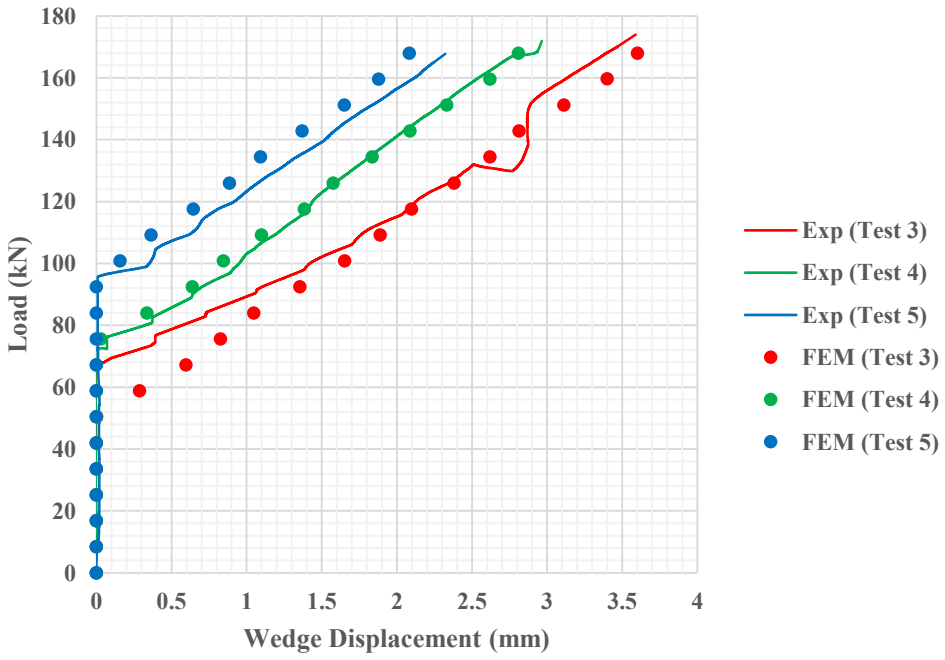


*Figure 6.12: Tensile Load (kN) VS Wedge Displacement (mm) of High Presetting Levels Using Presetting Rig*

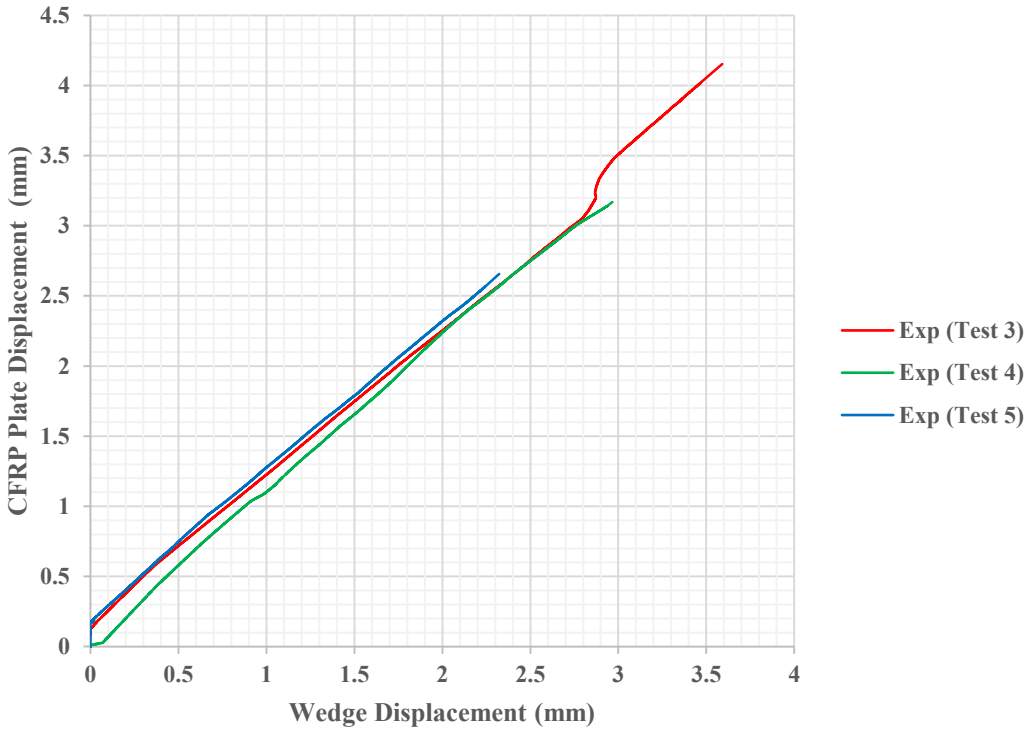


*Figure 6.13: CFRP Plate Displacement VS Wedge Displacement (mm) of Presetted Tests through Presetting Rig*

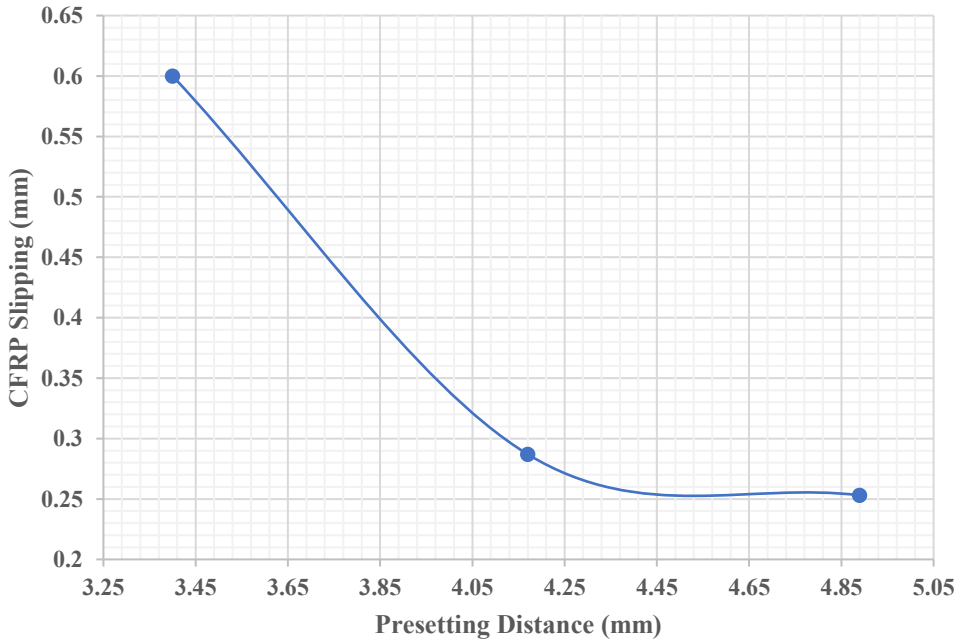


*Figure 6.14: Effect of Presetting Distance on CFRP Slipping*

#### 6.5.2.2. Presetting by Hammering

Three tests are performed by hammering the optimized wedge anchorage. The presetting distance for each test is summarized in Table 6.5. The dead-end anchorage is presetted with a presetting load of 200 kN in tests 6 and 7 while a presetting load of 240 kN is applied in test 8. The recorded wedge displacement as tensile loading is applied is shown in Figure 6.15 along with the FEM results. The CFRP plate displacement is plotted against the wedge displacement in Figure 6.16. As illustrated in Figure 6.15, there is a good agreement between the experimental results and the FEM results; however, the experimental results of Test 6 is not as accurate as the other tests which is believed be due to wedge misplacement caused by hammering one wedge more than the other. It is crucial to mention that the maximum tensile loading reached is 183.622 kN (109.3%) which is achieved by presetting the dead-end anchorage with a presetting load of 240 kN. This gives an indication that harder presetting of the dead-end anchorage would improve its performance and allow reaching higher tensile loading without inducing CFRP failure. Since CFRP failure is likely caused by the dead-end anchorage in each test then it is possible to conclude that the optimized anchorage can effectively grip CFRP plate without inducing CFRP failure until a tensile loading of at least 183.622 kN (109.3%) is applied.

*Table 6.5: The Presetting Distance of the Optimized Anchorage, the Maximum Tensile Load Reached and CFRP Slipping Recorded*

| Test No. | Presetting Distance (mm) | Maximum Tensile Load (kN) | Load to Strength Ratio (%) | CFRP Slipping (mm) |
|---|---|---|---|---|
| **6** | 1.85 | 166.893 | 99.34% | 2.28 |
| **7** | 1.8 | 167.331 | 99.6% | 0.906 |
| **8** | 1.8 | 183.622 | 109.3% | 0.596 |

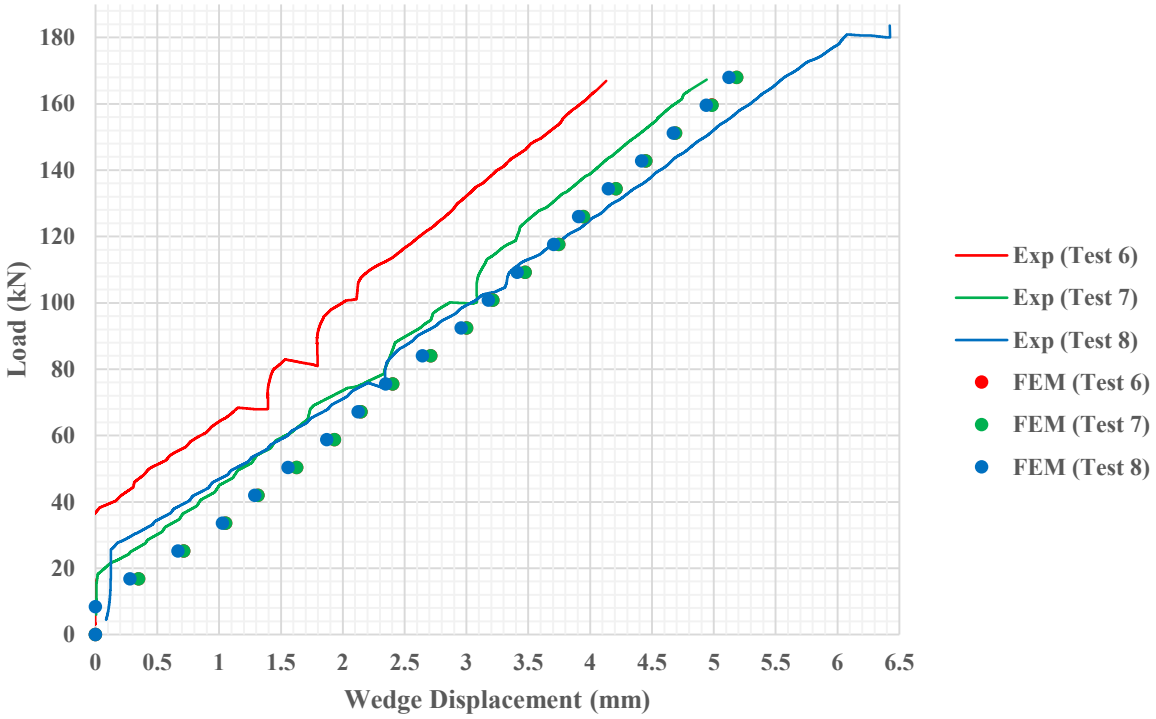


*Figure 6.15: Tensile Load (kN) VS Wedge Displacement (mm) of Presetted Tests through Hammering*

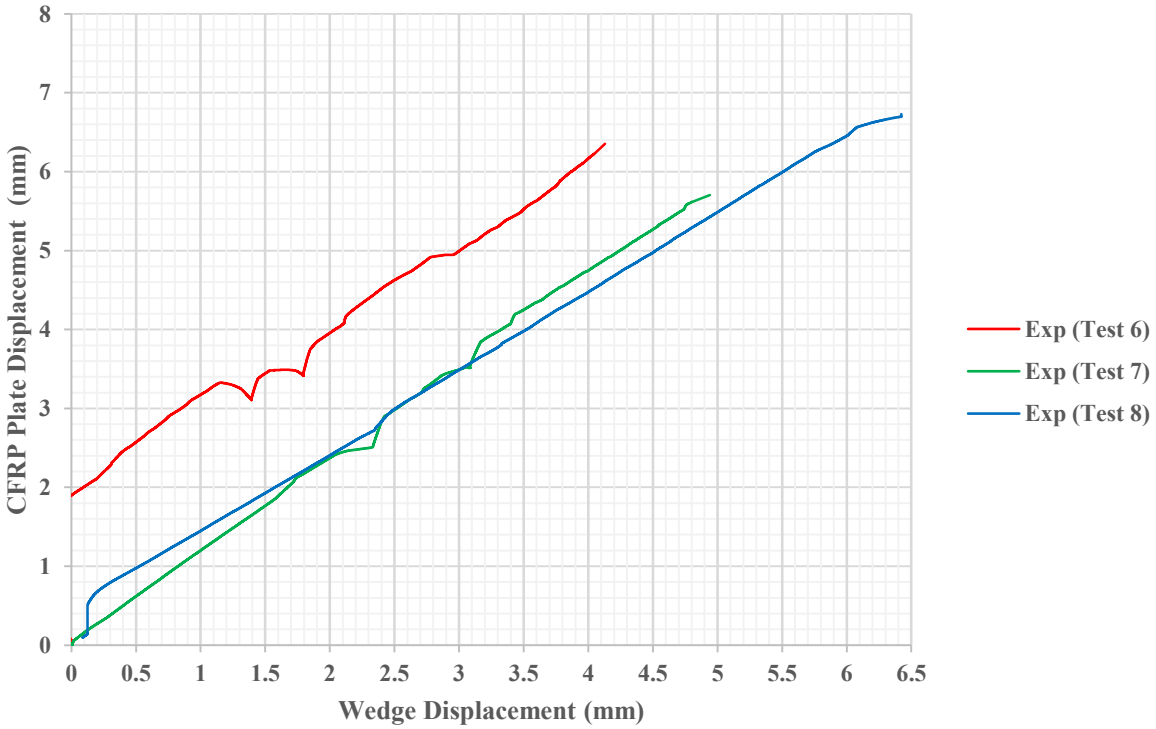


*Figure 6.16: CFRP Plate Displacement VS Wedge Displacement (mm) of Low Presetting Using Hammering*

### 6.5.3. Damage Analysis

After performing a total of eight tests, the plastic deformation within the wedges and the barrel of the optimized wedge anchorage is observed. The deformed wedge and barrel are shown in Figure 6.17 and Figure 6.18 respectively. As illustrated in Figure 6.17 and Figure 6.18, minor plastic deformation occurred at the loading edge of the wedges and the barrel; however, this plastic deformation does not affect the performance of the wedge anchorage as most of the induced interference stress is within the linear segments of the wedges and the barrel. Note that the machining pattern is still visible in the wedges and the barrel which proves the absence of plastic deformation. Since minor plastic deformation is induced after performing eight tests then it is possible to conclude that the optimized wedge anchorage has a high reusability which may exceed 10 times of usage.

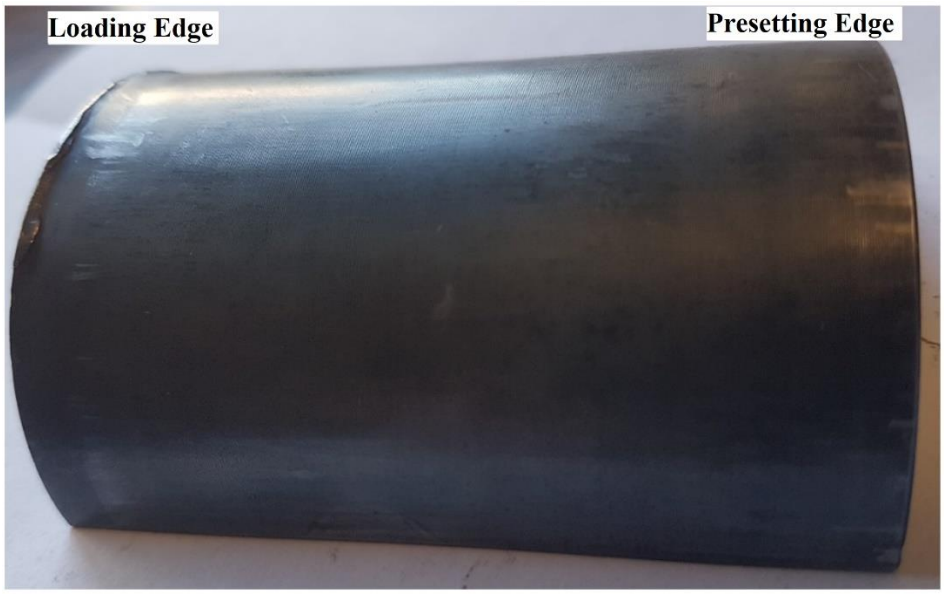


*Figure 6.17: Deformed Wedge*

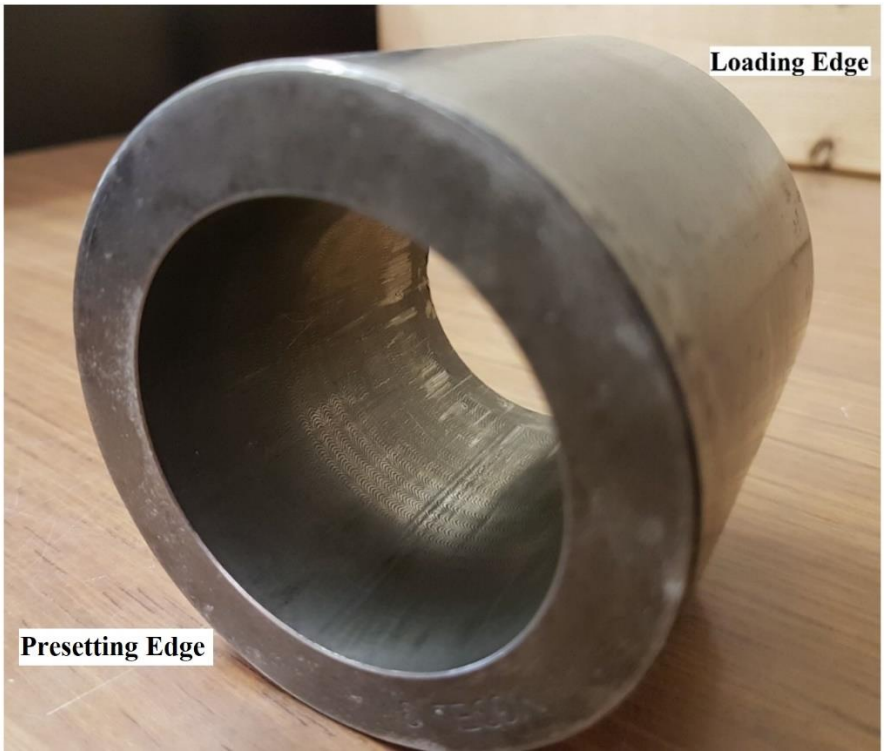


*Figure 6.18: Deformed Barrel*

## 6.6. Discussion

A total of eight experimental tests are conducted. CFRP premature failure occurred in two tests when hard copper sleeves are used. Softening the copper sleeves by heat-treatment for an hour at a temperature of $500^{o}C$ is sufficient to prevent premature failure of the CFRP plate. The optimized wedge anchorage illustrated its high performance by successfully gripping the CFRP plate until the occurrence of tensile failure. The tensile loading reached in the presented tests is ranging from 99.34% to 109.3% of the tensile strength of the CFRP plate and the recorded CFRP slipping is 0.25-0.6 mm when presetting process is performed; thus, it is possible to conclude that the optimized anchorage can effectively grip the CFRP plate by utilizing the full reported tensile strength of the CFRP plate without inducing premature failure.

The effect of the presetting distance on the CFRP plate slipping is investigated and shown in Figure 6.14. The presetting distance is inversely proportional to the CFRP plate slipping; however, once the presetting distance exceeds 4.45 mm, the effect of the presetting distance on the CFRP slipping becomes almost redundant.

The experimental results are compared to the FEM results in Figure 6.12 and Figure 6.15. It is clear from the figures that there is an excellent agreement between the experimental results and the FEM results which verifies the accuracy of the FEM model developed in Chapter 4. The experimental results of Test 6 shown in Figure 6.15 is not as accurate as the other tests which is likely due to an existing wedge misplacement created during the hammering process. It is worth mentioned that despite the existence of wedge misplacement, the reported CFRP tensile strength is reached which illustrates the outstanding performance of the optimized anchorage.

After performing eight tests, damage analysis is conducted to investigate the reusability of the optimized wedge anchorage. Minimal plastic deformation in the form of surface scratching is observed mainly at the loading edge of the wedges and the barrel as shown in Figure 6.17 and Figure 6.18 respectively; however, this plastic deformation is not expected to affect the performance of the optimized wedge anchorage since the interference and the induced stress within the barrel and the wedges are minimum at the loading edge.

## 6.7. Summary

The optimized wedge anchorage and the dead-end wedge anchorage are manufactured with a heat-treated 4140 steel. Eight tensile tests are performed Hard copper sleeves are used in the first two tests while heat-treated copper sleeves are employed in the other six tests. The dead-end anchorage is presetted using a presetting rig in every single test to prevent CFRP slipping. The optimized anchorage is presetted using presetting rig in the first five tests and hammered in the other three tests. CFRP premature failure occurred when hard copper sleeves are used. Softening the copper sleeves by heat-treatment for an hour at a temperature of $500^oC$ is sufficient to avoid CFRP premature failure. The maximum recorded tensile strength is 3,060.4 MPa representing 109.3% of the reported tensile strength of the CFRP plate. The recorded CFRP slipping is 0.25-0.6 mm when presetting process is performed. The accuracy of the FEM model is verified by comparing its results to the experimental results. The effect of the presetting distance on the CFRP plate slipping is investigated, and it is found that the effect of the presetting distance is almost redundant once the presetting distance exceeds 4.45 mm. Finally, damage analysis is conducted after performing eight tensile tests to confirm the reusability of the optimized wedge anchorage. It is observed that minimal plastic deformation occurred at the loading edge of the barrel and the wedges which is not expected to affect the performance of the optimized wedge anchorage as minimum stress is induced within the barrel and the wedge at the loading edge. Thus, it is concluded that the optimized anchorage has an excellent reusability that might exceed 10 times of usage.

# 7

# Conclusions and Recommendations

## 7.1. General

The presented work investigates the development and optimization of an innovative anchorage to grip CFRP plates that is reliable, reusable, compact and light in weight. To fulfil these requirements, a wedge anchorage is chosen as the most suitable system. Material selection process is conducted to select the optimal materials for the sleeves, the wedges and the barrel of the anchorage. 440C stainless steel is selected as the most suitable material for the wedges and the barrel due to its high yield strength and excellent corrosion resistance. Soft and hard annealed copper sleeves are used to improve the gripping strength of the optimized anchorage.

An FEM model of the wedge anchorage is developed using ABAQUS finite element package. An optimization process is performed to find the optimal dimensions of the anchorage through which the anchoring strength and the reusability are improved. The effect of the presetting distance on the performance of the optimized anchorage is studied. Several failure theories are used to investigate the likelihood of CFRP premature failure. Two new analytical models are developed to verify the accuracy of the FEM model. The results of the analytical models are compared well to the FEM results.

The optimized wedge anchorage is manufactured and tested to evaluate its performance by gripping its ends using the optimized anchorage and a larger dead-end anchorage. The dead-end anchorage is presetted in every test to avoid CFRP slipping. The optimized anchorage system is capable to carry the reported ultimate tensile strength of the CFRP plate when soft sleeves are used. The effect of presetting distance on the CFRP slipping is investigated. Damage analysis is performed after conducting eight tensile tests to examine the reusability of the optimized wedge anchorage.

## 7.2. Conclusions

### 7.2.1. Optimization Analysis

- The designed wedge anchorage is optimized by studying the effect of varying the slope of its linear segments, the radius of its circular segments and the lengths of each segment.
- The optimal wedge anchorage is selected based on its gripping strength as well as the maximum von Mises stress within the wedge anchorage.
- The optimal slope of the linear segment is parallel to the slope of the circular profile.
- The same slope of the linear segment is used for the barrel and the wedges to maintain a uniform interference across the linear segments.

### 7.2.2. Tensile Tests

- The optimized wedge anchorage is machined using 4140 steel instead of 440C stainless steel for economical consideration because the yield strength of 4140 steel is higher than the maximum estimated von Mises stress within the anchorage.
- Eight tensile tests are conducted. Five tests are performed by presetting the optimized anchorage using presetting rig, two of which use hard copper sleeves. The other three tests are conducted by hammering the optimized anchorage.
- Using hard copper sleeves induced CFRP premature failure at a tensile loading representing 91% and 94% of the reported tensile strength of the CFRP plate.
- Softening the copper sleeves by heat-treatment at $500\ ^{o}C$ for an hour is sufficient to improve the performance of the optimized anchorage and prevent CFRP premature failure.
- The three tests conducted by hammering the optimized anchorage confirmed its self-seating feature.
- The average tensile loading is 102.4% of the reported tensile strength of the CFRP plate.

### 7.2.3. Presetting Effect Analysis

- The effect of presetting distance on the performance of the wedge anchorage is investigated using both the FEM model and the experimental tests.
- Although increasing the presetting distance would generally increase the CFRP contact pressure and the von Mises stress within the barrel and the wedges, this is not entirely true once the tensile loading is applied. The FEM model revealed that any moderate presetting distance of up to 7 mm would produce almost the same stresses within the anchorage after applying the tensile loading. Nevertheless, applying high presetting distance of more than 7 mm would increase the CFRP contact pressure and von Misses stress within the wedge anchorage accordingly.
- Based on the experimental results, the presetting distance is inversely proportional to the CFRP slipping; however, the effect of the presetting distance on the CFRP slipping diminishes once the presetting distance exceeds 4.45 mm.

### 7.2.4. CFRP Plate Failure Analysis

- CFRP plate failure analysis is conducted analytically using several failure theories. Tsai-Hill theory, Tsai-Wu theory, Hashin theory, and Hoffman theory confirmed that CFRP premature failure is unlikely to occur.
- Experimental tests verified the unlikelihood of CFRP premature failure as the reported tensile strength is fully utilized.
- CFRP failure seems to occur at the dead-end anchorage in every test.

### 7.2.5. Wedge Anchorage Damage Analysis

- Damage analysis is performed after conducting eight tensile tests. Minor plastic deformation is recorded at the loading end of the barrel and the wedges.
- The minor plastic deformation is not expected to affect the performance of the wedge anchorage since the induced stress within the anchorage is minimum at the loading end.
- The reusability of the optimized wedge anchorage is confirmed by maintaining excellent performance after performing eight tensile tests. It is believed that the reusability of the anchorage might exceed ten times of usage.

## 7.3. Recommendations

- The performance of the optimized wedge anchorage can be investigated more accurately by gripping both sides of the CFRP plate using two optimized anchorages.
- The effect of the transferred bending loading between the CFRP plate and the concrete structure can be studied by applying lateral loading across the length of the CFRP plate.
- The performance of the optimized anchorage under cyclic loading needs to be studied.
- The optimized anchorage can be machined from mild steel if the anchorage is going to be used in a non-corrosive environment.
- The wedges and the barrel of the wedge anchorage can be made of dissimilar materials to reduce the material cost since the stress induced on the wedges is relatively low.
- Further optimization on the wedge anchorage can be achieved by investigating the effect of different geometric configurations such as the location of the center of the circular profiles of the wedges and the barrel.

## References


[1] X.-L. Zhao, *FRP-strengthened metallic structures*. Boca Raton: CRC Press, 2014.

[2] B. Benmokrane, H. Xu, and I. Nishizaki, "Aramid and carbon fibre-reinforced plastic prestressed ground anchors and their field applications," *Can. J. Civ. Eng.*, vol. 24, no. 6, pp. 968–985, 1997.

[3] H. J. Dagher, T. E. Kimball, S. M. Shaler, and B. Abdel-Magid, "Effect of FRP reinforcement on low grade eastern hemlock glulams," in *National Conference on Wood Transportation Structures, Madison, WI, General Technical Report No. FPL-GTR-96*, 1996.

[4] H.-J. Kim and J. Sim, "Mechanical properties of GFRP slip-form for in-situ application," *KSCE J. Civ. Eng.*, vol. 20, no. 5, pp. 1842–1851, 2016.

[5] J. R. M. d'Almeida and S. N. Monteiro, "The Role of the Resin Matrix/Hardener Ratio on the Mechanical Properties of Low Volume Fraction Epoxy Composites," *Adv. Perform. Mater.*, vol. 4, no. 3, pp. 285–295, 1997.

[6] C. Meyer and G. Vilkner, "Glass Concrete Thin Sheets Prestressed with Aramid Fiber Mesh," in *PRO 30: 4th International RILEM Workshop on High Performance Fiber Reinforced Cement Composites (HPFRCC 4)*, 2003, vol. 1, p. 325.

[7] C. S. Association, *Design and construction of building components with fibre-reinforced polymers*. Canadian Standards Association, 2002.

[8] M. Samaan, A. Mirmiran, and M. Shahawy, "Model of concrete confined by fiber composites," *J. Struct. Eng.*, vol. 124, no. 9, pp. 1025–1031, 1998.

[9] X. Li, L. G. Tabil, and S. Panigrahi, “Chemical treatments of natural fiber for use in natural fiber-reinforced composites: a review,” *J. Polym. Environ.*, vol. 15, no. 1, pp. 25–33, 2007.

[10] W. Seim, M. Hörman, V. Karbhari, and F. Seible, “External FRP poststrengthening of scaled concrete slabs,” *J. Compos. Constr.*, vol. 5, no. 2, pp. 67–75, 2001.

[11] U. Meier, “Carbon fiber-reinforced polymers: modern materials in bridge engineering,” *Struct. Eng. Int.*, vol. 2, no. 1, pp. 7–12, 1992.

[12] M. A. Erki and S. H. Rizkalla, “FRP reinforcement for concrete structures,” *Concr. Int.-DETROIT-*, vol. 15, pp. 48–48, 1993.

[13] U. Meier and M. Farshad, “Connecting high-performance carbon-fiber-reinforced polymer cables of suspension and cable-stayed bridges through the use of gradient materials,” *J. Comput.-Aided Mater. Des.*, vol. 3, no. 1, pp. 379–384, 1996.

[14] J. W. Schmidt, A. Bennitz, B. Täljsten, P. Goltermann, and H. Pedersen, “Mechanical anchorage of FRP tendons – A literature review,” *Constr. Build. Mater.*, vol. 32, pp. 110–121, 2012.

[15] J. M. Lees, B. Gruffydd-Jones, and C. J. Burgoyne, “Expansive cement couplers: A means of pre-tensioning fibre-reinforced plastic tendons,” *Constr. Build. Mater.*, vol. 9, no. 6, pp. 413–423, 1995.

[16] S. Grelle and L. Sneed, “Review of Anchorage Systems for Externally Bonded FRP Laminates,” *Int. J. Concr. Struct. Mater.*, vol. 7, no. 1, pp. 17–33, 2013.

[17] H. N. Garden and L. C. Hollaway, “An experimental study of the influence of plate end anchorage of carbon fibre composite plates used to strengthen reinforced concrete beams,” *Compos. Struct.*, vol. 42, no. 2, pp. 175–188, 1998.

[18] V. Martelli, G. Bianchini, and G. Ventura, “Measurement of the thermal expansion coefficient of AISI 420 stainless steel between 20 and 293 K,” *Cryogenics*, vol. 62, no. C, pp. 94–96, 2014.

[19] F. Ceroni, M. Pecce, S. Matthys, and L. Taerwe, “Debonding strength and anchorage devices for reinforced concrete elements strengthened with FRP sheets,” *Compos. Part B Eng.*, vol. 39, no. 3, pp. 429–441, 2008.

[20] A. Al-Mayah, K. Soudki, and A. Plumtree, “Development and Assessment of a New CFRP Rod–Anchor System for Prestressed Concrete,” *Appl. Compos. Mater.*, vol. 13, no. 5, pp. 321–334, 2006.

[21] J. W. Schmidt, A. Bennitz, B. Taljsten, and H. Pedersen, “Development of Mechanical Anchor for CFRP Tendons Using Integrated Sleeve,” *J. Compos. Constr.*, vol. 14, no. 4, pp. 397–405, 2010.

[22] L. Taerwe, *Non-Metallic (FRP) Reinforcement for Concrete Structures: Proceedings of the Second International RILEM Symposium*. CRC Press, 1995.

[23] E. Y. Sayed-Ahmed, “Single-and multi-strand steel anchorage systems for CFRP tendons/stays,” 2002, pp. 5–8.

[24] F. P. Bowden, A. J. W. Moore, and D. Tabor, “The Ploughing and Adhesion of Sliding Metals,” *J. Appl. Phys.*, vol. 14, no. 2, pp. 80–91, 1943.

[25] K. Herrmann, *Hardness testing principles and applications*. Materials Park, Ohio: ASM International, 2011.

[26] J. Pelleg, *Mechanical properties of ceramics*. Cham: Springer, 2014.

[27] W. Nafo and A. Al-Mayah, "Mechanical Investigation of Biological Tissues Using Tensile Loading and Indentation," in *Biomechanics of Soft Tissues Principles and Applications*, .

[28] S. Shaji and V. Radhakrishnan, "An investigation on solid lubricant moulded grinding wheels," *Int. J. Mach. Tools Manuf.*, vol. 43, no. 9, pp. 965–972, 2003.

[29] "Elastic contact between randomly rough surfaces: Comparison of theory with numerical results," *ResearchGate*. [Online]. Available: https://www.researchgate.net/publication/243435014_Elastic_contact_between_randomly_rough_surfaces_Comparison_of_theory_with_numerical_results. [Accessed: 18-May-2018].

[30] C. Czaderski, E. Martinelli, J. Michels, and M. Motavalli, "Effect of curing conditions on strength development in an epoxy resin for structural strengthening," *Compos. Part B*, 2011.

[31] E. Y. Sayed-Ahmed, R. Bakay, and N. G. Shrive, "Bond strength of FRP laminates to concrete: State-of-the-art review," *Electron. J. Struct. Eng.*, vol. 9, pp. 45–61, 2009.

[32] B. Zhang, B. Benmokrane, A. Chennouf, P. Mukhopadhyaya, and A. El-Safty, "Tensile behavior of FRP tendons for prestressed ground anchors," *J. Compos. Constr.*, vol. 5, no. 2, pp. 85–93, 2001.

[33] S. Rizkalla, T. Hassan, and N. Hassan, "Design recommendations for the use of FRP for reinforcement and strengthening of concrete structures," *Prog. Struct. Eng. Mater.*, vol. 5, no. 1, pp. 16–28, 2003.

[34] C. A. Neagoe, “Concrete beams reinforced with CFRP laminates,” Master’s Thesis, Universitat Politècnica de Catalunya, 2011.

[35] P. A. Schweitzer, *Corrosion engineering handbook. Fundamentals of metallic corrosion atmospheric and media corrosion of metals*, 2nd ed. Boca Raton: CRC Press, 2007.

[36] P. A. Schweitzer, *Fundamentals of corrosion mechanisms, causes, and preventative methods*. Boca Raton, Fla.: CRC Press, 2010.

[37] J. R. Davis, *Corrosion understanding the basics*. Materials Park, OH, Materials Park, Ohio: ASM International, 2000.

[38] Z. Qiankun, S. Yafei, R. Sixian, L. Huifeng, and Z. Xingjiang, “Corrosion Failure Analysis on Heat Exchanger Pipes,” *J. Fail. Anal. Prev.*, vol. 17, no. 2, pp. 349–353, 2017.

[39] L. P. Pook, *Metal fatigue what it is, why it matters*. Dordrecht: Springer, 2007.

[40] C. Bathias, *Gigacycle fatigue in mechanical practice*. New York: Marcel Dekker, 2005.

[41] B. Åkesson, *Fatigue life of riveted steel bridges*. Boca Raton, Fla.: CRC Press, 2010.

[42] M. M. Khonsari, *Introduction to thermodynamics of mechanical fatigue*. Boca Raton: CRC Press, 2013.

[43] J. Rösler, *Mechanical behaviour of engineering materials metals, ceramics, polymers, and composites*. Berlin ; New York: Springer, 2007.

[44] “In-flight break-up involving de Havilland DH82A Tiger Moth, VH -TSG,” Australian Transport Safety Bureau, Jan. 2016.

[45] M. E. Kassner, *Fundamentals of creep in metals and alloys*, Second edition. Amsterdam ; Boston: Elsevier, 2009.

[46] T. Nishiura, S. Nishijima, and T. Okada, "Creep behavior of an epoxy resin and an epoxy-based FRP in condition of simultaneous supply of radiation and stress at cryogenic temperatures," 1995.

[47] Levi de Oliveira Bueno, Vitor Luiz Sordi, and Luiz Marino, "Constant load creep data in air and vacuum on 2.25Cr-1Mo steel from 600 °C to 700 °C," *Mater. Res.*, vol. 8, no. 4, pp. 401–408, Dec. 2005.

[48] "Sika® CarboDur® CARBON FIBER LAMINATE FOR STRUCTURAL STRENGTHENING." [Online]. Available: http://can.sika.com/dms/getdocument.get/49814cdc-a55b-3580-a2d0-fe12104ac3cd/SikaCarboDur_pds.pdf. [Accessed: 17-Apr-2018].

[49] "Sikadur®-30 - THIXOTROPIC EPOXY ADHESIVE FOR BONDING REINFORCEMENT." [Online]. Available: https://gbr.sika.com/dms/getdocument.get/0a9f54be-6c6d-351e-a4a4-b56e9c98d49d/Sikadur+30+PDS+(CE).pd. [Accessed: 17-Apr-2018].

[50] G. D. Dean and P. Turner, "The elastic properties of carbon fibres and their composites," *Composites*, vol. 4, no. 4, pp. 174–180, 1973.

[51] J. D. Littell, C. R. Ruggeri, R. K. Goldberg, G. D. Roberts, W. A. Arnold, and W. K. Binienda, "Measurement of epoxy resin tension, compression, and shear stress-strain curves over a wide range of strain rates using small test specimens.(Author abstract)(Technical report)," *J. Aerosp. Eng.*, vol. 21, no. 3, pp. 162–173, Jul. 2008.

[52] S.-Y. Lee and G. S. Springer, “Effects of Cure on the Mechanical Properties of Composites,” *J. Compos. Mater.*, vol. 22, no. 1, pp. 15–29, 1988.

[53] R. Maurin, P. Davies, N. Baral, and C. Baley, “Transverse Properties of Carbon Fibres by Nano-Indentation and Micro-mechanics,” *Appl. Compos. Mater.*, vol. 15, no. 2, pp. 61–73, 2008.

[54] P. K. Mallick, *Fiber-reinforced composites: materials, manufacturing, and design*. New York: MDekker, 1988.

[55] T. P. Philippidis and P. S. Theocaris, “The Transverse Poisson’s Ratio in Fiber Reinforced Laminae by Means of a Hybrid Experimental Approach,” *J. Compos. Mater.*, vol. 28, no. 3, pp. 252–261, 1994.

[56] M. Knight, “Three-Dimensional Elastic Moduli of Graphite/Epoxy Composites,” *J. Compos. Mater.*, vol. 16, no. 2, pp. 153–159, 1982.

[57] Peng Feng, Pan Zhang, Xinmiao Meng, and Lieping Ye, “Mechanical Analysis of Stress Distribution in a Carbon Fiber-Reinforced Polymer Rod Bonding Anchor,” *Polymers*, vol. 6, no. 4, pp. 1129–1143, Apr. 2014.

[58] A. Al - Mayah, K. Soudki, and A. Plumtree, “Effect of sleeve material on interfacial contact behavior of CFRP-metal couples.(carbon-fiber-reinforced polymer )(Author abstract),” *J. Mater. Civ. Eng.*, vol. 18, no. 6, pp. 825–830, Nov. 2006.

[59] “Multipurpose 110 Copper with Certification - McMaster-Carr.” [Online]. Available: https://www.mcmaster.com/#1012n84/=1cg0mih. [Accessed: 17-Apr-2018].

[60] “The Copper Book For Architecture - Aurubis.” [Online]. Available: https://finland.aurubis.com/fileadmin/media/pdf/EN/copperbook.pdf. [Accessed: 17-Apr-2018].

[61] S. S. I. of the U. States, S. S. I. of N. America, N. D. Institute (Canada), A. Iron, and S. Institute, *Design Guidelines for the Selection and Use of Stainless Steel*. Specialty Steel Industry of the United States, 1993.

[62] "The Atlas Steels Technical Handbook of Stainless Steels," Atlas Steels.

[63] "Stainless Steel Bar 431, Atlass Steels." Atlass Steels.

[64] "444 Stainless Steel." AKSteel.

[65] "Properties: Stainless Steel - Grade 440 (UNS S44000)," *AZoM.com*. [Online]. Available: https://www.azom.com/properties.aspx?ArticleID=1024. [Accessed: 17-Apr-2018].

[66] "Getting Started with Abaqus: Keywords Edition (6.14)." [Online]. Available: http://abaqus.software.polimi.it/v6.14/books/gsk/default.htm?startat=ch02s04.html. [Accessed: 22-Jun-2018].

[67] F. Mohee, A. Al-Mayah, and A. Plumtree, "Friction Characteristics of CFRP Plates in Contact with Copper Plates under High Contact Pressure," *J. Compos. Constr.*, vol. 20, no. 5, Oct. 2016.

[68] "Coefficient of Friction." [Online]. Available: http://web.applied.com/assets/attachments/492ACC9E-E5C2-2D43-0B8CCDA72ACE3361.pdf.

[69] "Abaqus Analysis User's Manual (6.10)." [Online]. Available: https://www.sharcnet.ca/Software/Abaqus610/Documentation/docs/v6.10/books/usb/default.htm?startat=pt09ch33s01aus154.html. [Accessed: 18-Jun-2018].

[70] M. R. Behbahanifard, G. Y. Grondin, and A. E. Elwi, "Analysis of steel plate shear wall using explicit finite element method," in *Proc., 13th World Conf. Earthq. Eng*, 2004.

[71] P. Rao and V. Subba Rao, “Degradation model based on Tsai-Hill factors to model the progressive failure of fiber metal laminates,” *J. Compos. Mater.*, vol. 45, no. 17, pp. 1783–1792, Aug. 2011.

[72] Z. Hashin, “Failure Criteria for Unidirectional Fiber Composites,” *J. Appl. Mech.*, vol. 47, no. 2, pp. 329–334, 1980.

[73] J. Qiu and M. Zhou, “Analytical Solution for Interference Fit for Multi-Layer Thick-Walled Cylinders and the Application in Crankshaft Bearing Design,” *Appl. Sci.*, vol. 6, no. 12, p. 167, Jun. 2016.

[74] M. Shahzad, A. Kamran, M. Siddiqui, and M. Farhan, “Mechanical Characterization and FE Modelling of a Hyperelastic Material,” *Mater. Res.*, vol. 18, no. 5, Oct. 2015.

[75] “Ultrahigh Strength Steel: Development of Mechanical Properties Through Controlled Cooling,” *ResearchGate*. [Online]. Available: https://www.researchgate.net/publication/221921679_Ultrahigh_Strength_Steel_Development_of_Mechanical_Properties_Through_Controlled_Cooling/citations. [Accessed: 14-May-2018].

[76] “AISI 4140 Alloy Steel (UNS G41400),” *AZoM.com*, 07-Sep-2012. [Online]. Available: https://www.azom.com/article.aspx?ArticleID=6769. [Accessed: 14-May-2018].

[77] “Molykote G-n Metal Assembly Paste and Molykote G-n Metal Assembly Spray.” [Online]. Available: https://www.fmv.se/FTP/Drivmedel%202016/datablad/M0744-0870XX_MOLYKOTE%20GN%20PLUS.pdf. [Accessed: 01-Jul-2018].

## Appendix A. Analytical Model 1

The complex form of the CFRP contact pressure equation **(5.25)** is shown below.

$$P_c(X) = \int_{\theta_1}^{\theta_2} \frac{sin(\theta) * \left(r_2 - (r_1^2 + A + B)^{\frac{1}{2}}\right) * (r_1^2 + A + B)^{\frac{1}{2}}\, d\theta}{\frac{(v-1) * (r_1^2 + A + B)^{\frac{1}{2}}}{E} + \frac{r_2 * \left((v-1) * r_2^2 - (v+1) * r_3^2\right)}{E * (r_3^2 - r_2^2)}}$$

Where

$$A = \frac{\left(\frac{r_1 * (r_1 - r_2) * (cos(\theta_1) - cos(\theta_2))}{\frac{r_1 * (v-1)}{E} + \frac{r_2 * \left((v-1) * r_2^2 + (-v-1) * r_3^2\right)}{E * (r_3^2 - r_2^2)}}\right)^2 * \left(\frac{tp}{Ep} - \frac{tp + ts}{E} + \frac{ts}{Es}\right)^2}{w^2}$$

$$B = \frac{2 * r_1 * sin(\theta) * \left(\frac{r_1 * (r_1 - r_2) * (cos(\theta_1) - cos(\theta_2))}{\frac{r_1 * (v-1)}{E} + \frac{r_2 * \left((v-1) * r_2^2 - (v+1) * r_3^2\right)}{E * (r_3^2 - r_2^2)}}\right) * \left(\frac{tp}{Ep} - \frac{tp + ts}{E} + \frac{ts}{Es}\right)}{w}$$

## Appendix B. Analytical Model 2

The complex form of the CFRP contact pressure equation **(5.36)** is given below.

$$P_c(X) = \int_{\theta_1}^{\theta_2} \frac{r_1 * sin(\theta) * (r_2 - r_1)\, d\theta}{W(A * B + C)}$$

Where

$$A = \left(\frac{r_1}{\frac{r_1 * sin(\theta) - (t_p + t_S)}{v_1 * sin(\theta)} + \frac{t_S}{v_S * sin(\theta)} + \frac{t_p}{v_P * sin(\theta)}} - 1\right)$$

$$B = \left(\frac{r_1 * sin(\theta) - (t_p + t_S)}{E_1 * sin(\theta)} + \frac{t_S}{E_S * sin(\theta)} + \frac{t_p}{E_P * sin(\theta)}\right)$$

$$C = \left(\frac{r_2 * \left((v_2 - 1) * r_2^2 - (v_2 + 1) * r_3^2\right)}{E_2 * (r_3^2 - r_2^2)}\right)$$